LBL-31466

Lawrence Berkeley Laboratory
UNIVERSITY OF CALIFORNIA

Materials & Chemical
Sciences Division

Photoelectron and Photodissociation Studies of Free Atoms and Molecules, Using Synchrotron Radiation

L.J. Medhurst
(Ph.D. Thesis)

November 1991

Prepared for the U.S. Department of Energy under Contract Number DE-AC03-76SF00098

LBL--31466

DE92 004001

Photoelectron and Photodissociation Studies of Free Atoms and Molecules, Using Synchrotron Radiation

Laura Jane Medhurst
Ph.D. Thesis

Department of Chemistry
University of California at Berkeley

and

Chemical Sciences Division
Lawrence Berkeley Laboratory
University of California
Berkeley, CA 94720

November 1991

This work was supported by the Director, Office of Energy Research, Office of Basic Energy Sciences, Chemical Sciences Division of the U. S. Department of Energy under the Contract No. DE-AC03-76SF00098

Photoelectron and Photodissociation Studies of Free Atoms and Molecules, Using Synchrotron Radiation

By

Laura Jane Medhurst

Abstract

High resolution synchrotron radiation and Zero-Kinetic-Energy Photoelectron spectroscopy were used to study two-electron transitions in atomic systems at their ionization thresholds. Using this same technique the core-ionized mainline and satellite states of N_2 and CO were studied with vibrational resolution. Vibrationally resolved synchrotron radiation was used to study the dissociation of N_2, C_2H_4, and CH_3Cl near the N 1s and C 1s thresholds.

The photoelectron satellites of the argon 3s, krypton 4s and xenon 4d subshells were studied with zero kinetic energy photoelectron spectroscopy at their ionization thresholds. In all of these cases, satellites with lower binding energies are enhanced at their thresholds while those closer to the double ionization threshold are suppressed relative to their intensities at high incident light energies.

Zero-Kinetic-Energy photoelectron spectra were taken of N_2 and CO at the N 1s and C 1s ionization thresholds. Vibrational structure was observed for the $1s^{-1}$ mainlines and the lowest binding energy satellite of CO, which was consistent with the

equivalent core approximation. Many new satellites with different symmetries from the mainline were discovered.

The photodissociation fragments of core-excited and ionized N_2 were measured in coincidence with low energy electrons as functions of the vibrationally resolved incident light energy. The kinetic energy distributions of the fragments were determined and compared with the calculated energies for the dissociative potentials. Excess vibrational energy at the $1s \rightarrow \pi^*$ transition does not appear as kinetic energy of the dissociative fragments. Highly energetic dissociative states are present, which must result form triply charged N_2.

The photodissociation fragments of C_2H_4 and CH_3Cl were measured in coincidence were low energy electrons near the C 1s ionization threshold. For C_2H_4, the 4s Rydberg state can relax via participant Auger decay to stable $C_2H_4^+$. Quasi stable $C_2H_4^{+2}$ is also present. Energetic fragments are correlated with the electron impact Auger spectrum. For CH_3Cl, the dissociation pattern is very similar for the entire C 1s ionization region. Subtile differences are present. Cl^{+2} is less intense at the C $1s \rightarrow 4pe$ transition.

Contents

Part II Photodissociation

Acknowledgements

First I thank the taxpayers of the United States for supporting this work. Professor Dave Shirley procured this support and provided patient guidance throughout this work. Dennis Lindle, Trish Ferrett, and Phil Heimann taught me the basics of synchrotron based experiments and after they all left LBL continued to provide much practical advice. Phil, in the past three years, has been a real mentor to me and without him about half this thesis would not exist.

Those who have contributed directly to these experiments are Shihong Liu, Baohua Niu, Y. Yang, Jing Song Zhang, Roger van Zee, and Michelle Siggel. Lou Terminello and Alexis Schach von Wittenau both participated in experiments and supplied valuable computer expertise. Special thanks also goes to Laisheng Wang who helped me with Franck-Condon calculations, obtaining sample gases and turbo pumps, and many other things. From the Actinide group, Jerry Bucher helped with data transfer, and Norman Edelstein helped with the Xe calculations. The technical and engineering staffs at LBL, SSRL, and NSLS have also supplied valuable assistance. Special thanks also go to Y. Ma, Silivo Modesti and especially C. T. Chen for their help with the experiments performed on the AT&T beamline, and their interest in the work completed there. I would also like Wolfgang Eberhardt for his generous help with the experiment completed on U1.

I also thank my friends and colleagues in the Shirley group, who have helped me with many aspects of this work, my office mate Li-Qiong Wang, my classmate Zheng qing Huang, Zahid Hussain, Laisheng, Baohua, Tina, Tobius, Eric, and Lou, and in the Actinide group Wing, Glen, and David. My friends and classmates in the Chemistry department have been a constant source of scientific information and companionship, especially my former housemates Jeff and Pam, and my neighbors, Becca, Steve, and

Jackie. Extra special thanks for those who offered and provided shelter during my brief period of homelessness, Zheng qing, Roger, Phil, and Pam.

Lastly I thank my family, primarily my parents, Ward and Dorothy Medhurst, for constant encouragement and love.

This work was supported by the Director, Office of Energy Research, Office of Basic Energy Sciences, Chemical Sciences Division of the US Department of Energy under Contract No. DE-AC03-76SF00098.

Part I Zero-Kinetic-Energy PES

Introduction

The photoelectric effect was discovered by Hertz in 1886, 100 years before the work in this thesis began. In 1905, Einstein explained this phenomenon by quantizing light[1] and giving us the famous relation that the electron's kinetic energy equals the light energy minus the binding energy. By the late 1960's photoelectron spectroscopy had split into two divisions, which persist today, Ultraviolet Photoelectron Spectroscopy (UPS)[2] and Electron Spectroscopy for Chemical Analysis (ESCA).[3] UPS concentrates in the valence molecular orbital area, with sufficent resolution to separate vibrational levels of many small molecules. One example of a recent UPS experiment is the study of the transition state for neutral hydrogen transfer reactions.[4] In this case negative ions of the type AHB^-, where A and B are halogens, are crossed with laser light energetic enough to photodetach the least bound electron. This probes the energy levels of the neutral AHB molecule, which is a probable transition state for the reaction: $A + HB \rightarrow AH + B$. ESCA is a lower resolution technique because of the natural linewidth of X-rays, but it can probe atomic-like core electrons. ESCA has been applied lately to determine the electronic structure of high T_c superconductors.[5] In the case of $YBa_2Cu_3O_7$, X-ray photoelectron spectroscopy has shown that the superconducting

transition in this material leads to an increase of Cu^{+1} relative to Cu^{+2}, and that Cu^{+3} is not present, contrary to preliminary theoretical predictions.

A first approximation atomic photoelectron spectrum shows one peak for every occupied electronic subshell, and a molecular spectrum shows a peak for every occupied molecular orbital. Light of sufficient energy, then, could provide a direct measurement of all the electronic energy levels of the positive ion. In the dipole approxmation the cross section for the production of any particular ionic state, σ_j, is:

$$\sigma_j \propto \frac{1}{h\nu} \sum_k | < \Psi_j^{(N-1)} \; \phi_k(\varepsilon) | \sum_k^N r_\mu | \Psi_i(N) > |^2 \qquad (1)$$

where Ψ_j is the ionic wavefunction, ϕ_k is the continuum electron wavefunction, Ψ_i is the initial state wavefunction, and r_μ is the dipole operator. In general the one-electron ionic states, corresponding to the different orbitals, the mainlines, are followed by less intense transitions to states which in the first approximation, correspond to ionization of one electron plus excitation of another electron to an unoccupied orbital. These satellites are produced by electron correlation. The calculated energies and intensities of these states are sensitive to the way in which electron correlation is included in the wave function. Because the cross section depends on the incident light energy through the wavefunction of the continuum electron, the relative intensities of the different ionic states vary with the outgoing electron's kinetic energy. For satellites the energy dependence of the intensities is very difficult to calculate. In the limit of very high kinetic energy for the outgoing electron, however, the sudden approximation[6] can be used. This assumes that ionization of an electron from the particular orbital happens so rapidly that the outer shell electrons suddenly find themselves in the coulombic field of the ion, now with a finite probability of being in an excited state. Without ground state correlation, the resulting

satellites have the same symmetry as the mainline, and the transition in this independent particle formulation is often written as:

$$< \varepsilon^{l+1} \mid r \mid \phi_{nl} > < \psi_{n''l'} \mid \phi_{n'l'} > \qquad (2)$$

where ϕ_{nl} is the ground state wavefunction for the mainline electron, $\phi_{n'l'}$ is the ground state wavefunction for the electron which is excited during the transition, $\psi_{n''l'}$ is the one electron wavefunction of the excited electron in the ionic state, and l, the orbital angular momentum, does not change between the ground state and the ionic state. Most of the theoretical and experimental work has been performed in this limit. For many systems these monopole transitions are dominant at the high energy limit.

Attempts to find a simple, general treatment of satellites at threshold, zero kinetic energy, have been less successful. Chapter 1 of this dissertation will discuss this problem in the context of the satellites of the Ar $3s^{-1}$, Kr $4s^{-1}$, and Xe $4d^{-1}$ subshells. For the Ar $3s^{-1}$ and Kr $4s^{-1}$ valence satellites it is possible to distinguish most of the individual satellites and compare them with optical data. The monopole satellites are ^2S and ^2P states, and these are present through configuration interaction in the final state. Therefore satellites of other symmetry are present through initial state configuration interaction or dynamic effects. One of these dynamic effects is called conjugate shakeup. If the transition for direct satellites is expressed as (2), the conjugate transition is:

$$< \psi_{n'' l+1} \mid r \mid \phi_{nl} > < \varepsilon^{l'} \mid \phi_{n'l'} > \qquad (3)$$

Therefore these satellites have different selection rules than the direct transitions. For Xe $4d^{-1}$, the satellites are too numerous to be resolved, but a general comparison of the dynamic phenomena is possible. The results from the atomic systems will then compared to the molecular core-level satellites of N_2 and CO in Chapter 2.

These experiments were performed using a time-of-flight zero-kinetic-energy electron analyzer and synchrotron radiation. Details of the experimental apparatus can

Zero Kinetic Energy Electron Analyzer

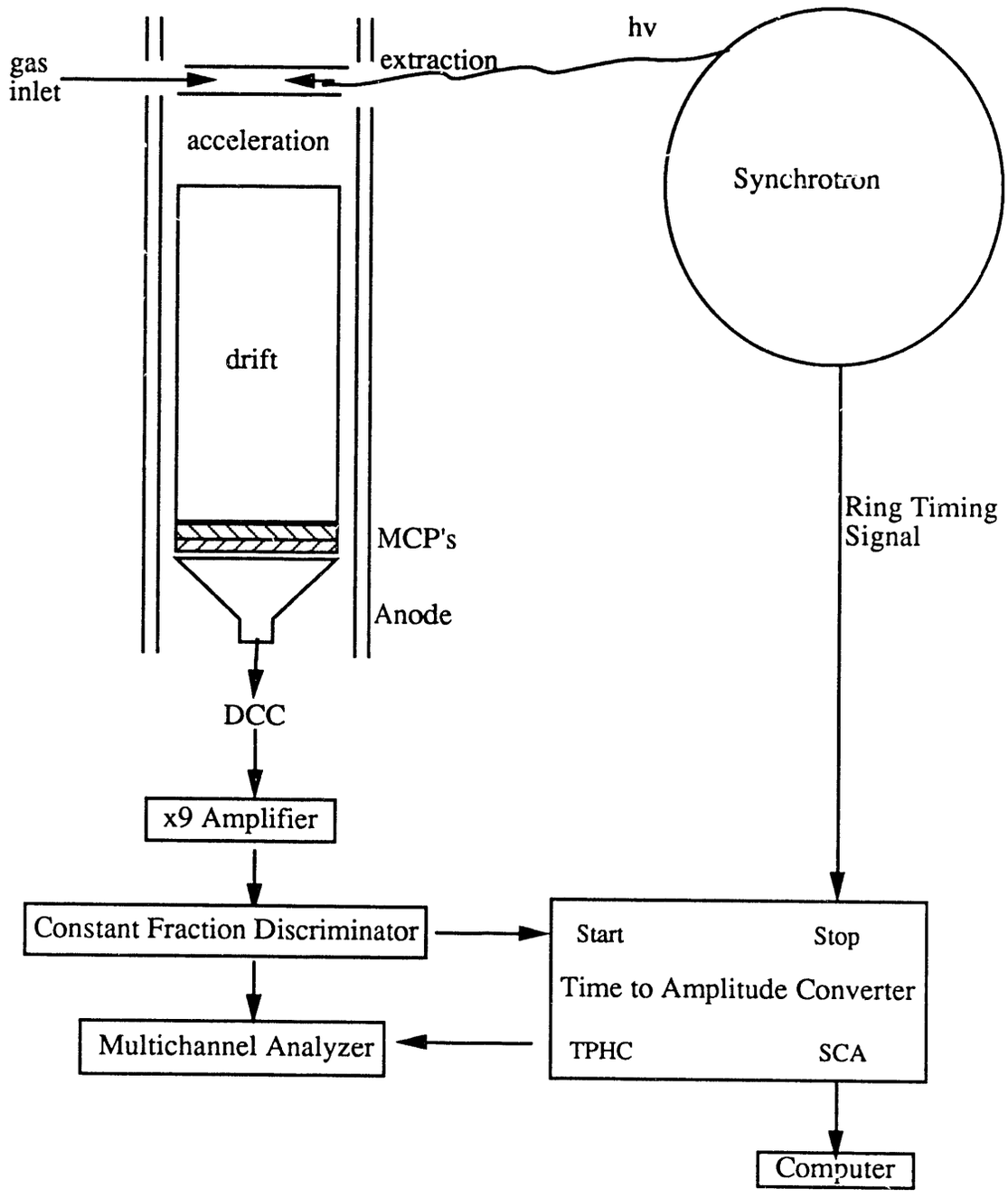

FIGURE I.1 Schematic Diagram of Experimental Apparatus

be found elsewhere.[7] Figure I.1 shows the important features. Gas from an effusive source intersects the synchrotron radiation between two grids, which provide the electric field to extract the low energy photoelectrons. The analyzer possesses three different field regions, extraction, acceleration, and drift. It was configured according to the space focussing conditions of Wiley and McLaren.[8] After passing through the flight tube, the signal is multiplied by two multichannel electron multplying plates in a chevron configuration. The signal is then separated from the high voltage of the resistive anode by a decoupling capacitor. Figure I.2 shows the calculated transmission as a function of kinetic energy, discounting the effect of the grids. The electron pulse, after amplification and discrimination, starts a time to amplitude converter. The light pulses come from the synchrotron about every 200 nanoseconds. A clock pulse from the synchrotron provides the stop pulse. The resulting time spectrum is displayed by a multichannel analyzer. A time window can then be selected, which corresponds to one kinetic energy of the photoelectrons. The experimental resolution is approximately 0.03 eV, for zero kinetic energy electrons. The spectra of chapters 1 and 2 show the intensity of zero kinetic energy electrons detected as a function of the synchrotron radiation energy. Synchrotron radiation is used, because it provides a tunable source of vacuum ultraviolet and soft X-ray radiation.

Since two different ZKE analyzers were used, one oriented 54.7° from the polarization vector and the other at 90°, the angular distribution of the ejected electrons must be considered. The differential cross section is:[9]

$$\frac{d\sigma}{d\Omega} = \frac{\sigma_{tot}}{4\pi} [\, 1 + \frac{\beta}{2} (3\cos^2\theta - 1)] \qquad (4)$$

where θ is the angle between the polarization vector and the analyzer and β is the asymmetry parameter. β has been derived as:[10]

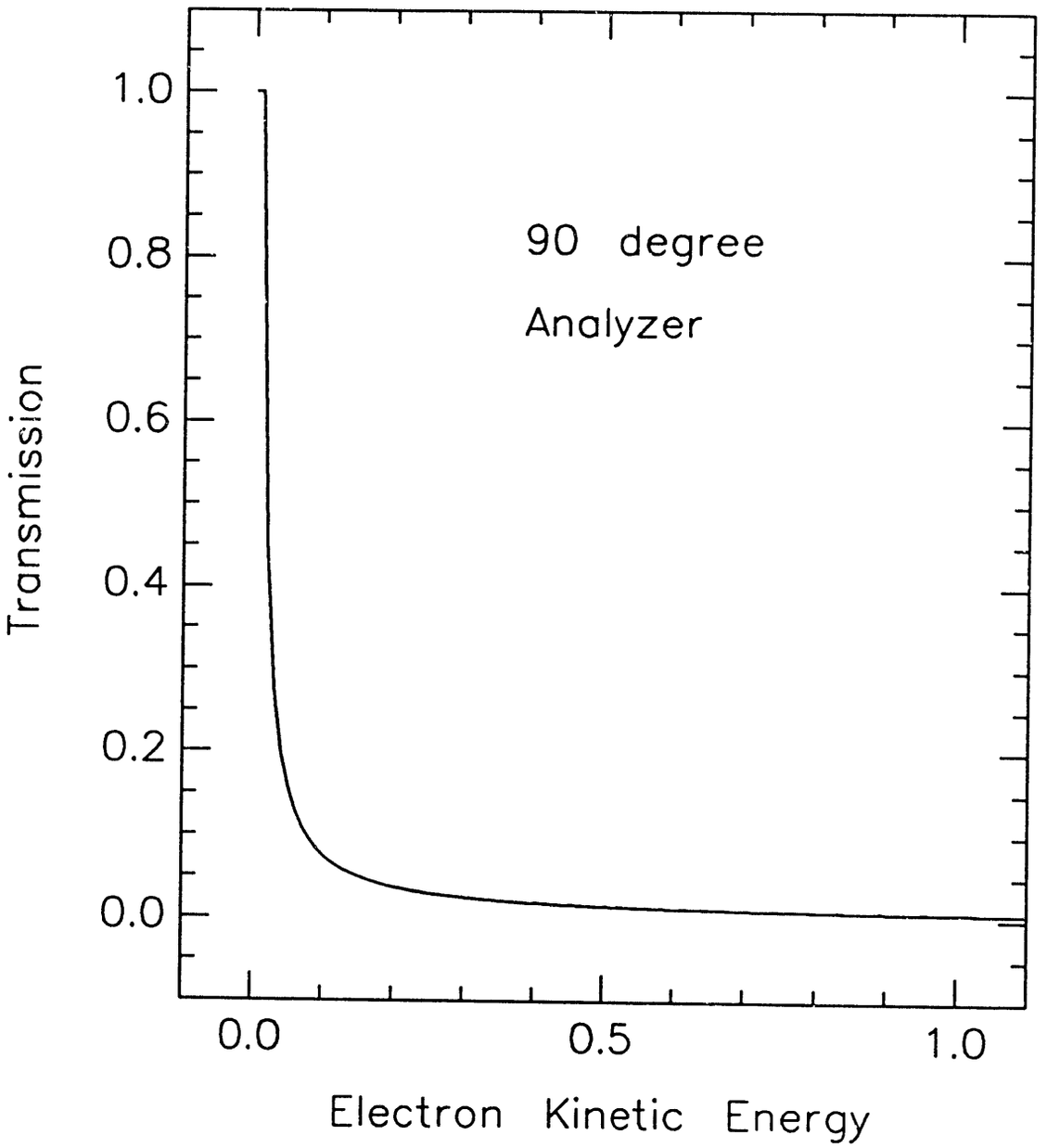

FIGURE I.2 Theoretical transmission of ZKE analyzer as a function of Electron Kinetic Energy.

$$\beta = \frac{l(l+1)(\sigma_{(l-1)})^2 + (l+1)(l+2)(\sigma_{(l+1)})^2 - 6\, l(l+1)\, \sigma_{(l+1)}\, \sigma_{(l-1)} \cos(\delta_{(l+1)} - \delta_{(l-1)})}{3(2l+1)[l\,(\sigma_{(l-1)})^2 + (l+1)\,(\sigma_{(l+1)})^2]} \quad (5)$$

for atoms with equally populated magnetic sublevels and wavefunctions which are antisymmetrized products of spin orbitals. $\sigma_{(l\pm1)}$ is the radial dipole matrix element,

$$\sigma_{(l\pm1)} = \int R_{nl}\, r\, R_{nl\pm1}\, dr \quad (6)$$

and δ_l is the l^{th} partial wave's phase shift. β ranges from 2 to -1. For an isotropic distribution, an outgoing s-wave, $\beta = 0$, and $\beta = 2$ for an outgoing p-wave. For electrons with kinetic energies ≤ 30 meV, the entire solid angle is collected, so effects of the angular distribution should not be present in ZKE spectra. However, cross sections measured at 90° will be reported as such.

The majority of these experiments were performed using the 90° analyzer. For this analyzer the length of the extraction region, d_{ex}, was 0.5 cm., the acceleration region, d_{acc}, 1.8 cm., and the drift region, d_d, 26.2 cm. The fields used were $E_{ex} = 2.2$ V/cm. and $E_{acc} = 5.95$ V/cm. For the 54.7° analyzer, d_{ex}, = 0.5 cm., $d_{acc} = 1.8$ cm., $d_d = 19.2$ cm., $E_{ex} = 2.2$ V/cm. and $E_{acc} = 3.6$ V/cm. The spectra were corrected for incident light intensity determined either with the fluorescence from a sodium salycilate scintillator and phototube or electron yield from a gold grid. Specific details for each spectrum will be presented with it.

Chapter 1 Atomic Satellites at Threshold

> Since the structure of molecules and their reactions with each other underlie all of chemistry and biology, quantum mechanics allows us in principle to predict nearly everything we see around us, within the limits set by the uncertainty principle. (In practice, however, the calculations required for systems containing more than a few electrons are so complicated that we cannot do them.)
>
> Stephen Hawking, *A Brief History of Time,* Bantam Books, New York 1988, page 60.

The various approximations used in determining the electronic structure of atoms and molecules differ mainly in the way electron interaction is included. Most start from the Hartree-Fock mean field[1] approximation and improve upon this by adding excited configurations to the wave functions. If an atom is considered solely the sum of one-electron wave functions, ionizing radiation produces an emission spectrum consisting of electrons whose binding energies are equal to their orbital energies (Koopman's Theorem). This one-electron description, however, fails to give even a qualitatively correct description for ionization in some cases, for example the energy ordering of the valence orbitals of N_2.[2] Inclusion of electron interaction in the calculation can rectify this. The difficulty of including electron interaction makes it important to understand the types of correlation which are important. The photoelectron satellite spectrum, within a given basis set, shows directly the types of correlation present for that system. If both the two limits in the kinetic energy of the departing electron are known, the relative

importance of static (high kinetic energy) and dynamic (threshold) correlation can be determined.

The static contribution to the satellites is usually calculated in the sudden approximation. This gives the relative intensities of the satellites as the overlap of the initial state with the final ionic state. After ionization, the outer electrons relax toward the nucleus.[3] This change in the spatial distribution of the ionic wavefunctions gives intensity to the excited ionic states. Because the dipole transition has, in this description, already happened, the satellites must have the same symmetry as the one-electron core-hole state, the mainline. At very high kinetic energy, the continuum electron states are similar, and in general most of the satellites in X-ray spectra can be assigned to final states with the same symmetry as the mainline.[3] The relative intensities calculated in this way are usually too low,[4] and electron correlation in the form of configuration interaction is necessary. Dyall and Larkins have compared the intensities of satellites obtained from Hartree-Fock wave functions with those obtained from configuration interaction (CI) wave functions for the valence shells of rare gases. In all cases, the total satellite intensity is greater in the CI calculation, and the relative intensities of the satellites also changes.

As the kinetic energy of the photoelectron decreases the mechanism of a particular satellite is revealed. The effects of CI in the initial state and final state are independent of the kinetic energy. At lower kinetic energies, however, the continuum electrons' wave functions are very different and the so-called "conjugate shake up" states can appear. Also at specific incident light energies highly excited autoionizing states can relax into satellite states.

By measuring the satellites at threshold for the Ar $3s^{-1}$, Kr $4s^{-1}$, and Xe $4d^{-1}$ subshells and comparing them with existing sudden limit, kinetic energy and theoretical studies, I hoped to gain insight into the various mechanisms of electron interaction. First

I will discuss the previous studies on the Ar $3s^{-1}$ satellites, since it has been studied in the greatest detail. I then present my results for the satellites' threshold spectrum of Ar $3s^{-1}$ and an explanation for the appearance of many states not present at the sudden limit. These results for Ar $3s^{-1}$ are then compared with those for Kr $4s^{-1}$, which has the same symmetry as the Ar $3s^{-1}$ subshell, and the more complex Xe $4d^{-1}$ system.

The Sudden Limit

The argon satellites which appear between the $3s^{-1}\ ^2S$ threshold (29.24 eV) and the $3p^{-2}\ ^3P$ double ionization threshold (43.38 eV) have the general valence electron configuration $3s^23p^4nl$. The configurations $3s3p^5nl$ are not in this binding energy range. Table 1.1 shows the possible final state symmetries for the argon valence satellites with l = s,p,and d, and Table 1.2 shows the experimentally determined final states using optical data.[5] In this case, there are two mainlines, the $3s^{-1}\ ^2S$ state and the

Valence Orbitals	Final State Symmetries		
$3s^23p^4$	^1S	^1D	^3P
+np (direct shakeup)	^2P	^2F, ^2D, ^2P	^4D, ^2D, ^4P, ^2P, ^4S, ^2S
+ns (conjugate shakeup)	^2S	^2D	^4P, ^2P
+nd (conjugate shakeup)	^2D	^2G,^2F, ^2D, ^2P, ^2S	^4F, ^2F, ^4D, ^2D, ^4P, ^2P, ^4S, ^2S

Table 1.1 Shakeup Final States

$3p^{-1}\ ^2P$ state, so the satellites in the sudden approximation should have either ^2P or ^2S symmetry. In the absence of CI the final states are further restricted to $3s^23p^4np$, ^2S or ^2P configurations.

Assignment	Optical Energy[a]
$3s^{-1}\ ^2S$	29.24
$3p^{-2}(^3P)3d\ ^4D$	32.18
$3p^{-2}(^3P)4s\ ^4P$	32.46
$3p^{-2}(^3P)4s\ ^2P_{3/2}$	32.90
$3p^{-2}(^3P)\ 4s^2P_{1/2}$	33.02
$3p\text{-}2(^3P)3d^4F$	33.45
$3p^{-2}(^3P)3d\ ^2P_{1/2}$	33.70
$3p^{-2}(^3P)3d\ ^2P_{3/2}$	33.82
$3p^{-2}(^3P)3d\ ^4P$	34.06
$3p^{-2}(^1D)4s\ ^2D_{3/2}$	34.18
$3p^{-2}(^1D)4p\ ^2D_{5/2}$	34.21
$3p^{-2}(^3P)3d\ ^2F$	34.30
$3p^{-2}(^3P)3d\ ^2D$	34.49
$3p^{-2}(^1D)3d\ ^2G$	34.88
$3p^{-2}(^3P)4p\ ^4P$	35.01
$3p^{-2}(^3P)4p\ ^4D$	35.30
$3p^{-2}(^3P)4p\ ^2D$	35.44
$3p^{-2}(^3P)4p\ ^2P_{1/2}$	35.56
$3p^{-2}(^3P)4p\ ^2P_{3/2}$	35.62
$3p^{-2}(^3P)4p\ ^4S$	35.72
$3p^{-2}(^3P)4p\ ^2S$	35.73
$3p^{-2}(^1D)3d\ ^2F$	36.03
$3p^{-2}\ (^1S)4s\ ^2S$	36.50
$3p^{-2}(^1D)4p\ ^2F$	36.89
$3p^{-2}(^1D)4p\ ^2P$	37.11
$3p^{-2}(^1D)3d\ ^2D$	37.18
$3p^{-2}(^1D)4p\ ^2D$	37.25
$3p^{-2}(^1D)3d\ ^2P$	37.40
^2P	38.04
$3p^{-2}(^3P)5s\ ^4P$	38.32

Assignment	Optical Energy
$3p^{-2}(^3P)5s\ ^2P$	38.48
$3p^{-2}(^3P)5s\ ^2P$	38.55
$3p^{-2}(^1D)3d\ ^2S$	38.58
$3p^{-2}(^3P)4d\ ^4F$	38.77
$3p^{-2}(^3P)4d\ ^4P$	38.90
$3p^{-2}(^1S)3d\ ^2D$	38.91
$3p^{-2}(^3P)4d\ ^2F$	38.96
$3p^{-2}(^3P)5p\ ^2P$	39.33
$3p^{-2}(^3P)5p\ ^2D$	39.38
$3p^{-2}(^3P)4d\ ^2P$	39.39
$3p^{-2}(^3P)5p\ ^2S$	39.53
$3p^{-2}(^1S)4p\ ^2P$	39.57
$3p^{-2}(^3P)4d\ ^2D$	39.64
$3p^{-2}(^3P)4f\ ^4F$	39.91
$3p^{-2}(^3P)4f\ ^4D$	39.94
$3p^{-2}(^1D)5s\ ^2D$	40.04
$3p^{-2}(^3P)\ 4f$	40.07
$3p^{-2}(^3P)4f\ ^2D$	40.14
$3p^{-2}(^1D)4d\ ^2G$	40.38
$3p^{-2}(^3P)6s\ ^4P$	40.44
$3p^{-2}(^1D)4d\ ^2P$	40.53
$3p^{-2}(^1D)5s\ ^2D$	40.51
$3p^{-2}(^3P)6s\ ^2P$	40.58
$3p^{-2}(^1D)4d\ ^2F$	40.58
$3p^{-2}(^3P)5d\ ^2P$	41.10
$3p^{-2}(^3P)5d\ ^2D$	41.12
$3p^{-2}(^1D)4d\ ^2S$	41.20
$3p^{-2}(^1D)4f\ ^2P$	41.62
$3p^{-2}(^3P)6s\ ^2D$	42.16

Table 1.2 Argon 3s Satellites from Optical Data

a. C. E. Moore, Ref. 5.

Table 1.3 lists the experimental results of Svensson et. al [6] obtained with Al Kα radiation, 1487 eV, which should fall within the sudden approximation. Their assignments made in the intermediate coupling scheme show the importance of CI, because the most intense satellites are those with the configuration $3s^23p^4nd,\ ^2S$. Their

detector is located 90° to the propagation direction of the unpolarized light, and for unpolarized light $d\sigma/d\Omega = \sigma_{tot}/4\pi[1 - \beta/4(3\cos^2\theta' - 1]$.[7] Therefore $d\sigma/d\Omega \propto \sigma_{tot}[1 + \beta/4]$, and the asymptotic value for β for the ^2S states is two. Since that is the maximum value of β, and the βs for the ^2P states should be less than 2.0, the actual cross section ratios, $^2S/^2P$ are probably somewhat less than those presented in Table 1.3.

Peak #	Assignment	Binding Energy[a]	Intensity[a]	Theoretical Energy[b]	Theoretical Intensity[b]
	$3s3p^5\ ^2S$	29.24	100.0		100.0
1	$3s^23p^4(^3P)3d\ ^2P$	34.50	0.05(5)		
2	$3s^23p^4(^3P)4p\ ^2P$	35.64	0.6(1)	36.16	0.3
3'	$3s^23p^4(^1S)4s\ ^2S$	36.52	0.6(1)	37.74	1.5
4	$3s^23p^4(^1D)4p\ ^2P$	37.15	3.7(3)	37.98	1.8
4'	$3s^23p^4(^1D)3d\ ^2S$	38.60	18.6(5)	39.80	13.2
5	$3s^23p^4(^1S)4p\ ^2P$	39.57	1.5(2)	40.64	0.4
6	$3s^23p^4(^1D)4d\ ^2S$	41.21	9.4(4)	42.23	8.6
	$3s^23p^4(^1D)5d\ ^2S$	42.67	4.1(3)	43.52	2.3
	$3s^23p^4(^1D)6d\ ^2S$	43.43	1.5(2)		
	$3s^23p^4(^1D)7d\ ^2S$	44.00	0.5(1)		

Table 1.3 Argon 3s Satellites at the Sudden Limit
a. Svensson et. al., Ref. 6.
b. Dyall and Larkins, Ref. 4.

The configuration interaction explanation for the great intensities of the nd series is Final Ionic State Configuration Interaction (FISCI) between the $3s3p^5$ and $3s^23p^4nd$ states.[4] The results of Dyall and Larkins are also presented in Table 1.3, and they qualitatively reproduce the experimental results. A comparison of Table 1.2 and Table 1.3 reveals a difficulty; the experimental resolution is approximately 0.5 eV, but the separation between the possible final states can be as small as 0.01 eV. For the lower binding energy satellites the assignments are particularly tenuous. Another method used

to determine the energies and intensities in the sudden limit is Electron Momentum Spectroscopy (EMS). An electron collides with the atom under high kinetic energy and low momentum transfer conditions, thus simulating an X-ray. Using this technique, Leung and Brion[8] measured the angular distributions for two of the Ar $3s^{-1}$ satellites (binding energy = 38.5 and 41.1 eV) in momentum space. The momentum distributions are the same as that of the $3s^{-1}$ mainline, and this confirms the ^2S assignments for these two states. For the Ar $3s^{-1}$ satellites, however, there were persistent differences in the relative intensities between the electron coincidence measurements and the XPS results, which produced a flood of experimental and theoretical work on this system.[9] In summary, the EMS experiments give approximately twice as much relative intensity to the satellites compared with the $3s^{-1}$ mainline, and the binding energies between the various measurements and theories did not agree within the experimental error.

Energy Dependence

In 1985, Adam et. al.[10] made an extensive study of the $3s^{-1}$ satellites from 40 eV to 70 eV incident light energy. The results of this study are reproduced in figure 1.1. Peaks 4, 5, and 6 reach their sudden limit relative intensities by 70 eV incident energy, and their asymmetry parameters are 2.0 with the experimental error. Therefore, their assignment as the $3s^23p^4nd$ series was still upheld. Since their relative intensities are almost invariant, except at extremely low kinetic energies, it is also probably true that their intensity is derived from FISCI.

Satellites 1, 2, 3, and 4', however, behave very differently. They have maximum intensity at about 43 eV, which corresponds to the Cooper minimum in the $3s^{-1}$ photoionization channel. This implies that they do not derive intensity from the $3s^{-1}$

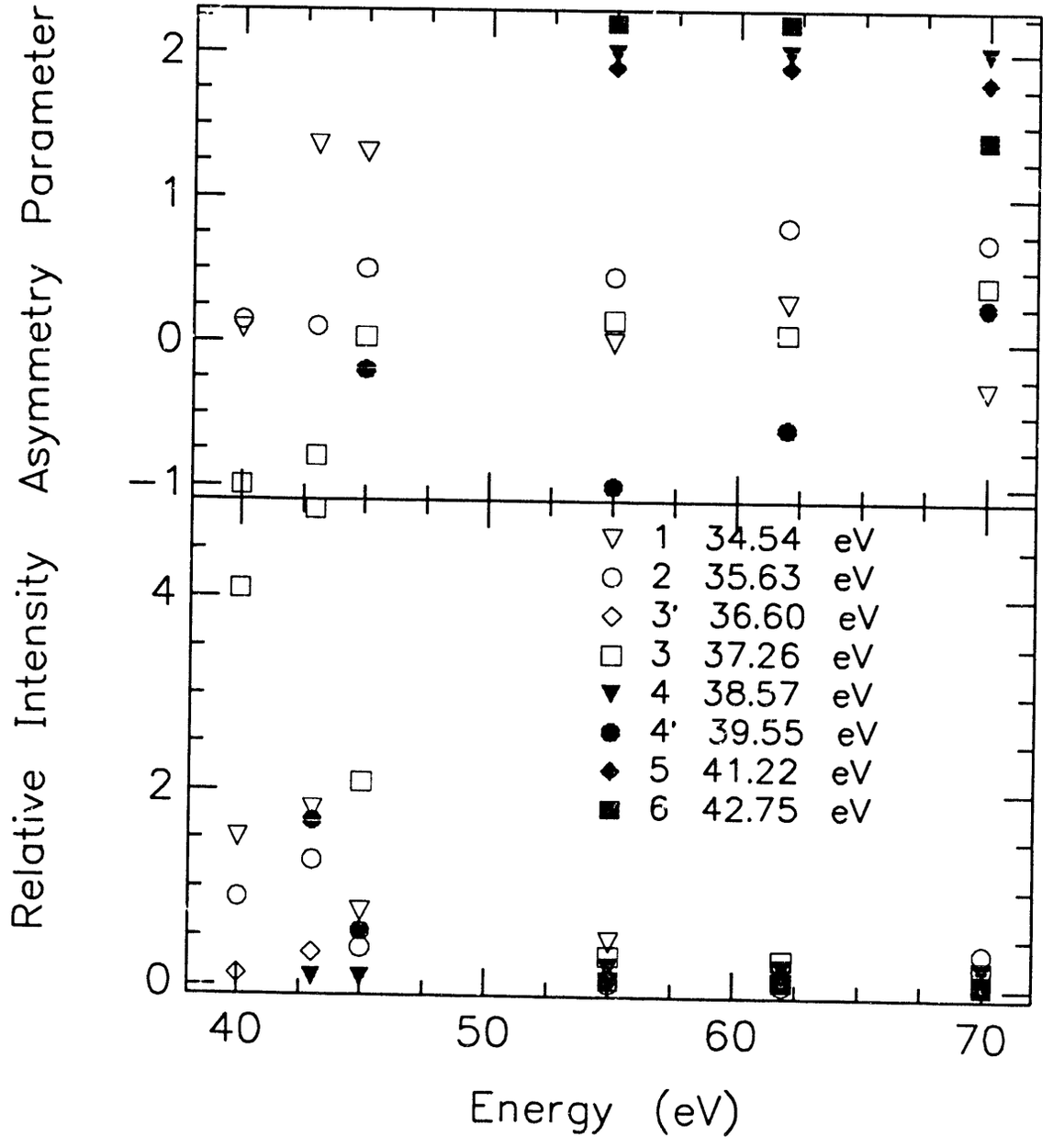

FIGURE 1.1 Intensities of Satellites as a function of energy relative to the 3s mainline, 1=100%, and asymmetry parameters for the same satellites from Adam et. al., ref. 10. Measured binding energies are listed.

mainline. This is supported by the similarity of the sum of these satellites cross sectionto the $3p^{-1}$ cross section. The satellites' asymmetry parameters, however, are not that similar to the $3p^{-1}$ asymmetry parameter. Therefore, the results of Adam et. al. did not conclusively determine the configuration of satellites 1, 2, 3, and 4', but because of the asymmetric shape of peaks 1 and 2, they suggested that these peaks might contain more than one electronic final state. The likely candidates for these states, based on optical data, are ^2D states. The presence of ^2D states can be explained by either initial state CI, in which case they should also be present at the sudden limit, or by conjugate shakeup, which was shown in table 1.1 to access ^2D states through either a dipole or monopole transistion of the 3p electron.

Several subsequent experiments were performed in the energy range of 80 - 120 eV.[11] The original purpose of these experiments was to clarify the intensity differences between the EMS spectra, XPS, and theory. One the first of these experiments foundthe ratio, $3s^23p^43d$ (^2S) / $3s3p^5$ (^2S) to increase with increasing incident energy.[12] This contradicted a very simple theoretical model,[13] which is based solely on the energy variation of the dipole matrix element $D(\varepsilon) = |\langle \varepsilon p \mid r \mid ns \rangle|^2$. Since this matrix element increases as the kinetic energy is decreased, the satellites which have noticeably lower kinetic energies near threshold increase relative to the ^2S mainline. Applying this to the sudden limit CI calculations helped the calculations approach the value of Adam et. al. at 77 eV. However, it did not explain the variations of the $3s^23p^4nd$ satellites at near threshold kinetic energies, since Adam showed that they decrease toward their thresholds.

One experimental difficulty in synchrotron based-experiments was brought forward indirectly by Kossman et. al.[11] The bandwidth of a monochromator is constant in wavelength, and consequently depends on the square of the energy. Also in all the experiments mentioned thus far, the resolution is much lower (on the order of 1.0 eV)

than the separation between electronic states. It is usually assumed that at the sudden limit, this should not cause too much confusion, since the most intense states will be those which have the same symmetry as the mainline, while at lower incident energies the conjugate states might be present. It was never shown experimentally, however, whether conjugate states are absent at higher incident energies or just obscured by lower resolution. The data of Kossman et. al. are summarized in figure 1.2. This work has a total resolution of <0.5 eV. At this higher resolution peak 1 is seen to split into 2 separate peaks. Both of these states are best described as conjugate shakeup states, and over this energy range they are small and decreasing with increasing kinetic energy.

The two other newly visible states (binding energy = 38.03 and 41.77 eV), also small and decreasing, are not assigned to direct shakeup configurations, neither ^2S nor a monopole $3p \rightarrow np\ ^2P$ state. As for the $3s^23p^4nd$ states, they are large and decreasing slowly over the energy range of the experiment (60-120 eV). Once Kossman et. al. firmly established the presence of more satellites, the controversy surrounding the intensities of the satellites at the sudden limit and the energy dependence from the Cooper minimum to the sudden limit resolved itself. The differences in the relative intensities were artifacts of experiments with low and differing resolutions. Attention now focussed on the satellites at lower incident energies. The work of Adam et. al. and to some extent Kossman et. al. indicated that there are prominent lower binding energy satellites which decrease from threshold to near invisibility at the sudden limit. Also theoretical work by Wijesundera and Kelly[14] suggested that the behavior of the FISCI satellites ($^2S\ 3s^23p^4nd$) near threshold was more interesting than previous work suggested.

They calculated explicitly the energy dependence of these satellites using Many Body Perturbation Theory (MPBT). The energy dependence of the $3s^23p^44d\ ^2S$ and $3s^23p^45d\ ^2S$ satellites were calculated to be quite similar. They both start at a minimum

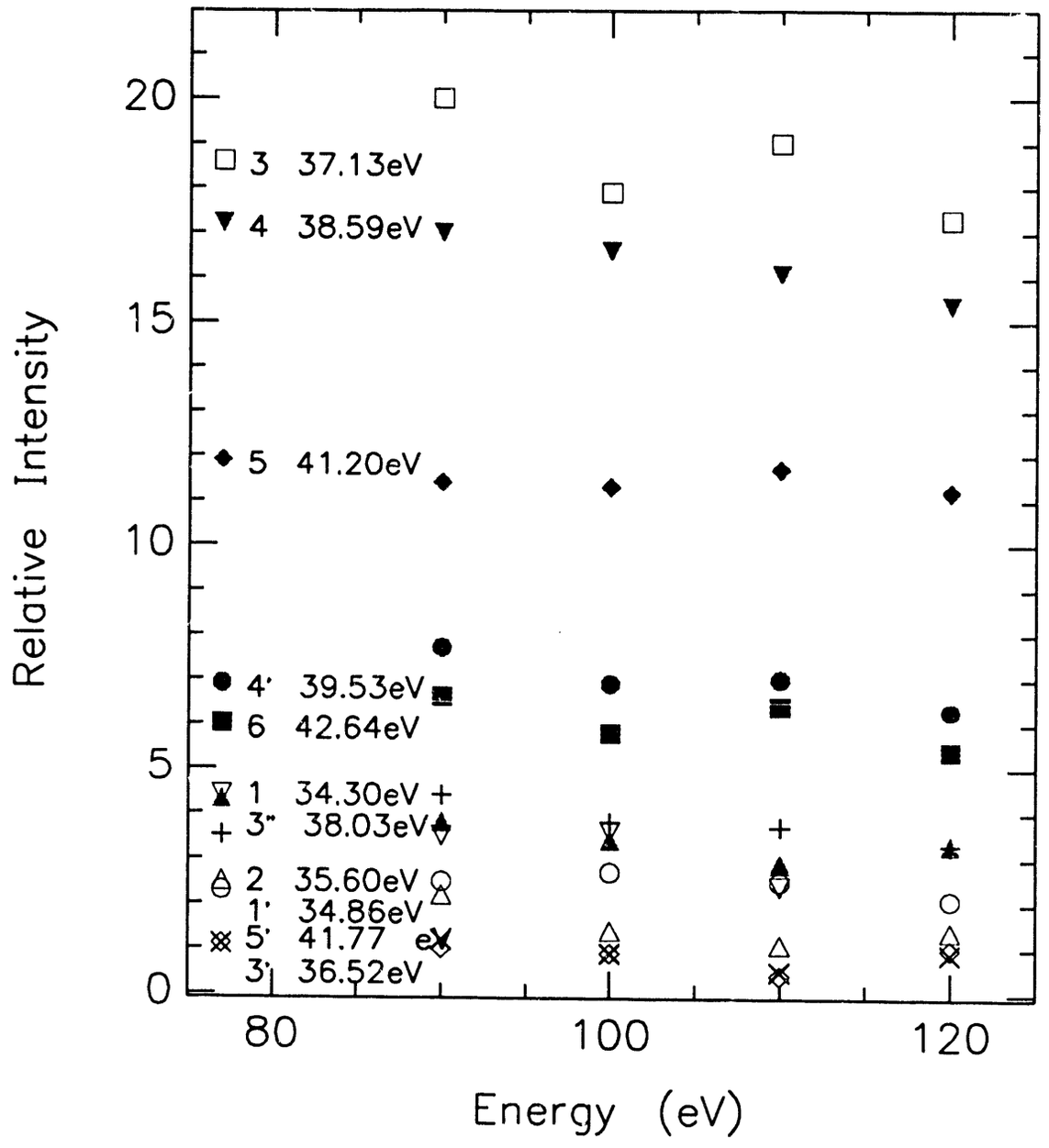

FIGURE 1.2 Intensities of satellites, as percent of the 3s mainline, from ref. 11 as a function of energy. Symbols are the same as figure 1.1 for satellites present in both.

at threshold and rapidly increase over a range of about 15 eV to a low maximum. They then very slowly decrease. The results of Adam et. at. confirm this, since at very low kinetic energies they are not visible (implying low cross section), and at higher energies they are roughly constant. The $3s^2 3p^4 3d\ ^2S$ state, however, was calculated to have its greatest intensity at threshold and rapidly decrease to a Cooper minimum at approximately 45 eV incident energy. It then rises to another low maximum at approximately 75 eV and slowly decreases to the sudden limit. The results of Adam et. al. unfortunately track this satellite only down to 57 eV, and this Cooper minimum in a satellite was unseen until the work of Becker et. al.[15]

Becker et. al. studied the satellites of Ar from 32 eV to 100 eV, and they measured the Cooper minimum structure in the $3s^2 3p^4 3d\ ^2S$ satellite. They also show examples of the different types of near threshold behavior for satellites, tracking the mainline or a constant branching ratio, enhancement on an autoionizing resonance, and intense at threshold and rapidly decreasing.

Threshold Spectra

Previously the zero kinetic energy (ZKE) spectra of neon and helium have been studied intensively.[16] In the case of helium, it was possible to compare the results with accurate calculations. The hydrogenic final states monotonically decrease in intensity as n gets larger, and measurements of the angular distribution at low kinetic energies (0.6 eV) indicate that as the electron is excited to higher n states, l is excited preferentially to greater values. Both of the results have been confirmed theoretically.

For neon the ZKE spectrum is much more complex. In contrast to high kinetic energy results, quartet states appear, breaking the $\Delta S = 0$ selection rule. States of high angular momentum, ^2F for example, are prominent and the ^2S and ^2P states which

dominate at the sudden limit are not very intense. Some states have appreciable intensity only at their thresholds, which coincide with doubly excited states of neutral neon. Like helium l increases with increasing n. Within a given Rydberg series, however, the intensities do not appear to decrease monotonically with increasing n.

Argon

Figure 1.3 is the Argon $3s^{-1}$ ZKE spectrum, with the sudden limit satellites from table 1.1 indicated . This spectrum was taken at SSRL on beamline IIIa, with a spherical grating monochromator. The analyzer was oriented 54.4° to the polarization vector. The spectrum has not been corrected for second order light, but the cross sections reported in table 1.4 have been. The cross sections were determined by comparison with 3s-1 cross section as calculated by Huang et. al..[17] Since the spectrum is so congested, a spectrum with finer point density is presented in figure 1.4.

It is apparent from the spectra that the lower binding energy satellites are prominent in the threshold spectrum, while those close to the double ionization threshold are suppressed. Also in the threshold spectrum none of the peaks are assigned to n >4. This is very different from He where n=10 is clearly visible and Ne, where n ranges ashigh as 5. Part of the explanation for this must be the 3d subshell, which supplies many low lying states.

In the low binding energy region of the satellite spectrum several quartet states are observed. Intersystem combinations have been previously observed,[5] so this simply implies a breakdown of L-S coupling. There is no evidence to indicate that the j-j coupling selection rule $\Delta J = 0, 1$ is violated. However for some of the high angular momentum states of the ion, the photoelectron must also have high angular momentum. In particular for the ^2G (binding energy = 34.92 eV), the outgoing electron must be εf,

Assignment	Optical Energy[a]	Sudden Limit		Threshold	
		Energy[b]	σ(Mb)[b]	Energy[c]	σ(Mb)[c]
$3s^{-1}\,^2S$	29.24	29.24	0.80		
$3p^{-2}(^3P)3d\,^4D$	32.18			32.21	0.045(4)
$3p^{-2}(^3P)4s\,^4P$	32.46			32.52	0.030(3)
$3p^{-2}(^3P)4s\,^2P_{3/2}$	32.90			32.93	0.063(5)
$3p^{-2}(^3P)4s\,^2P_{1/2}$	33.02			33.04	0.014(3)
$3p^{-2}(^3P)3d\,^4F_{5/2}$	33.50			33.52	0.024(2)
$3p^{-2}(^3P)3d\,^4F_{3/2}$	33.53			33.60	0.016(2)
$3p^{-2}(^3P)3d\,^2P_{1/2}$	33.70			33.72	0.069(5)
$3p^{-2}(^3P)3d\,^2P_{3/2}$	33.82			33.84	0.248(13)
$3p^{-2}(^3P)3d\,^4P$	34.06			34.05	0.018(2)
$3p^{-2}(^1D)4s\,^2D_{3/2}$	34.18			34.11	0.020(2)
$3p^{-2}(^1D)4s\,^2D_{5/2}$	34.21			34.24	0.177(10)
$3p^{-2}(^3P)3d\,^2D$	34.49	34.50	0.0004	34.43	0.060(4)
$3p^{-2}(^1D)3d\,^2G$	34.88			34.92	0.017(2)
$3p^{-2}(^3P)4p\,^4P$	35.01			35.02	0.012(2)
$3p^{-2}(^3P)4p\,^4D$	35.30			35.36	0.023(2)
$3p^{-2}(^3P)4p\,^2D$	35.44			35.50	0.051(4)
$3p^{-2}(^3P)4p\,^2P_{1/2}$	35.56			35.57	0.034(3)
$3p^{-2}(^3P)4p\,^2P_{3/2}$	35.62	35.64	0.0048	35.66	0.033(3)
$3p^{-2}(^1D)3d\,^2F$	36.03			36.06	0.115(7)
$3p^{-2}(^1S)4s\,^2S$	36.50	36.52	0.0048	36.55	0.016(2)
$3p^{-2}(^1D)4p\,^2F$	36.89			36.96	0.038(3)
$3p^{-2}(^1D)4p\,^2P$	37.11	37.15	0.0296		
$3p^{-2}(^1D)3d\,^2D$	37.18			37.18	0.054(4)
$3p^{-2}(^1D)4p\,^2D$	37.25			37.29	0.070(5)
$3p^{-2}(^1D)3d\,^2P$	37.40			37.48	0.024(3)
^2P	38.04			38.10	0.043(4)
$3p^{-2}(^1D)3d\,^2S$	38.58	38.60	0.149	38.66	0.019(2)
$3p^{-2}(^3P)4d\,^2P$	39.39			39.45	0.028(2)
$3p^{-2}(^1S)4p\,^2P$	39.57	39.57	0.012		
$3p^{-2}(^3P)4d\,^2D$	39.64			39.70	0.022(2)
$3p^{-2}(^1D)4d\,^2S$	41.20	41.21	0.075	41.24	0.027(3)
		42.67	0.033		
		43.43	0.012		
		44.00	0.0040		
sat. total			0.325		1.49

Table 1.4 Argon Satellites at Threshold

a. C. E. Moore, Ref. 5

b. Svensson et. al. Ref. 6

c. This work

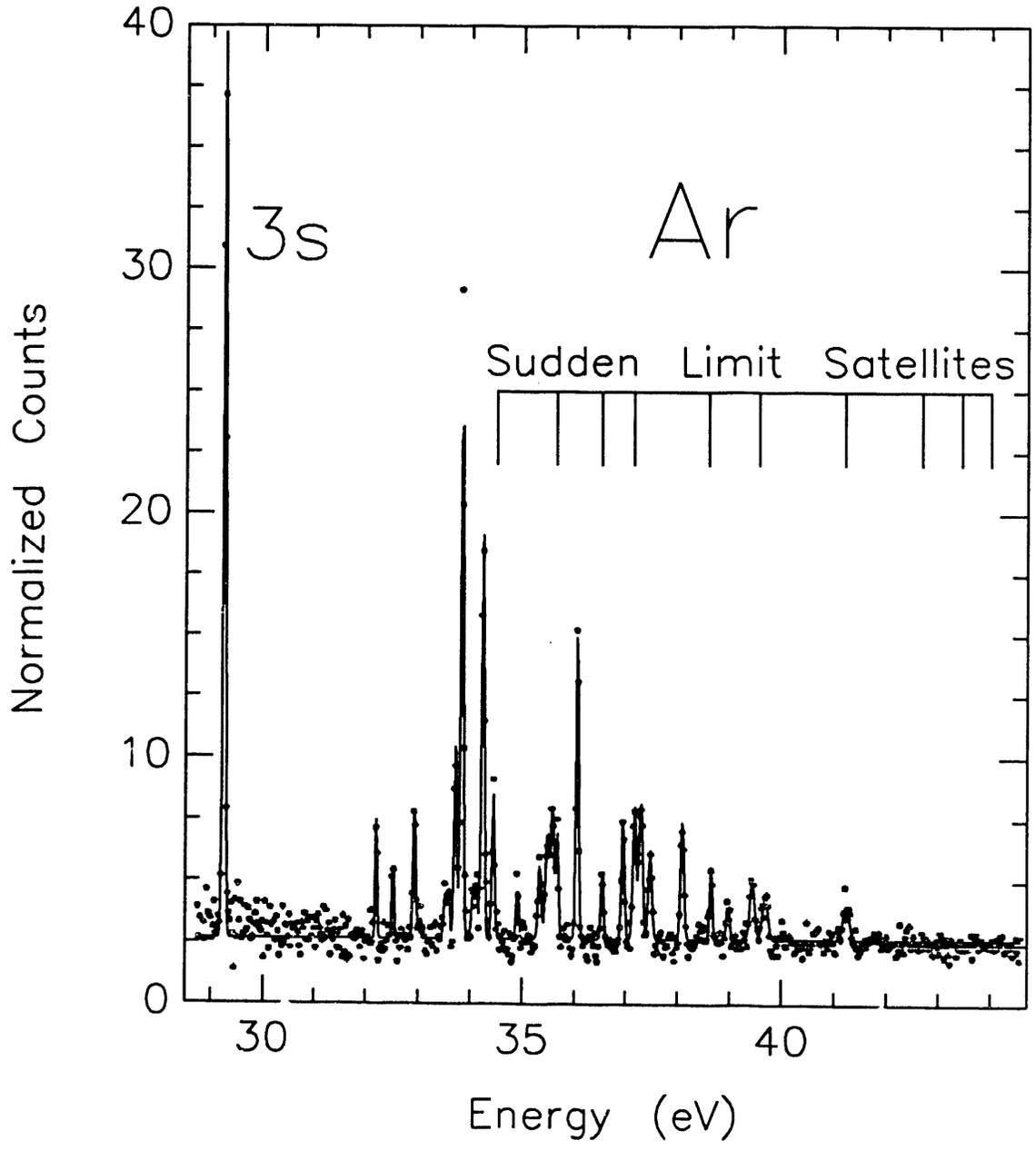

FIGURE 1.3 ZKE spectrum of Ar from $3s^{-1}$ threshold to the double ionization limit. The solid line is a least squares fit to the data.

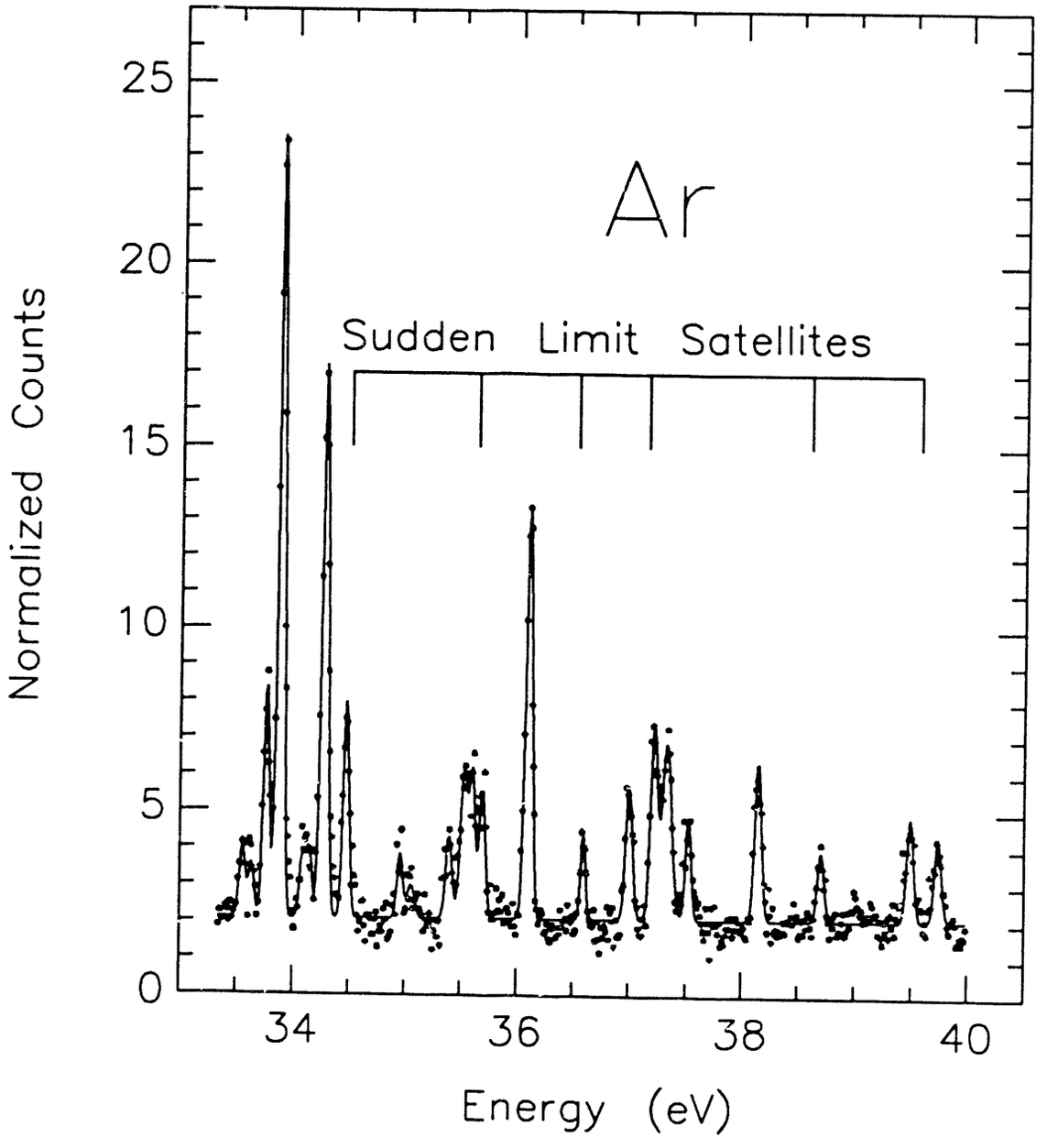

FIGURE 1.4 Same as figure 1.3 with a finer point density.

because of the ΔJ selection rule and the Laporte rule. These high angular momentum states have previously been attributed to the interaction between the ionized electron and the excited electron. In the Wannier model[18] of double ionization, the two electrons have large angular correlation, and according to Fano[19] unstable radial correlation. Previous explanations viewed ionization into a satellite channel near threshold as failed double ionization, then an electron departing with zero kinetic energy exchanges angular momentum with the excited electron for a long time. The two electrons move out through two narrow cones 180° apart. If the kinetic energy of one electron exceeds that of the other, it begins to feel the potential from the ion decrease and the electron accelerates, leaving the other electron in a highly excited orbital.

However, Wannier's original description is slightly different. The two electrons leave the ion with the two vectors $\mathbf{r}_1$, and $\mathbf{r}_2$ and γ = the angle between them. A change into scalar coordinates gives:

$$r_1 = r \cos \chi/2 \qquad 1$$
$$r_2 = r \sin \chi/2 \qquad 2$$
$$0 \leq \chi \leq \pi \qquad 3$$

Now r represents the progress of the reaction, and χ, defined by equations 1 and 2, the relative distance each electron travels from the nucleus. In terms of the variable r, there exist three different zones, the reaction zone, the coulomb zone, and the free zone. The reaction zone is inside the complex atomic potential, and the Coulomb zone is where the electrons experience a simple Coulombic potential. The boundary between the reaction zone and the Coulomb zone is taken to be on the order of the Bohr radius. Since the free zone is the distance where there is no potential, the boundary between the Coulomb zone and the free zone is a function of the kinetic energy. For zero kinetic energy electrons the boundary between the Coulomb zone and the free zone is at infinity. If $\chi = 0$ or π, it is apparent from equations 1-3 that this leads to a single escape, and $\chi = \pi/2$ leads to double escape. Figure 1.5 taken from Wannier[18] shows the geometry with respect to χ

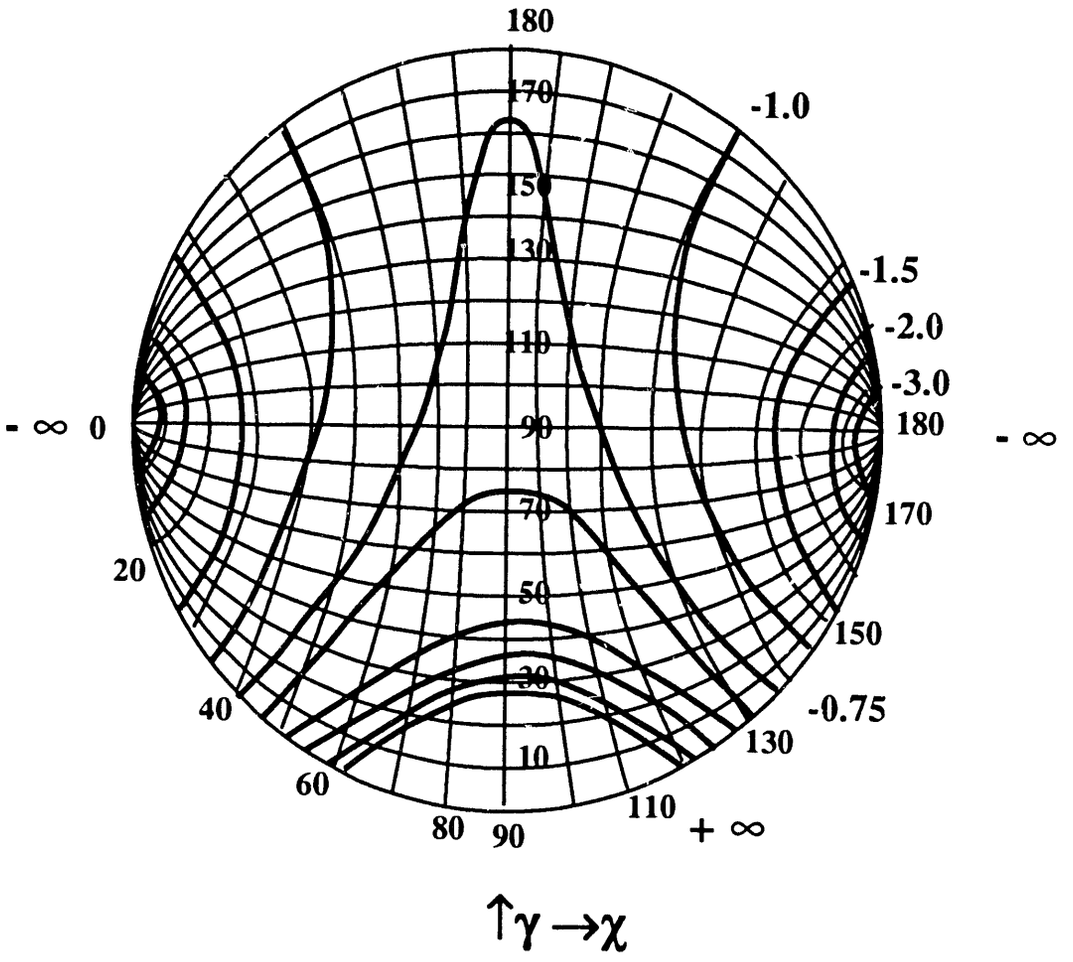

FIGURE 1.5 Two-dimensional projection of the potential for two interacting electrons leaving an atom as a function of γ, the angle between them, and χ, which determines their relative velocities

and γ at the threshold for double ionization. The unstable equilibrium point at $\gamma = \pi$, and $\chi = \pi/2$ corresponds to double escape, and the deep minima at $\chi = 0$ and $\chi = \pi$ correspond to single escape. Wannier also applies this description to small energies above threshold.

> "In this semi intuitive approach to orbits of finite ε we first observe . . . that there is no difference between the orbits of zero energy and of small energy in the reaction and Coulomb zones. . . . It is then intuitively reasonable that all orbits which led to double escape at zero energy will continue to do so at finite ε. . . . .However, because the energy is finite, other orbits will also be possible now."[18]

If, in contrast, we look at the orbits corresponding to energies lower than the double ionization energy, we can make a similar statement. There is still no difference in these orbits in the reaction zone. However, now at least one electron remains in the Coulomb zone. Looking at the orbits for double ionization, both electrons should be approximately equidistant from the ionic core, and neither has sufficient energy to escape the Coulomb zone. For single escape each of the states in table 1.2 corresponds to an orbit. As we decrease the energy further, single ionization orbits become one by one energetically inaccessible and both electrons remain bound. They still leave the reaction zone in that orbit, but the outgoing electron is trapped in the Coulomb zone, causing the two electron resonances visible in the absorption spectrum.[20] This description is simply equivalent to the two electron Rydberg series being continuous as $n \rightarrow \infty$. The orbit, single or double escape, is determined before any electron leaves the reaction zone with χ equal to any value for single escape.

Madden, Ederer, and Codling[20] have measured and assigned the two electron resonances between 29.24 eV and 43.38 eV. A comparison of their results and the satellite spectrum at zero kinetic energy reveals that the most prominent double ionization series culminate in the most prominent satellites. Almost all the satellites, which are

present at threshold, have at least one member of their Rydberg series visible in the absorption spectrum. Three satellites are unambiguously assigned to states without any previously determined Rydberg states. These are ^4D (binding energy = 32.21 eV), ^4F (binding energy = 33.52 eV), and ^2F (binding energy = 36.06 eV). The ^4D state occurs between two strong Rydberg states leading to $^2P_{3/2}$ (binding energy =32.90 eV) and $^2P_{1/2}$ (binding energy = 33.72 eV) satellites. The others appear at energies equal to a doubly excited states. This is not to be greatly emphasized: since there are so many doubly excited states, it is harder to find a satellite without a doubly excited state at the same energy, and almost all of the resonances have Fano profiles with q's which indicate that they strongly interact with one or more continua. The most important interactions near threshold are still between the various single escape orbits, since they are much more numerous than the double escape orbits.[18] This is apparent from the deep mimima at the single escape points in the potential in fig. 1.5.

As the double ionization threshold is approached, fewer quartet and high angular momentum states are visible in the satellite spectrum. Perhaps since the number of accessible single ionization channels is greater here, other considerations, such as symmetry, are more important for interaction between doubly excited states and satellites than energy. Fluorescence measurements[21] and photoelectron studies[15] have shown that some Ar $3s^{-1}$ satellites are enhanced at resonances with energies not coincident with their thresholds.

At threshold, direct <u>two</u>-electron transitions produce satellites, by autoionization of the double escape orbits and energetically inaccessible single escape orbits into the accessible single escape orbits or direct ionization into <u>two</u> electron single escape orbits. The basic structure of satellites spectra are determined in the reaction zone, where a detailed quantum mechanical description is necessary. The only Ar $3s^{-1}$ satellites, calculated as a function of kinetic energy, are the $3s^23p^4nd\ ^2S$ states calculated by

Wijesundera and Kelly,[14] using MBPT. Their results differ from our results at threshold. For the $3s^2 3p^4 3d\ ^2S$ state, they calculate $\sigma = 0.45$ Mb. Since this area of the spectrum does not have excellent signal to noise, and the theoretical cross section for 3d shows much variation close to threshold, it is dangerous to say conclusively that the data do not support the theory.

The threshold spectrum in this case contributes to an understanding of the X-ray spectrum. Since the binding energies for the valence satellites cannot change as a function of incident light energy, the assignment of peak 1 in table 1.3 should be $3s^2 3p^4 3d\ ^2D$. This implies that even at the sudden limit satellites are not strictly restricted to the mainline symmetry, and direct two-electron transitions are still present.

Krypton

Figure 1.6 is the satellite spectrum of krypton from the 4s ionization threshold to the double ionization threshold. This spectrum was taken at NSLS on Beamline I, an extended range spherical grating monochromator. The analyzer was oriented at 90° relative to the polarization vector of the radiation. The results are summarized in table 2.5. The spectrum is not corrected for higher order light, but the tabulated values are. The allowed transitions are the same as for the Ar $3s^{-1}$. The figure also shows the positions of the satellites measured at high kinetic energy from Svensson et. al.[6]

Even though the signal-to-noise ratio is inferior this spectrum, and angular distribution effects may be present, it is still apparent that several lower binding-energy satellites are present in the threshold spectrum which are absent at the sudden limit. As with argon, high angular momentum and quartet states are present at threshold. The important satellites at the sudden limit are again the $4s^2 4p^4 nd\ ^2S$ series, and this has been predicted theoretically.[4] However, the assignment of all the sudden limit satellites

		Sudden Limit		Threshold	
Assignment	Optical Energy[a]	Energy[b]	σ(Mb)[b]	Energy[c]	σ(Mb)[c]
$4s^{-1}\ ^2S$	27.52	29.52	0.63	27.52	0.63
$4p^{-2}(^3P)5s\ ^4P_{5/2}$	27.99			27.99	0.020(2)
$4p^{-2}(^3P)5s\ ^4P_{3/2}$	28.27			28.28	0.0120(12)
$4p^{-2}(^3P)5s\ ^4P_{1/2}$	28.58			28.59	0.109(5)
$4p^{-2}(^3P)4d\ ^4D$	28.90			28.94	0.073(4)
$4p^{-2}(^3P)4d\ ^4F_{9/2}$	29.62			29.59	0.056(2)
$4p^{-2}(^1D)5s\ ^2D$	29.82			29.81	0.097(4)
$4p^{-2}(^3P)4d\ ^4F_{7/2}$	29.86				
$4p^{-2}(^3P)4d\ ^4P$	30.25	30.25	0.0069	30.26	0.0160(13)
$4p^{-2}(^3P)5p\ ^4P_{5/2}$	30.60			30.63	0.050(3)
$4p^{-2}(^3P)5p\ ^4P_{3/2}$	30.65				
$4p^{-2}(^3P)4d\ ^2D_{5/2}$	30.68				
$4p^{-2}(^3P)4d\ ^2P_{3/2}$	30.69				
$4p^{-2}(^3P)3d\ ^4P$	31.15				
$4p^{-2}(^1D)4s\ ^2D_{3/2}$	31.17			31.19	0.113(5)
$4p^{-2}(^1D)4s\ ^2D_{5/2}$	31.24	31.25	0.011		
				31.91	0.023(2)
$4p^{-2}(^1S)5s\ ^2S$	32.08	32.09	0.014	32.01	0.093(4)
$4p^{-2}(^1D)4d\ ^2F_{5/2}$	32.49			32.48	0.114(5)
$4p^{-2}(^1D)4d\ ^2F_{7/2}$	32.56				
$4p^{-2}(^1D)4d\ ^2D$	32.57			32.57	0.042(2)
$4p^{-2}(^1D)4d\ ^2F$	32.63				
$4p^{-2}(^1D)5p\ ^2P$	32.68	32.75	0.056	32.77	0.095(4)
$4p^{-2}(^1D)4d\ ^2P$	32.83				
$4p^{-2}(^1D)5p\ ^2D$	32.87			32.91	0.011(1)
$4p^{-2}(^3P)5d\ ^4P_{1/2}$	33.93			33.82	0.031(2)
$4p^{-2}(^3P)5d\ ^4P_{5/2}$	33.96			33.93	0.044(3)
$4p^{-2}(^3P)5d\ ^4D$	34.03				
$4p^{-2}(^3P)6s\ ^2P_{3/2}$	34.09	33.98	0.150		
$4p^{-2}(^3P)5d\ ^4F_{5/2}$	34.46				
$4p^{-2}(^3P)5d\ ^2P_{3/2}$	34.47	34.47	0.014		
$4p^{-2}(^3P)5d\ ^2F_{7/2}$	34.61				

Table 1.5 Krypton Satellites at Threshold

a. C. E. Moore, Ref. 5.

b. Svensson et. al., Ref. 6.

c. This work.

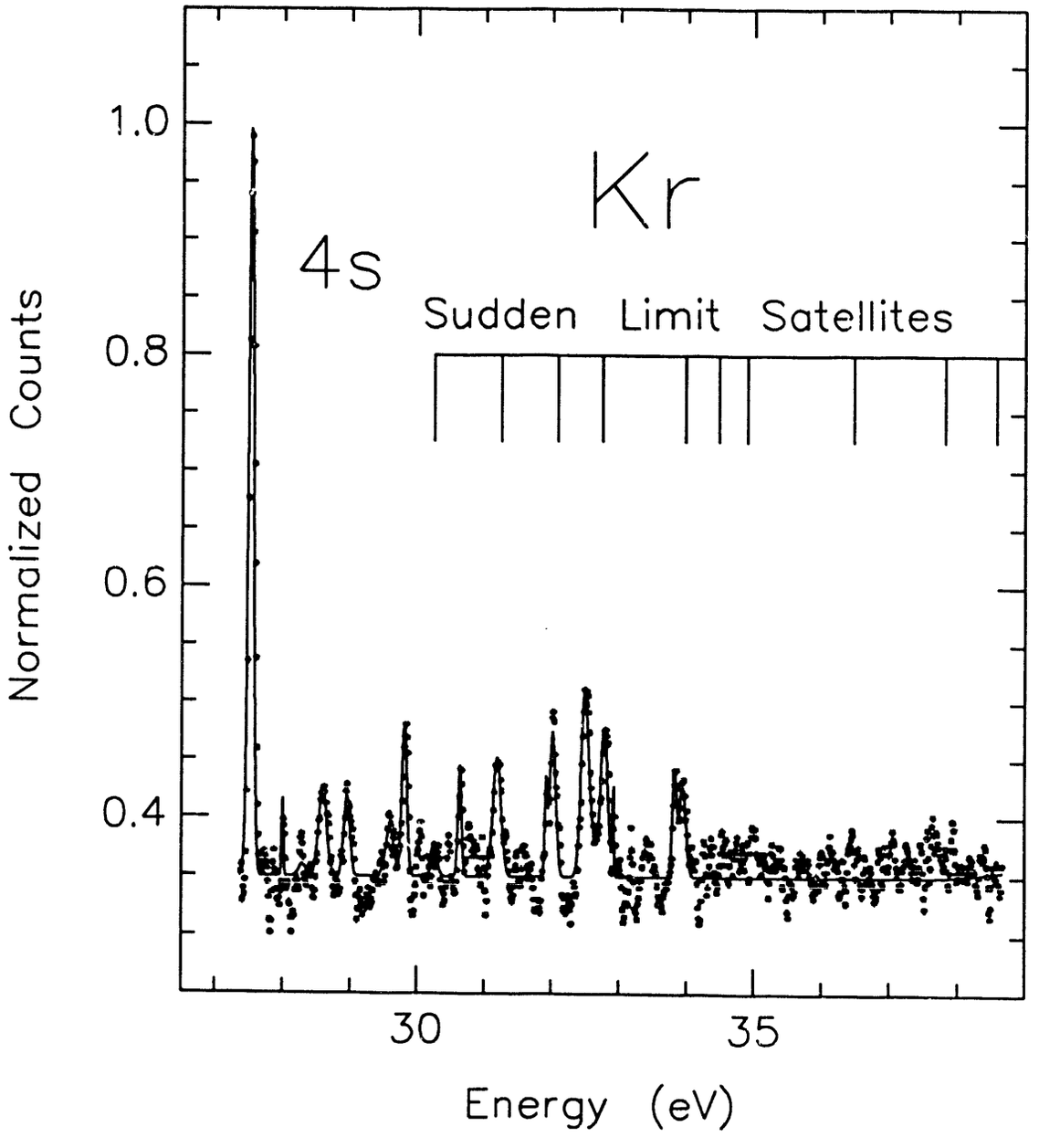

FIGURE 1.6 ZKE spectrum of Kr from $4s^{-1}$ threshold to the double ionization limit. The solid line is a least squares fit to the data.

		Sudden Limit		Threshold	
Assignment	Optical Energy[a]	Energy[b]	σ(Mb)[b]	Energy[c]	σ(Mb)[c]
$4p^{-2}(^3P)5f\ ^4F$	34.85				
$4p^{-2}(^3P)5f\ ^2F$	34.87				
$4p^{-2}(^3P)5f\ ^2D$	34.91				
$4p^{-2}(^3P)5f\ ^4D$	34.92				
$4p^{-2}(^1S)5p\ ^2P$	34.92	34.90	0.013		
$4p^{-2}(^1D)5d\ ^2S$		36.47	0.067		
$4p^{-2}(^1D)6p\ ^4D$					
$4p^{-2}(^1D)6d\ ^2S$		37.81	0.032		
$4p^{-2}(^1D)7d\ ^2S$		38.57	0.019		
$4p^{-2}(^1D)8d\ ^2S$		39.21			
$4p^{-2}(^1D)nd\ ^2S$		39.77	0.010		
sat. total			0.393		1.00

Table 1.5 cont. Krypton Satellites at Threshold
a. C. E. Moore, Ref. 5.
b. Svensson et. al., Ref. 6.
c. This work.

as ^2P and ^2S states seems to be wrong for krypton also. The satellite with a binding energy of 30.25 eV especially is much more likely the ^2D (30.68 eV) or ^2D (29.82 eV) state than the ^2P state at 30.69 eV. Therefore, as with argon, some intrinsically two-electron transitions can be present at the sudden limit. This makes the theoretical calculation of energies and intensities much more difficult without symmetry restrictions.

The quartet-doublet combinations, however, only appear in the threshold region, and they seem to be restricted even there to combinations involving low binding energy quartet states.

Xenon

The xenon $4d^{-1}$ subshell is more complex than the valence shell systems. There are several open single and double ionization orbits. The most important in this energy

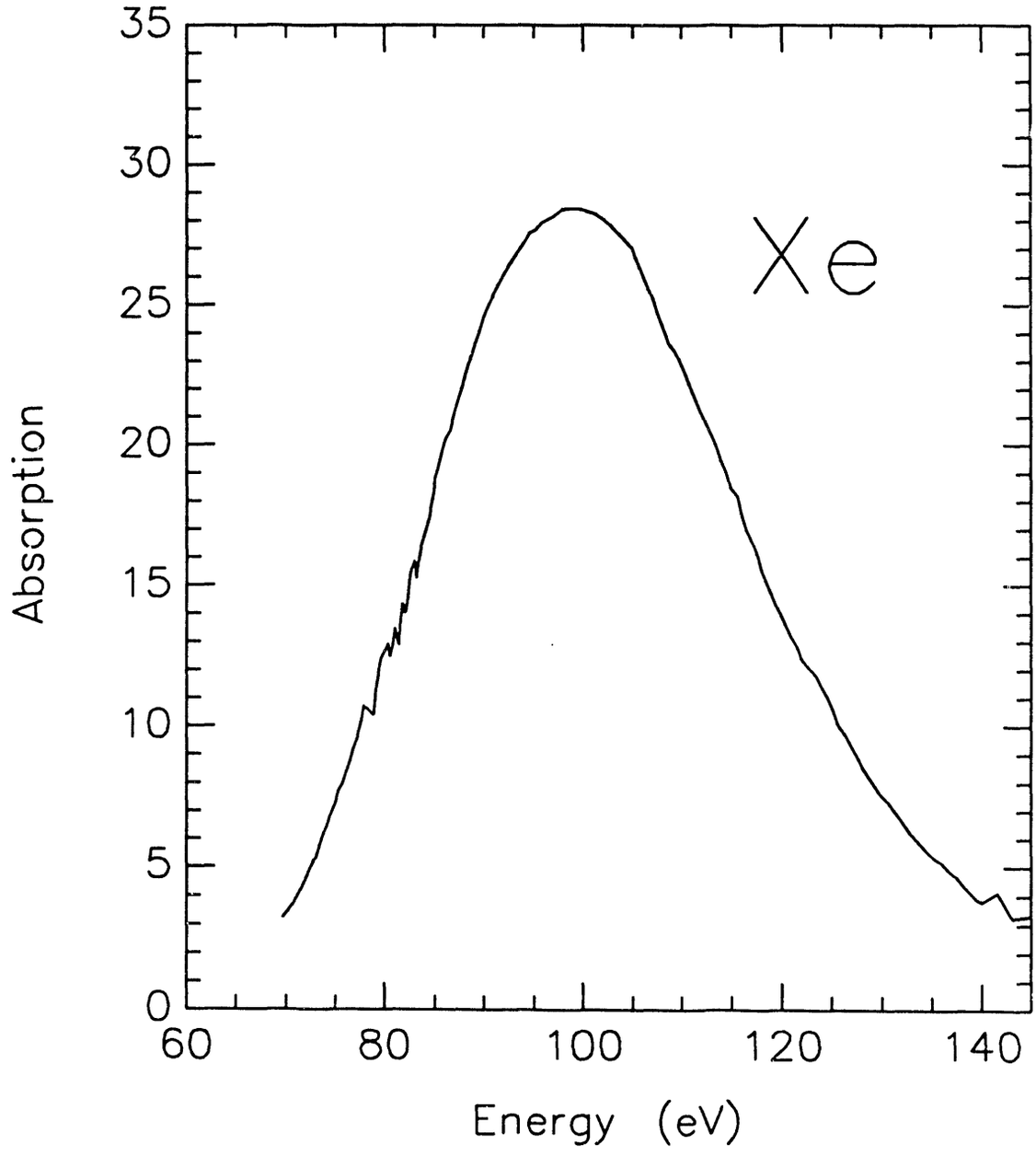

FIGURE 1.7 Absorption spectrum of Xe (ref. 22), showing the delayed onset from the centrifugal barrier in the εf ionization channel.

range are the $4d^{-1}\ ^2D_{5/2}$ (binding energy = 67.5 eV) and $^2D_{3/2}$ (binding energy = 69.5 eV) mainlines. They go through a delayed maximum at 100 eV, because of the centrifugal barrier for the outgoing εf electron. The absorption spectrum of xenon is shown in figure 1.7.[22] A ZKE spectrum at a core-level looks very different from the valence spectra. Since the energy is above the double ionization limit, discrete absorption resonances can relax by emitting two electrons simultaneously. Sometimes one of these electrons has zero kinetic energy. Therefore, discrete resonances appear in ZKE spectra of core-levels.[23] For the Xe $4d^{-1}$ case, the triple ionization energy is 65.43 eV, so the 4d ionized states can relax by emission of two electrons simultaneously also. Therefore, for a core-level subshell the ZKE spectrum should have a background which mimics the absorption spectrum. The mainline and satellites peaks will sit on top of this.

Core-level spectra are further complicated by Post-Collision Interaction (PCI). In the semiclassical description,[24] when an atom emits a low energy electron from a core orbital, and subsequently this ion relaxes by Auger decay, if the Auger electron has a greater kinetic energy than the original photoelectron, the Auger electron passes the photoelectron and their potentials change. The Auger electron is now in the field of a singly charged ion. It gains kinetic energy, and the photoelectron loses kinetic energy. For spectra where the incident energy is scanned, this results in the threshold peaks broadening asymmetrically and the maximum intensity does not occur at its threshold, but slightly higher incident energy.

Figure 1.8 is the satellites spectrum of the Xe $4d^{-1}$ subshell with the absorption spectrum,[22] and the XPS spectrum.[6] This spectrum was taken at SSRL Beamline IIIa, with a grasshopper monochromator. The analyzer was at 54.7° to the polarization vector of the radiation. At the top of the spectrum are the results of a ΔSCF calculation, which gives some idea of the electronic configurations of the satellites. However, a calculation of the satellites' energies of Xe $4d^{-1}$ in the intermediate coupling scheme has found 36

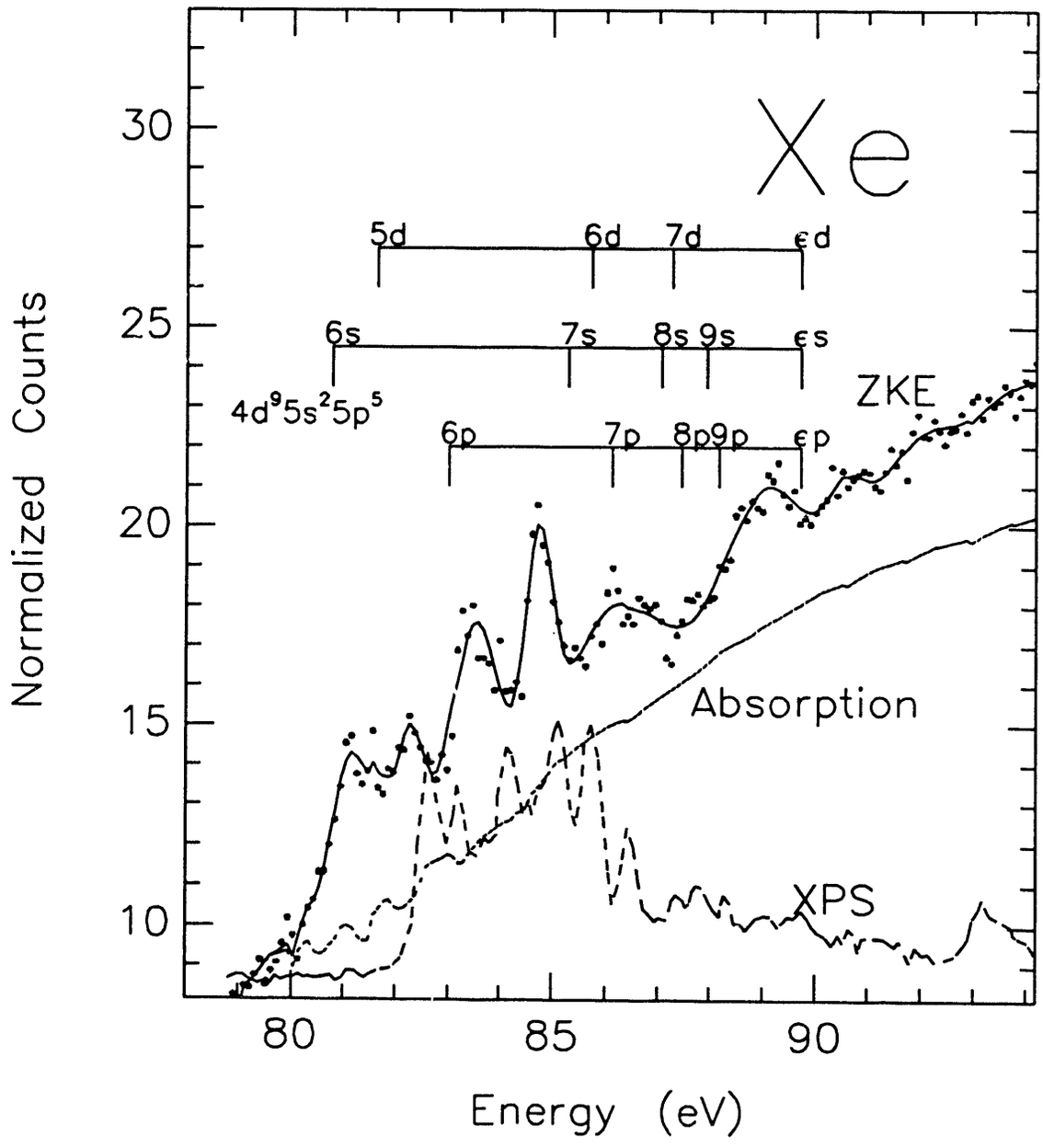

FIGURE 1.8 ZKE spectrum of Xe over the $4d^{-1}$ satellite region with absorption (ref.22) and XPS (ref.6).

satellites[6] between 81.7 eV and 86.7 eV, all with the configuration $4d^9 5s^2 5p^5 6p\ ^2D$. So the calculation displayed on the figure is not meant to imply any definite assignment of the spectrum. The most intense peaks, however appear at energies which roughly correspond to the $4d^9 5s^2 5p^5 6s$, $4d^9 5s^2 5p^5 5d$, and $4d^9 5s^2 5p^5 6p$ states.

It is clear that the ZKE spectrum is not simply the sum of the XPS and absorption spectra. As with the simpler valence satellites, low binding energy satellites are enhanced, which are not present at the sudden limit. It is also possible that some of these states are conjugate shakeup states. Including PCI effects the lowest binding energy satellites calculated by Svensson et. al. of the configuration $4d^9 5s^2 5p^5 6p\ ^2D$ should have a maximum at 81.9 eV. This is one eV greater than the first satellite in figure 1.8. Therefore it is possible that some the states present at threshold correspond to symmetries different from the mainline.

Conclusions

Satellites at zero kinetic energy are strongly influenced by the presence of doubly excited states, both the Rydberg series for double escape and the Rydberg series' of higher binding energy satellites. At energies where this resonant interaction is possible quartet-doublet intersystem crossing is observed. These quartet satellite states are not visible at higher energies. In contrast, the conjugate states are present at their threshold and also present, with less intensity, at higher kinetic energies, and discrepancies between theory and experiment may exist because the calculations include only satellites with the same symmetry as the mainline.

The inner shell case of xenon indicates that for many electron systems the lower binding energy satellites are enhanced at their thresholds, and the presence of many low energy ionic states does not influence this phenomenon. The most significant interaction

is solely between other 4d-hole states, even when the doubly excited states can relax by an Auger-like process.

Chapter 2 Vibrationally Resolved Threshold Spectra of N_2 and CO at the N-1s and C-1s Edges

Two of the most widely studied small molecules are N_2 and CO. Whereas experimentally they are easy to study, calculations of even the simplest properties require the inclusion of electron correlation. For N_2, as was mentioned in Chapter 1, electron correlation must be included to calculate the energy ordering of the valence orbitals. Similarly, the calculation of the dipole moment of CO requites electron correlation to achieve even the correct sign.[2] Many facets of the core-level ZKE spectra of N_2 and CO, however, can be explained by the very simple, equivalent-core model, which was first proposed in 1934 by Prins.[3] First I will present a brief summary of previous studies and the equivalent-core explanation of these. Then, I will apply this model to my results for N_2 and CO, using ZKE-PES, and for the satellite region compare this with other theoretical results.

Table 2.1 shows the molecular orbitals for N_2 and CO, their occupancy, and their ionization potentials for the occupied orbitals. Previously the neutral transitions of the core electrons have been studied by EELS[4,5] and most recently by high resolution photoionization.[6,7] Figure 2.1 shows the photoionization spectrum of Chen et. al.[6] The lowest energy peak corresponds to a N1s$\rightarrow 1\pi_g^*$ transition, with vibrational structure. This is followed by transitions to Rydberg-like orbitals, which lead up to the 1s

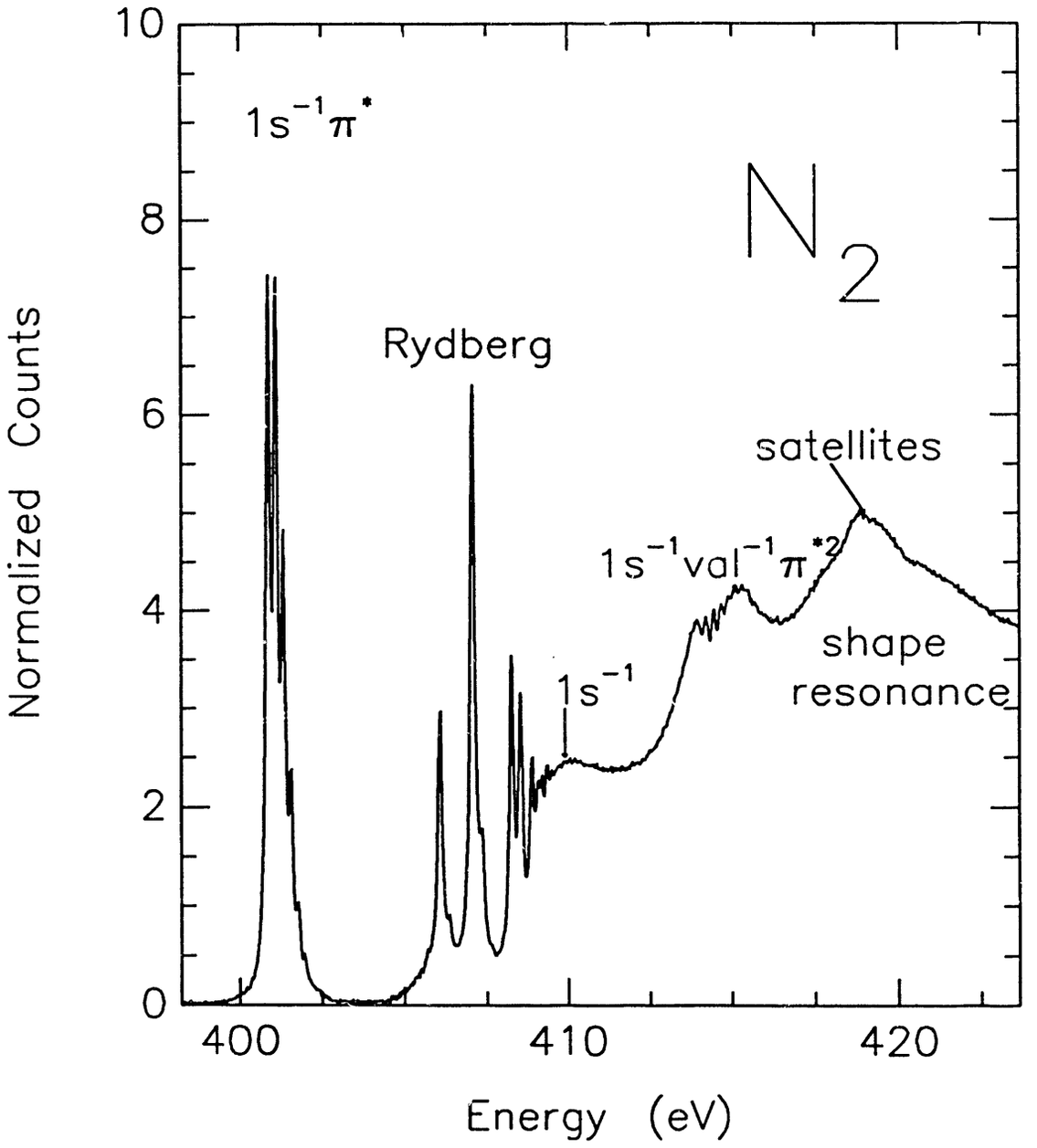

FIGURE 2.1 Absorption spectrum of N_2; at photon energies above the $1s^{-1}\pi^*$ resonance, the spectrum has been enlarged 10 times.

Molecular Orbitals for N_2	Occupancy		Ionization Potential	
			N_2	CO
σ_u				
$1\pi_g$				
$3\sigma_g$	↑↓		15.58 eV	14.01 eV
$1\pi_u$	↑↓ ↑↓		16.70 eV	16.58 eV
$2\sigma_u$	↑↓		18.75 eV	19.70 eV
$2\sigma_g$	↑↓		37.9 eV	38.9 eV
$1\sigma_u$	↑↓	C(1s)	409.98 eV	296.24 eV
$1\sigma_g$	↑↓	O(1s)	409.98 eV	542.57 eV

Table 2.1 N_2 and CO Molecular Orbitals

ionization threshold. The equivalent-core model describes these electronic states in terms of the states of NO. If the core hole is localized on one N-atom, the nucleus plus core electrons now appear to the valence electrons to be an O-atom, and the outer electrons experience a potential like the NO molecule. Similarly the equivalent-core states for C-1s excited states are also the states of NO. Therefore for both molecules the

Transition	CO[a]			N_2[b]			NO[c]			
1s→	R_e (Å)	ω_e (eV)	Term Energy (eV)	R_e (Å)	ω_e (eV)	Term Energy (eV)	R_e (Å)	ω_e[d] (N_2) (eV)	ω_e[d] (CO) (eV)	Term Energy (eV)
π^*	1.153	269	8.68	1.164	235	9.07	1.151	244	246	9.264
$3s\sigma$	1.077	307	3.712	1.077	293	3.788	1.063	304	304	3.799
$3p\pi$	1.073	309	2.749	1.073	300	2.793	1.062	307	310	2.786
$3d\pi$	1.08	309	1.466				1.059			1.503
$4p\pi$	1.083	292	1.277			1.310				1.309
ground state	1.128	269		1.098	292					

Table 2.2 Equivalent Core Comparison

a. Domke et. al., Ref. 7.

b. Chen et. al., Ref. 6.

c. K. P. Huber and G. Herzberg, *Molecular Spectra and Molecular Structure* (Van Nostrand, Princeton, 1979), Vol 4, and references therein.

$1s \rightarrow \pi^*$ transition can be compared to the ground state of NO, and the Rydberg series can be compared to the Rydberg series converging on the NO^+ X-state. Table 2.2 lists the results of Chen et. al. and Domke et. al. for N_2 and CO, respectively, and the equivalent core states of NO. The bond lengths were determined by performing a Franck-Condon analysis. In both cases, the parameters listed in table 2.2 do not agree within their uncertainty with the equivalent core states. However, the agreement is satisfactory enough to provide an assignment of the spectra.

Beyond the 1s-ionization limit there are several sharp structures, which are doubly excited neutral states. They were assigned not solely on the basis of energy, but also because this structure is present in EELS and absorption, and absent in photoelectron spectra.[8] The broad maximum at 420 eV and extending over a 10 eV range is a σ^* shape resonance. This phenomenon is primarily a one-electron effect, and is similar to the broad delayed maximum in the xenon 4d cross section. In this case the antibonding σ^* molecular orbital lies above the 1s ionization threshold, but still in the inner well. Electrons excited into this state escape through the $1s^{-1}$ channel. Partial cross section measurements[9] of the $1s^{-1}$ channel show this is the primary source of the intensity, and that the angular distribution of this channel is perturbed at this energy.

Atop the shape resonance at 419 eV there is some finer structure from the satellite states. Previous PES at 1483 eV incident light energy[8] has found two relatively intense structures at 419.8 and 426.7 eV. These are currently assigned to the configuration $1s^{-1}\pi^{-1}\pi^*, {}^2\Sigma^+$, with the difference in energy from intermediate coupling between the unpaired π and π^* electrons, on the basis of CI calculations.[10] The triplet-paired state has lower energy. Whereas at the sudden limit these satellites are relatively well understood,[11] their energy dependence near their ionization thresholds is not well characterized[12,13]. Even at the sudden limit the width of the satellites peaks is too great for one electronic state,[8] including vibrational broadening.

Figure 2.2 shows the ZKE-PES spectra of N_2 across the nitrogen K-edge, with the absorption spectra.[6] This ZKE spectrum was obtained at Bell Laboratories' high resolution soft X-ray beamline located at the National Synchrotron Light Source, Brookhaven National Laboratory.[14] The experimental vacuum chamber was separated from the beamline by a thin (1200Å) Ti window. The storage ring operated in single-bunch mode. The electron detector was oriented at 90° to the polarization vector of the synchrotron radiation. The total instrumental resolution was ~200 meV for N_2 and~140 meV for CO.

The ZKE and absorption spectra are quite similar below the ionization threshold. At these photon energies core-excited states generally decay via an Auger-like, autoionization as was mentioned in Chapter 1. Since the core-excitation energy is far above the energy required for double ionization (42.68 eV for N_2), it is possible for these states to decay by emitting two electrons simultaneously. Previous work[15] on atomic systems has suggested that the kinetic energy distribution of two simultaneously emitted electrons is double-peaked with one electron having low kinetic energy and the other having correspondingly high kinetic energy. Therefore, ZKE-PES is very sensitive to this two-electron process and all the features in a photoabsorption spectrum can be found in a ZKE spectrum for a core level. The relative intensities for these transitions, however, are different in ZKE-PES and absorption.[16] In general, as the electron is excited to higher-lying orbitals the tendency to decay by emitting two electrons simultaneously increases. However, within a single electronic state the relative intensities of the different vibrational levels appear to be the same in ZKE-PES and absorption, as is expected in the Born-Oppenheimer approximation.

The 1s ionization threshold (mainline) appears in the ZKE spectra as an intense peak with vibrational structure. At higher photon energies, the structure corresponding to two-electron transitions in the neutral is present in the ZKE spectrum, but these peaks

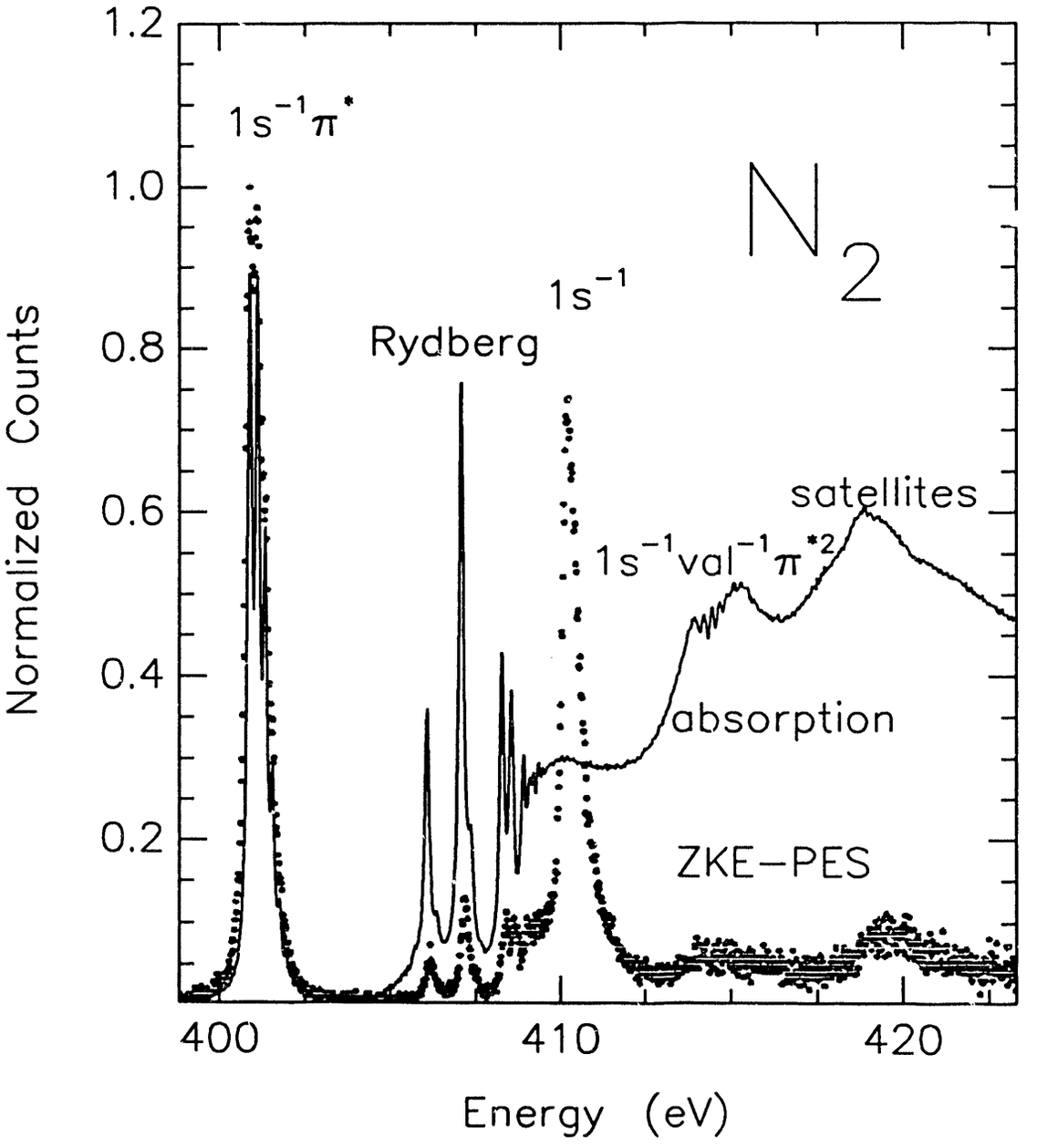

FIGURE 2.2 ZKE spectrum of N_2 across the N- K edge (data points) and the corresponding absorption spectrum[6] (solid lines). At photon energies above $1s \rightarrow \pi^*$ resonance, the absorption spectrum has been enlarged 10 times, The double excitation and satellite region of the ZKE spectrum of has been enlarged 3 times.

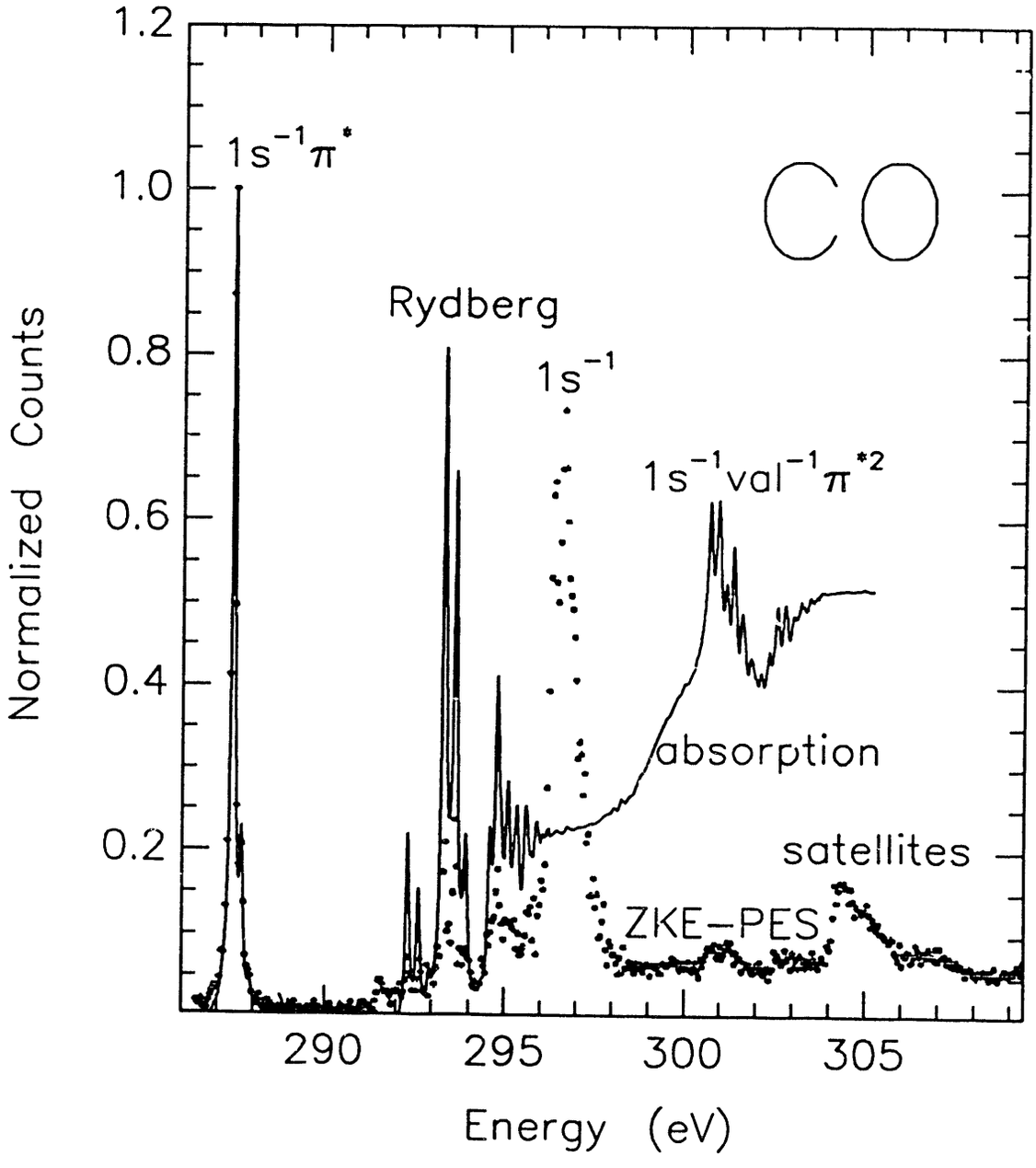

FIGURE 2.3 ZKE spectrum of CO across the C-K edge (data points) and the corresponding absorption spectrum[6] (solid lines). At photon energies above $1s \rightarrow \pi^*$ resonance, the absorption spectrum has been enlarged 9 times, and the ZKE spectrum of CO has been enlarged 3 times. The double excitation and satellite region of the ZKE spectrum of has been enlarged an additional 2.3 times.

are better resolved in the photoabsorption spectra. They can be considered Rydberg states leading to the excited states of the ion (satellites). As with the mainline state these satellites appear as peaks in the ZKE spectra and steps in the absorption spectra. Figure 2.3 shows the ZKE spectrum of CO across the C-1s ionization threshold with the absorption spectrum.[7] Because these two molecules are isoelectronic and the final states for these spectral regions are the same in the equivalent core model, the preceding discussion applies to the CO spectrum also.

Mainlines

Figure 2.4 shows the mainline peak of CO and its vibrational structure. The solid line is a least squares fit to the data, and the dashed lines show the individual vibrational peaks. As was mentioned in Chapter 1, peaks which correspond to a core-level ionization threshold exhibit Post-Collision Interaction (PCI), which broadens the peaks asymmetrically and shifts the maxima to higher photon energy. This is caused by the interaction of the photoelectron with the Auger electron. The energy values reported in table 2.3 and indicated on fig. 2.4 are the thresholds for the different vibrational states. The function of Niehaus[17], convoluted with a Gaussian for instrumental broadening, was used to fit the peaks. At threshold the difference between the Niehaus treatment and the more detailed treatment of Russek and Menlhorn[18] is less than the experimental uncertainty. The Niehaus function depends upon the lifetime of the core hole and the excess photon energy above the ionization threshold. For CO the C-1s natural linewidth was determined from the lineshape to be 95 ± 5 meV. Figure 2.5 contains the mainline spectrum of N_2, which has a natural linewidth of 140 ± 20 meV. However, the convergence of the natural linewidth, the vibrational spacing, and the instrumental linewidth is not strong for overlapping Niehaus functions. The peak positions and

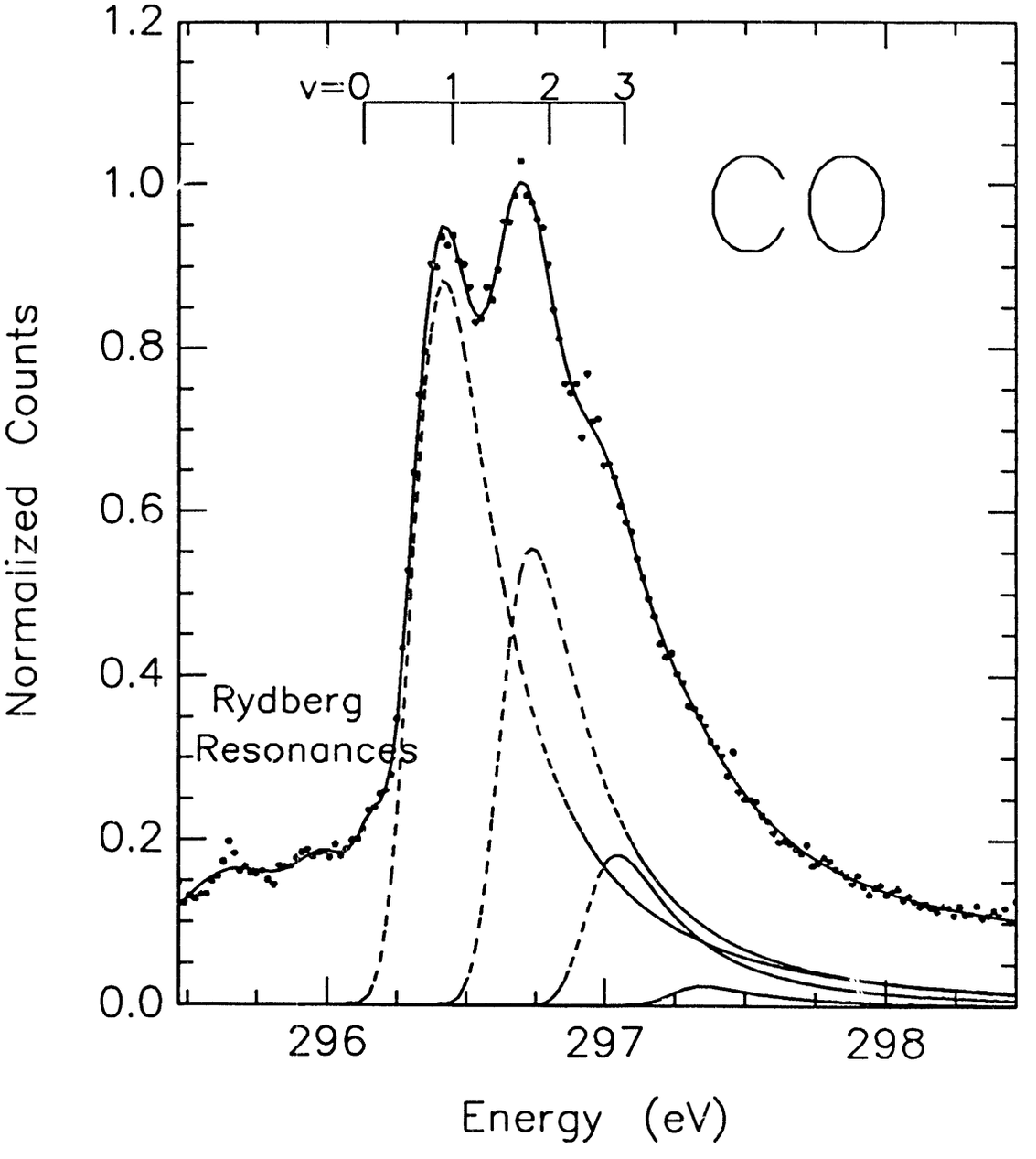

FIGURE 2.4 ZKE spectrum of CO at the C-1s ionization threshold. The solid lines are fits to the data points. The individual peaks are shown with the dashed lines. The vertical lines at the top mark the thresholds for the different vibrational states. The maxima of the peaks are shifted from this by PCI.

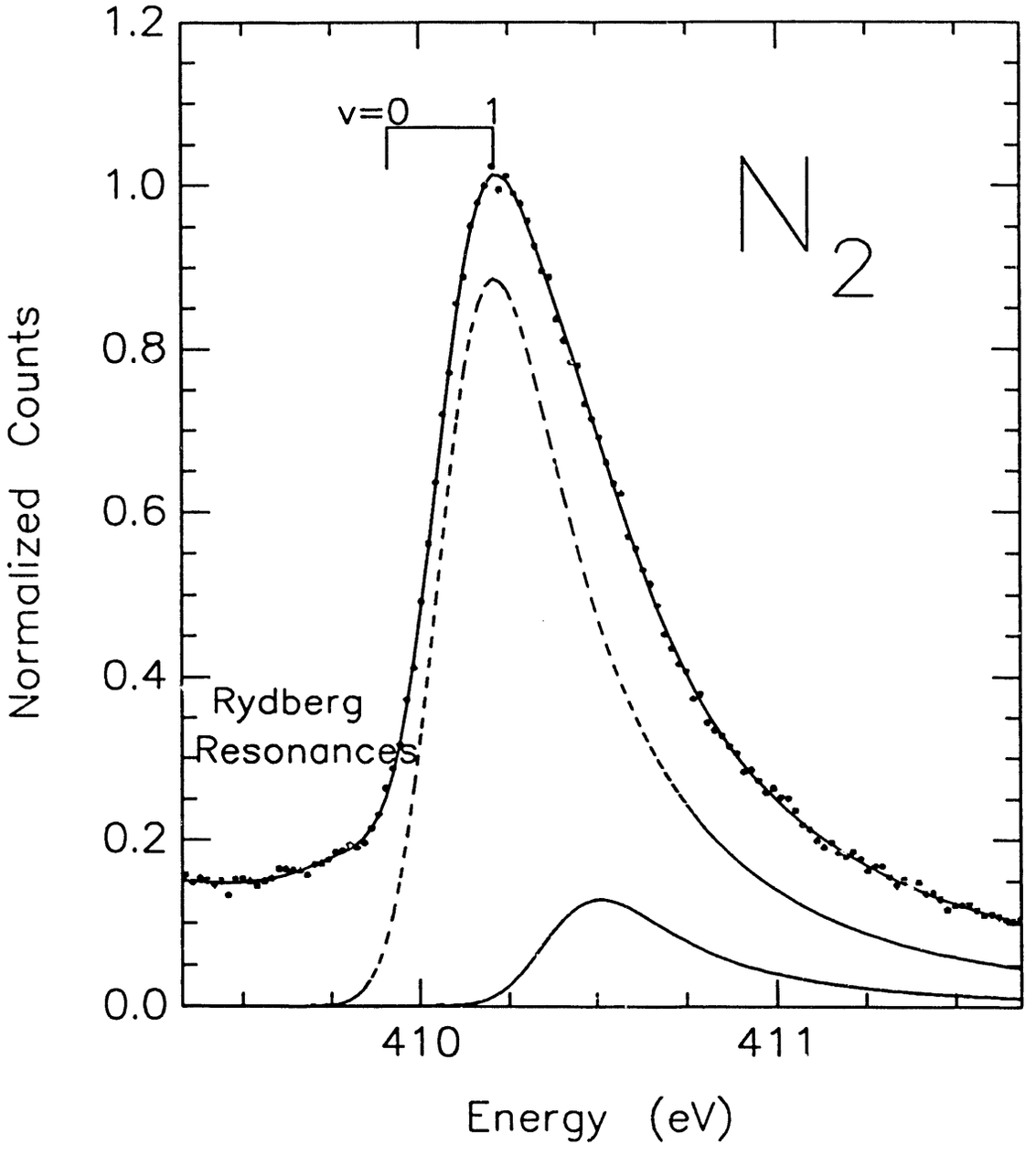

FIGURE 2.5 ZKE spectrum of N_2 at the N-1s ionization threshold: The solid line is a fit to the data points. The individual peaks are shown with the dashed lines. The vertical lines at the top mark the thresholds for the different vibrational states. The maxima of the peaks are shifted from this by PCI.

Franck-Condon factors determined from the spectra are presented in table 2.3. Also in table 2.3 are the harmonic vibrational frequencies, ω_e, obtained from the spectrum and the equilibrium bond lengths, R_e, determined by calculating the harmonic oscillator Franck-Condon Factor's (FCF's) using the algorithm of Nichols[19]. Gelius[8] previously

	Transition	Energy	FCF	
CO^{+a}	$1s^{-1}$ v=0	296.13 ± 0.03	1.00 ± 0.14	$\omega_e = 2490 \pm 140$ cm^{-1}
	v=1	296.45 ± 0.03	0.63 ± 0.06	$R_e = 1.077 \pm 0.005$ Å
	v=2	296.80 ± 0.03	0.21 ± 0.03	
	v=3	297.07 ± 0.03	0.03 ± 0.02	
N_2^{+a}	$1s^{-1}$ v=0	409.91 ± 0.03	1.00 ± 0.23	$\omega_e = 2400 \pm 600$ cm^{-1}
	v=1	410.21 ± 0.06	0.14 ± 0.05	$R_e = 1.077 \pm 0.010$ Å
CO^b	ground state			$\omega_e = 2168.1358$ cm^{-1}
				$\chi_e\omega_e = 13.2883$ cm^{-1}
				$R_e = 1.128323$ Å
N_2^b	ground state			$\omega_e = 2358.57$ cm^{-1}
				$\chi_e\omega_e = 14.324$ cm^{-1}
				$R_e = 1.09768$ Å
NO^{+b}	$X\ ^1\Sigma^+$			$\omega_e = 2379.18$ cm^{-1}
				$\chi_e\omega_e = 16.262$ cm^{-1}
				$R_e = 1.063$ Å

Table 2.3 Mainlines

a. This work.

b. K. P. Huber and G. Herzberg, *Molecular Spectra and Molecular Structure* (Van Nostrand, Princeton, 1979), Vol 4, and references therein.

analyzed the vibrationally broadened lineshapes from photoelectron spectra excited by Al Kα radiation. His FCF's for the CO C-1s mainline are 1.00, 0.97, 0.53 and 0.17, and for the N_2 N-1s mainline they are 1.00 and 0.32. He used a Gaussian lineshape and a separation of 2340 cm^{-1} versus the 2490 ± 140 cm^{-1} we determined for CO and 2400

$\pm$ 600 cm^{-1} for N_2. Both the neglect of the natural Lorentzian linewidth and the smaller vibrational separation in the least-squares fit decrease the intensity of the first peak relative to the excited vibrational states, and this may explain why the higher vibrational states appear to be more intense for Gelius. Therefore, the differences between our FCFs and his are probably due to differences of analysis and not from any real differences in the Franck-Condon factors.

The structural parameters for the equivalent-core species for both N_2 and CO, the NO^+ X state, are also listed in table 2.3 . In the equivalent-core model, the core-ionized states have the same potential and therefore the same force constant as the NO^+ X state. The vibrational frequencies should equal that of the NO^+ X state times the square root of the ratio of the reduced masses:

$$\omega_{CO^+} = (\omega_{NO^+}) \frac{\sqrt{\mu_{NO}}}{\sqrt{\mu_{CO}}} = 2480 \text{ cm}^{-1}$$

$$\omega_{N2^+} = (\omega_{NO^+}) \frac{\sqrt{\mu_{NO}}}{\sqrt{\mu_{N2}}} = 2390 \text{ cm}^{-1}$$

Here we have used the harmonic oscillator vibrational frequency for NO^+ for a direct comparison. These values are very close to those determined from the spectra, considering the errors. Because the 1s electron is non-bonding and the bond order does not change, the equilibrium bond length is assumed to decrease in the transition to the core ionized state in both molecules. This probably results from valence electrons contracting around the core hole .

Satellites

The core-level satellites of CO and N_2 were studied previously at high incident photon energy[8] and as functions of photon energy.[13] The earlier work focussed on the

sudden limit satellites, those with the same symmetry as the mainline, $^2\Sigma^+$. Recent ZKE spectra at lower resolution[16] suggested that more than one electronic state was present at low photon energy, and Angonoa et. al. [20] calculated states of other symmetries using a Green's function technique. High resolution (ZKE) spectra of the energy region of the first, $^2\Sigma^+$ satellite for CO is presented in fig. 2.6. The relative positions of the states calculated by Angonoa et. al. are also indicated. The calculated peak energies have been adjusted to the experimental scale by setting the calculated energies of the lowest binding energy $^2\Sigma^+$ states of N_2 and CO equal to the experimental values of Gelius. Clearly there is a peak lower in energy than the lowest energy $^2\Sigma^+$ state of Gelius, remembering that the energy of PCI broadened peaks is determined from the onset and not the peak maximum. Therefore the increase of intensity previously attributed solely to the $^2\Sigma^+$ peak near its threshold[12] is partially the result of other electronic states. In the Al Kα spectra there was no evidence for states other than $^2\Sigma^+$ in either N_2 or CO. Figures 2.7 and 2.8 show the ZKE spectra of the first two $^2\Sigma^+$ N_2 satellites. Even though the resolution at the N-1s edge is not as high as the C-1s edge, there appears to be structure in the spectra, which cannot be attributed to $^2\Sigma^+$ states.

Core-level satellite states should possess vibrational structure similar to the mainline peaks. Such structure has been reported for the two-electron excited states, which are the Rydberg series for the satellites of CO.[2] A Franck-Condon analysis of the lowest binding energy satellite state for CO^+, the three lowest binding energy peaks of fig. 2.6, is reported in table 2.4. The uncertainty in the relative intensities of the other fitted peaks made it impossible to perform a Franck-Condon analysis for any other state of CO^+ or N_2^+. The equilibrium bond length for this satellite should be larger than in the ground state. Promoting a bonding electron into an antibonding orbital increases the bond length more than the contraction of electrons around the core hole decreases it. The bond lengths and vibrational frequencies of the two lowest binding energy electronic

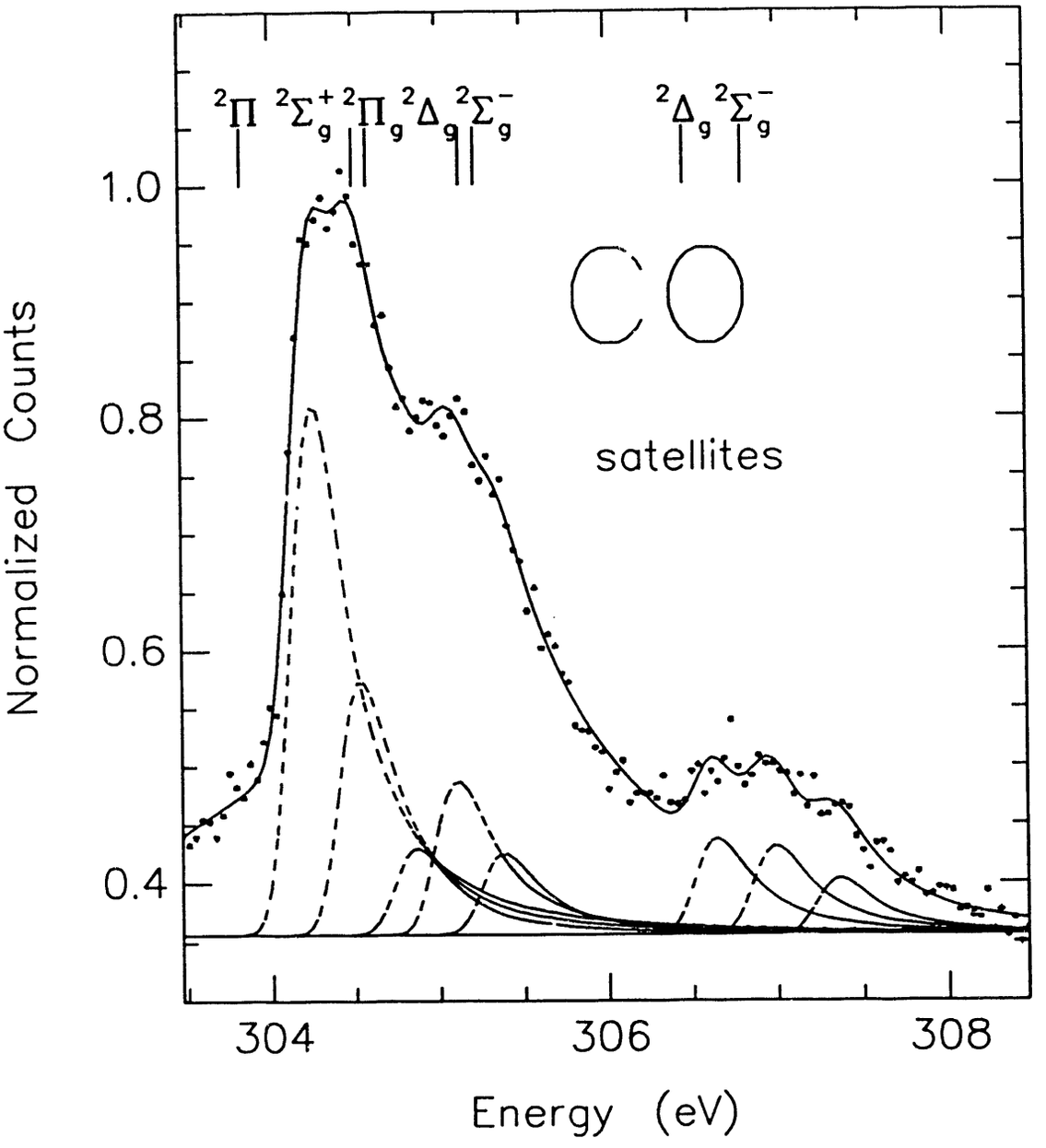

FIGURE 2.6 ZKE spectrum of the satellite region of CO: The solid line is a fit to the data points. The individual peaks are shown with the dashed lines. The calculated energies of Angonoa et. al.[11] are shown at the top of spectrum. These energies are calibrated to the experimental high incident photon energy results of Gelius.[8] As in figure 2.4, these energies correspond to the peak thresholds not the maxima, because of PCI.

states of NO^+ are also listed in table 2.4. One is a $^3\Pi$, and the other is a $^3\Sigma$ state. The bond length and vibrational frequency of the satellite are closer to those of the $^3\Pi$ state of NO^+, which results from excitation of a 5σ electron to the π^* orbital. This is the same valence-electron configuration as the lowest binding energy $^2\Pi$ state calculated by Angonoa et. al. The $^3\Sigma^+$ excited state of NO^+ has a much longer bond and much smaller vibrational frequency. Therefore the equivalent-core model supports the assignment of this lowest binding energy satellite as the $^2\Pi$ state. In N_2 the intensity at

	Transition	Energy	FCF	
CO^{+a}	$1s^{-1}5s^{-1}\pi^*$ v=0	304.02 ± 0.05	1.00 ± 0.22	$\omega_e = 2200 \pm 400$ cm^{-1}
	v=1	304.29 ± 0.03	0.47 ± 0.10	$R_e = 1.174 \pm 0.013$ Å
	v=2	304.64 ± 0.04	0.16 ± 0.09	
	(5s and π^* singlet paired)			
NO^{+b}	a $^3\Sigma^+$			$\omega_e = 1293$ cm^{-1}
				$\chi_e\omega_e = 15$ cm^{-1}
				$R_e = 1.284$ Å
NO^{+b}	b $^3\Pi$			$\omega_e = 1710.8$ cm^{-1}
				$\chi_e\omega_e = 14.0$ cm^{-1}
				$R_e = 1.175$ Å

Table 2.4 Satellites

a. This work.

b. K. P. Huber and G. Herzberg, *Molecular Spectra and Molecular Structure* (van Nostrand, Princeton, 1979) Vol 4, and references therein.

energies lower than the binding energy of the first $^2\Sigma^+$ is probably also from the $^2\Pi$ state. However, since the ground-state bond length is shorter for N_2 than for CO, the expected Frank-Condon envelope for the satellite states are broader, and we could not separate the electronic states.

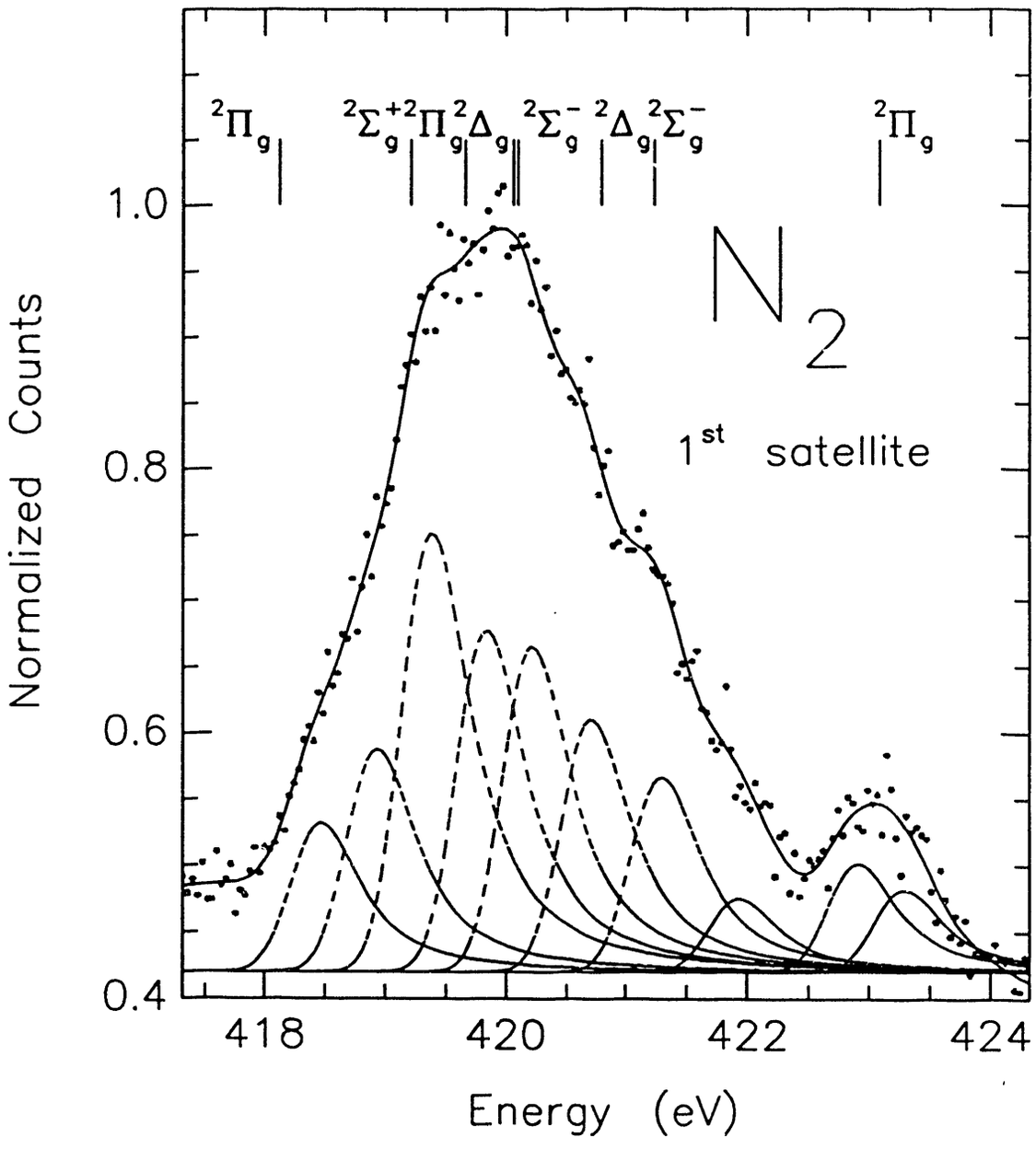

FIGURE 2.7 ZKE spectrum of the first satellite region N_2: The solid line is a fit to the data points. The individual peaks are shown with the dashed lines. The calculated energies of Angonoa et. al.[11] are shown at the top of spectrum. These energies are calibrated to the experimental high incident photon energy results of Gelius.[8] As in figure 2.4, these energies correspond to the peak thresholds not the maxima, because of PCI.

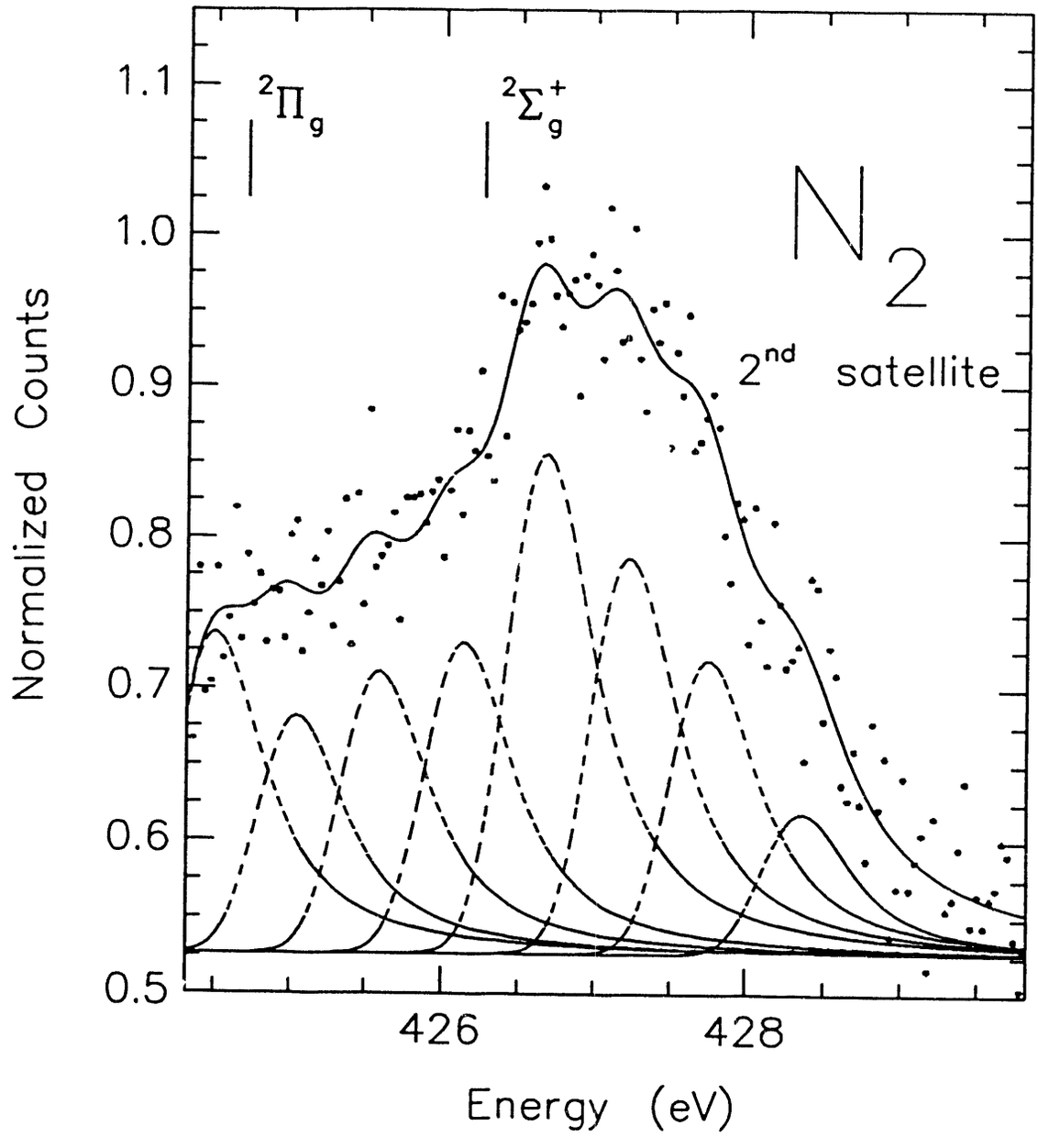

FIGURE 2.8 ZKE spectrum of the second satellite region N_2,.The solid line is a fit to the data points. The individual peaks are shown with the dashed lines. The calculated energies of Angonoa et. al.[11] are shown at the top of spectrum. These energies are calibrated to the experimental high incident photon energy results of Gelius.[8] As in figure 2.4, these energies correspond to the peak thresholds not the maxima, because of PCI

The appearance of satellites of different symmetry (especially high angular momentum states) than the mainline at their thresholds was well documented in atomic systems in Chapter 1, where it was attributed to Wannier's description[21] of double ionization, in which the two departing electrons are highly correlated at low kinetic energy, and excitation into orbitals of high angular momentum is favored. Another possible influence on the intensities of the satellites in this energy range is the σ^* resonance. Since this resonance is nearly degenerate in energy with the triplet paired satellites' threshold, it is possible they are enhanced on resonance as is the case with a satellite of SF_6.[22] However, the angular distributions of the enhanced satellite and the mainline are the same for SF_6 in the vacinity of the shape resonance, implying that they have the same symmetry, and this is clearly not true for this system. A detailed anaylsis of the double excitation region of CO by Domke et. al.[7], reveals three main series of peaks, which have an energy separation similar to the three groups of peaks in fig. 2.6. Therefore like the Ar 3s satellites, the double excitation spectrum shows the same pattern as the satellites of $N_2$and CO, and the enhancement of molecular satellites of symmetries different than the mainline happens at threshold for the same reasons that high angular momentum atomic satellites are enhanced at threshold.

Conclusions

In spite of post-collision interaction, it is possible to determine the spectroscopic parameters and equilibrium bond lengths for core-ionized species. These states, like the core-excited states of the neutral molecule, can be interpreted using the equivalent-core model. Even the satellites can be interpreted by invoking this model, if they are well resolved. Apparent enhancement of the lowest binding energy $^2\Sigma^+$ satellite near its

threshold in both N_2 and CO is partially caused by the onset near their thresholds of other higher angular momentum satellites.

Part II Photodissociation

Introduction

In chapter 2 the equivalent core model was shown to agree reasonably with the experimental results, in both zero-kinetic-energy and absorption spectroscopy, for both N_2 and CO, and with frozen-core calculations.[1,2] This model has also been applied to larger molecules,[3,4] if the geometry of the molecule is not too different from the equivalent-core molecule's geometry. In systems where this model is difficult to apply, such as benzene and ethylene, the vibrationally resolved absorption spectra also show evidence of core-hole localization.[5] The frequencies of the vibrational levels indicate that the symmetries of both molecules are lowered by core-level excitation, and the C-H stretching frequencies, in particular, are close to the typical N-H stretching frequency.

Assuming that a core hole is localized, in general, the dissociation of a molecule after core-excitation or ionization should reflect the localized origin of excitation. Previous results have not been conclusive on this point. For CF_3CH_3, the two C-1s^{-1} peaks are well separated in a ZKE spectrum, because of their respective chemical shifts. Excitation of the C-1s electron which originates from the CH_3 group produces quantitatively more CF_3^+ than excitation of C-1s from the CF_3 group or excitation of a F-1s electron.[6] For N_2O, it is possible to selectively excite either the terminal nitrogen

or the central nitrogen to the lowest unoccupied molecular orbital. The experimental difference in the relative ion yields between $N_T \rightarrow \pi^*$ and $N_C \rightarrow \pi^*$ is $\leq 20\%$ for all of the ions measured.[7] In the case of acetone,[8] however, localized excitation of the CO C-1s$\rightarrow\pi^*$ transition produces approximately ten times more C^+ than ionization or excitation of the methyl C-1s electron. In this case the π^* orbital is localized in the CO region, whereas in N_2O the π^* orbital extends over the entire molecule. So not only the localized nature of the core hole must be considered but also the localization of the orbital into which it is excited.

Since core-hole states generally relax by Auger processes, the dissociation takes place on the lower energy singly or doubly-ionized potential surface. Previous studies have shown that for N_2 the branching ratios and kinetic energies of the departing fragments differ when measured in coincidence with different Auger electrons.[9] Therefore this relaxation before dissociation also plays an important part in determining the details of the dissociation process.

All of these previous studies have focussed on the role of the excited electronic state in the dissociation process. The role of vibrational excitation in the core-hole excited-state has not been determined. Previous studies with vibrational resolution have been limited to EELS, absorption, and some photoelectron spectroscopy, as in chapter 2. For differential experiments, such as Auger electron or deexcitation spectroscopy and photodissociation, the incident light intensity required has limited these studies to using broad band excitation and determining the effect of interference from the manifold of vibrational states.[10,11] How a specific vibrational excitation affects dissociation remains unanswered. For a simple diatomic, such as N_2, the absorption spectra and theory indicate that the nuclear and electronic wavefunctions are separable, for the core-excited state, which implies that vibrational excitation should appear as kinetic energy of the departing fragments. Even in this simple case, however, the Auger

and deexcitation spectra show evidence of interference from the large natural line-width of the core excited states. For more complex highly symmetric molecules, such as ethylene, the core excited states experience a Jahn-Teller-like distortion from vibronic effects. Since the nuclear and electronic wavefunctions are known to be mixed, the effects of vibrational excitation are not transparent. Using the AT&T high resolution soft X-ray monochromator, it was possible to excite specific vibrational levels of core-excited states. I then studied the photodissociation products in an attempt to understand the role of vibrational excitation in this process. First N_2 was studied, because many types of experimental results exist for this molecule, and by comparison with these studies, I hoped to carefully characterize the analyzer and achieve a thorough understanding of this dissociation process. Then ethylene was studied, since vibronic effects are known to be important in its core-excitation spectrum, and CH_3Cl was studied because of its difference from the other systems.

The time-of-flight system used to study threshold electrons was adapted to the study of positive ions. The microchannel electron multipliers are also efficient ion detectors. The arrangement used is shown in Figure II.1. Because the typical delay between light pulses of a synchrotron is on the order of 100 nsec in timing mode and to obtain reasonable resolution the ions' time-of-flight should be on the order of microseconds, the light source was treated as a continuum. One method for time-of-flight detection of ions is to pulse the extraction grids. However, when a molecule absorbs an X-ray, usually it emits electrons first, then the remaining positive ion might dissociate. Therefore it is possible to use a static field time-of-flight analyzer to study the ionic fragments and their kinetic energies, by determining their TOF relative to an initial emitted electron. Figure II.1 shows a schematic diagram of the detector. Since the goal is to separate different kinetic energies of the ionic fragments, the long flight tube was used to analyze the ions, and the electron detector was designed for high collection

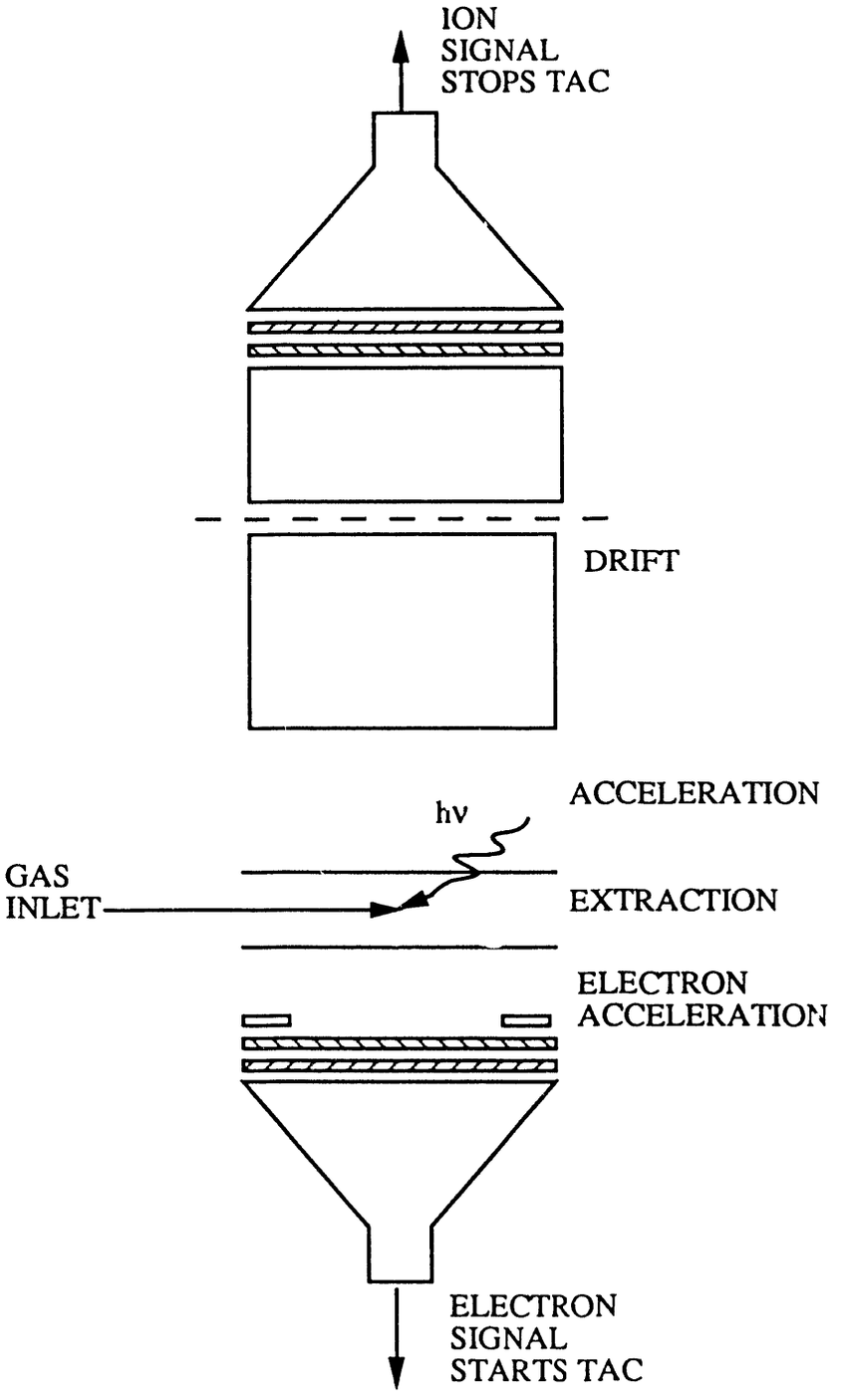

FIGURE II.1 Photoelectron, Photoion Analyzer

efficiency. The electronics were the same as for the zero-kinetic-energy spectra. The ion detector was composed of three regions: extraction, acceleration and drift, and was operated in the space focussing mode.[12] Electrons were accelerated out of the interaction region toward a bare set of channel plates in front of the same resistive anode used in the ZKE analyzer. This provided a start signal for the time-to-amplitude converter (TAC). The front of the first channel plate was kept at +157 volts, but the extraction potential was varied. The electrons' time-of-flight for all extraction fields was less 15 nsec. For the molecules studied, the TOF of the ions was between 1 and 12 μsecs. Therefore the total error introduced in the ions' TOF by using the initial electron pulse is less than 5%.

The collection efficiency as a function of the initial kinetic energy of the charged particle is determined by the active area of the microchannel plate detector and the time it takes the particle to reach the detector. Figure II.2 shows this schematically for an isotropic distribution. As the particles travel down the flight tube, they expand into a sphere of radius, $L = t(2U_0/m)^{-1/2}$, where t is their time-of-flight, U_0 is the initial kinetic energy, and m is the mass of the particle. The acceptance half angle, θ, equals $\sin^{-1}$ (L/R) where R is the radius of the active surface of the detector. The transmission is $1/2(1-\cos\theta) + 1/2(1-\cos\theta')$ where θ and θ' are indicated on figure II.2.

For the ions the calculation of the transmission was relatively straight forward. The time-of-flight at each energy was calculated for the particles emitted directly into the detector and away from the detector. Using these flight times, the forward and reverse transmissions were calculated and summed. The results are shown in figure II.3 for the potentials used in these experiments. For the electrons, the flight path is very short, and the sphere in figure II.2 expands appreciably from the time the first straight into the detector electron reaches the detector until the electrons emitted at the acceptance angle reach the detector. Therefore the simple calculation used for ions is inadequate. The

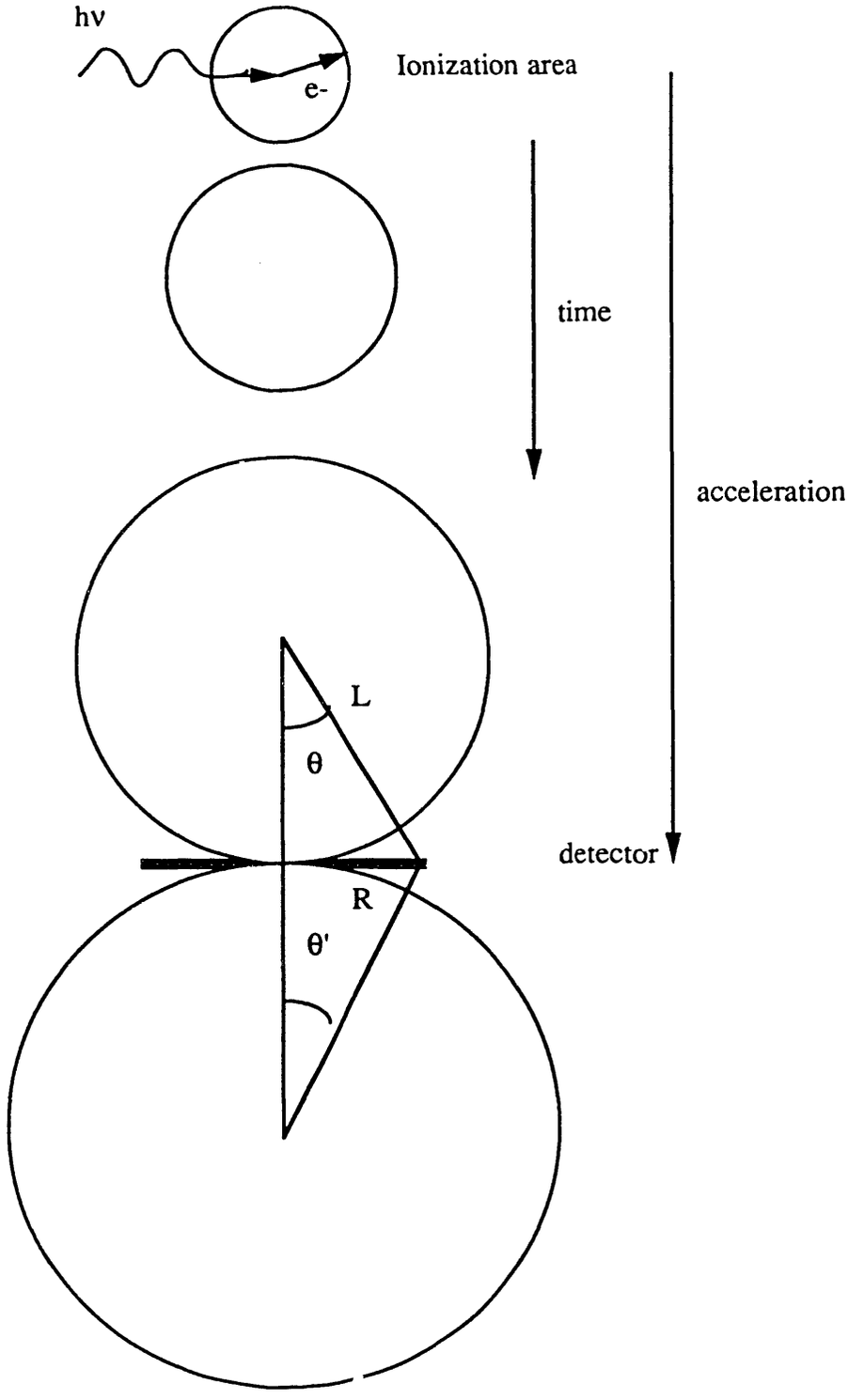

FIGURE II.2 Schematic Diagram showing the particle's spatial distribution as a function of time and position in the detector

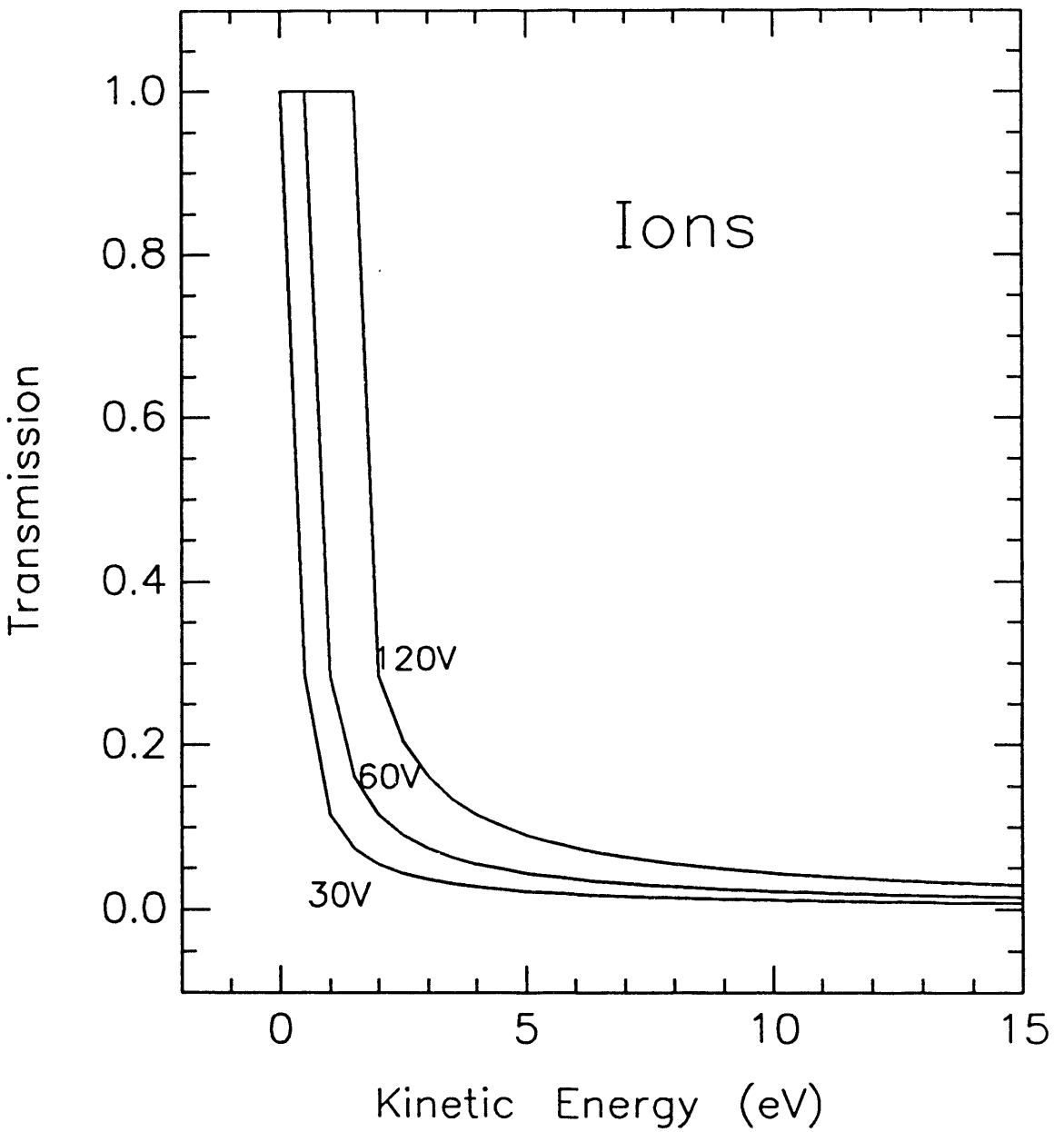

FIGURE II.3 Ion transmission as a function of initial kinetic for different extraction potentials for an isotropic distribution.

transmission was calculated with a numeric simulation program for charged particles in electric fields, MacSimion,[13] which calculates the potential in a two-dimensional array. The results for the fields used are presented in figure II.4. The irregularities in the calculated transmission are probably from the finite number of points in the potential array and the resolution in the calculated angles. All extraction potentials have approximately equal (10%) transmission for at the energies of Auger electrons, 200-350 eV. It is apparent from figure II.4 that we are measuring ions in coincidence with primarily low kinetic energy electrons, and that this is enhanced for higher extraction fields.

Because the beam from the monochromator where these experiments were performed was large (4mm) in the horizontal direction, the analyzer was placed at 90° relative to the light's polarization vector. The effects of the angular distribution on the kinetic energy profile are not straightforward. Saito and Suzuki,[14] however, have obtained good agreement with angularly resolved data, by assuming that ions of every kinetic energy have the same angular distribution. This can be justified by two arguments. The first concerns the lifetime of the core-hole excited state. Since this state relaxes in about 10 fsec, and a typical rotational period is 100 psecs, the molecule's initial alignment relative to the polarization vector does not change before it dissociates. The second argument concerns the Auger electrons. For the particular case of N_2, the angular distribution of the Auger electrons was measured and found to be essentially zero.[15] This implies that realignment does not occur during the relaxation process. It is hasty, however, to assume that electrons from a particular Auger peak are isotropically distributed. Studies on atomic systems[16] have shown that the sum of several different Auger electrons can have an isotropic distribution, while the individual peaks can have vastly different angular distributions. Because the kinetic energy of the ion can be

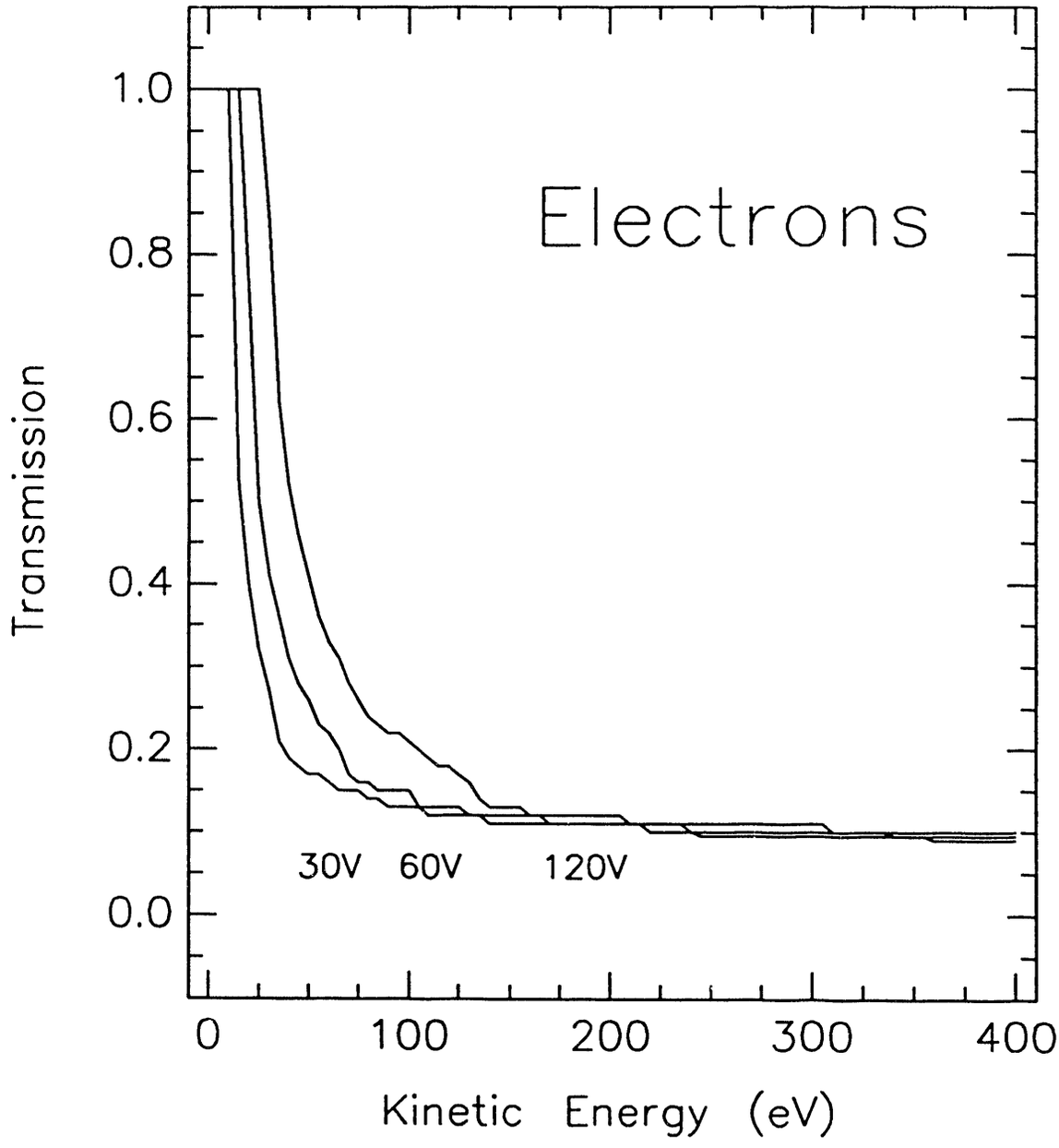

FIGURE II.4 Electron transmission as a function of initial kinetic for different extraction potentials for an isotropic distribution.

different measured in coincidence with different Auger electrons, it is not safe simply to assume that the angular distribution is the same for all kinetic energies.

The transmission presented in figure II.3 assumes an istropic distribution of ions and electrons. In general, this is not the case. Clearly if the particles are emitted at 90° relative to the polarization vector their transmission does not decrease as rapidly with increasing kinetic energy. A detailed discussion of the effects of the angular distribution will be presented in Chapter 3 in conjunction with the N 1s Rydberg states of N_2.

With this apparatus two types of data were collected, energy dependence sweeps and kinetic energy distributions. The energy dependence sweeps were determined by using a TAC window of all kinetic energies of a specific mass to charge ratio and sweeping through the interesting energy range. Sweeps of the total ion and total electron yield were used for the energy calibration. The light intensity for an energy dependence sweep was calibrated by using the electron yield from a gold grid calibrated against the total ion yield of argon. This gives the relative intensity of particular ionic fragment as a function of incident energy. The kinetic energy distributions show the energy released upon fragmentation.

The kinetic energy distribution is determined by converting a time-of-flight spectrum at a particular incident light energy to the kinetic energy scale. To do this the time-of-flight was calculated for different kinetic energies of specific mass to charge ratios. The experimental time-of-flight spectrum was put on an absolute scale by setting the flight times of the parent ion, $N_2,^+$ and the double ion, $N_2,^{+2}$ to their calculated values, since they are only thermally broadened. For N_2 there are only three mass to charge ratios present, 28, 14 , and 7, and these are well separated in the the time spectrum. If kinetic energy is released in dissociation, there are two possibilities, either all the fragments with that energy are collected or a fraction of them are collected. For the first case, the experimental peak will appear as one broadened peak centered at the

time a particle with no kinetic energy should appear. If only a fraction of the solid angle is collected, those initially directed perpendicular to the axis of the detector are not collected, so two peaks appear in the time spectrum, one for particles initially directed into the detector, and one for those directed away from the detector. These will also be centered about the zero-kinetic-energy time. Figure II.5 is a time-of-flight spectrum of N_2 with the different fragments labeled. Using the calculated values for the flight times of different kinetic energies, the spectrum can be converted to an energy scale and divided by the transmission of the fragment at that energy. This gives the intensity of the fragment as a function of its kinetic energy.

Conversely, the functional form of a particular kinetic energy can be calculated in time , and these functions used to fit the time spectrum. The resulting peak intensities can be plotted as a function of kinetic energy, similarly giving the fragment's intensity as a function of its kinetic energy. This technique was used by Suzuki and Saito.[14] A comparison of these two methods is presented in figure II.6. The points represent the least square fit to the time spectrum and the line is a point by point time to energy conversion. Both methods account for the transmission as a function of kinetic energy. They are normalized to each other at the maximum intensity. As can be seen in figure II.5, the two methods are in agreement. The fitting procedure, however, does not extend to very high kinetic energies, and also can add an arbitrary oscillation to the kinetic energy distribution. Therefore the direct time to energy conversion will be presented.

The energy dependence data provides a general pictorial representation of how the initial excited electronic state affects the dissociation products. For C_2H_4 very little is known about the high-lying doubly ionized dissociative states, this gives some new information. For N_2 the kinetic energy distributions are used to assign some of the high kinetic energy fragments and to examine the role of vibrational excitation in the core-excited states.

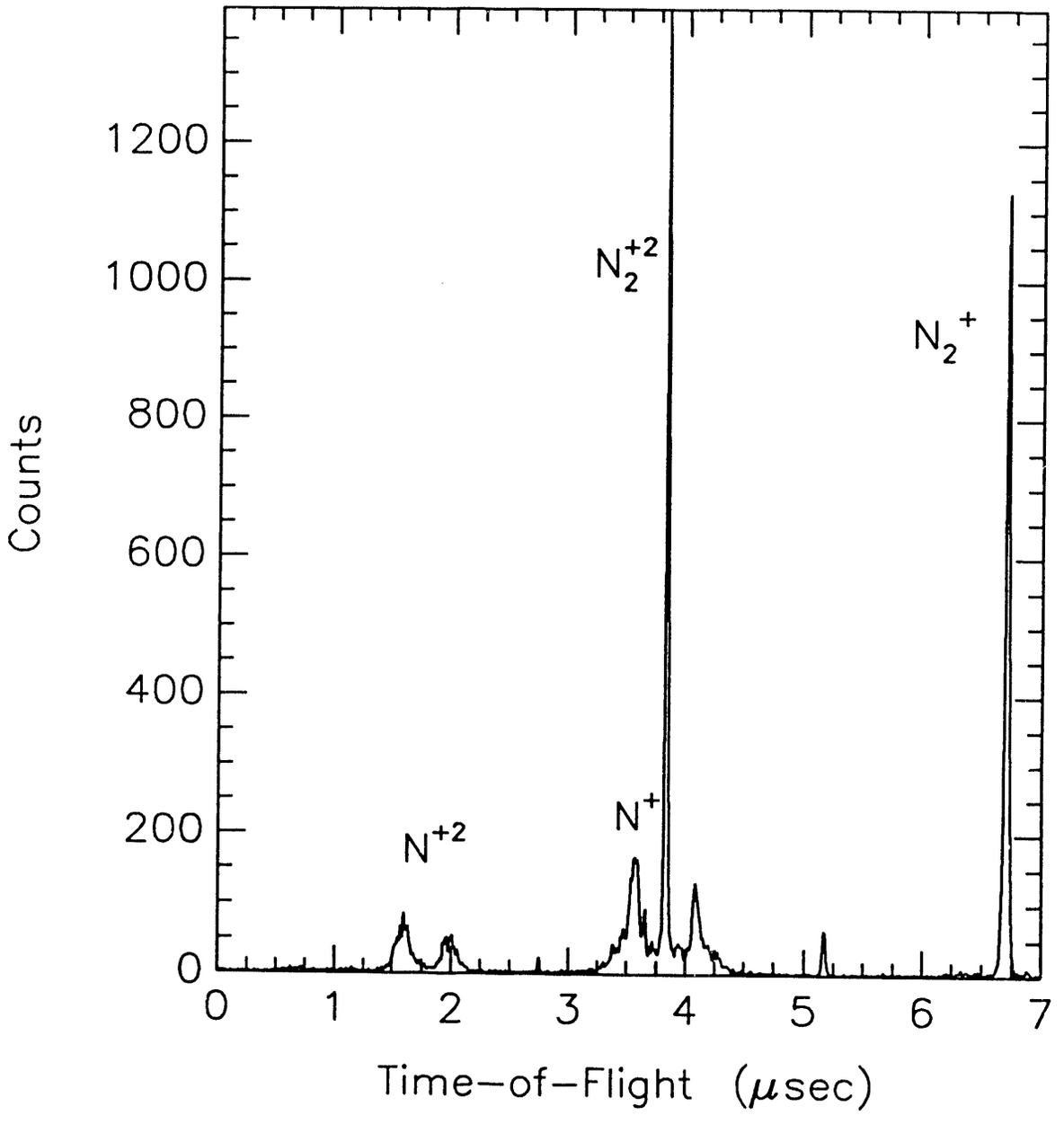

FIGURE II.5 Time-of-flight spectrum at N_2 at 380 eV incident light energy and 70 V extraction potential.

Chapter 3 Photodissociation of N_2

After a molecules interacts with an X-ray several processes occur. This is shown schematically in figure 3.1. If the X-ray has more energy than the binding energy of the 1s electron, that electron is emitted as a photoelectron. The molecule is still in a highly excited state, and typically (~95%) it relaxes by Auger decay leaving the molecule with two electrons missing in the valence shells. For N_2 the Auger electrons have energies of 200-360 eV. This leaves the molecule in a doubly charged state. Depending on the nature of the potential surface, after Auger decay the molecule might dissociate. The total kinetic energy of the fragments is then equal to the difference in energy between the Franck-Condon position on the dissociative surface and the internal energy of the fragments. In this case, photoelectron spectroscopy shows the core-ionized potential surface, the Auger spectrum shows the energies of the doubly ionized potential surfaces, and the ionic fragments show whether or not these doubly ionized surfaces are dissociative and what the fragments are. If the energy of the X-rays is varied not only the core-ionized states but also the neutral core-excited states can be studied. These processes are also shown in figure 3.1. For the neutral states, Auger processes are typically divided into two categories, participant, where the excited electron changes orbitals, and spectator, which mimics the core-hole Auger spectrum

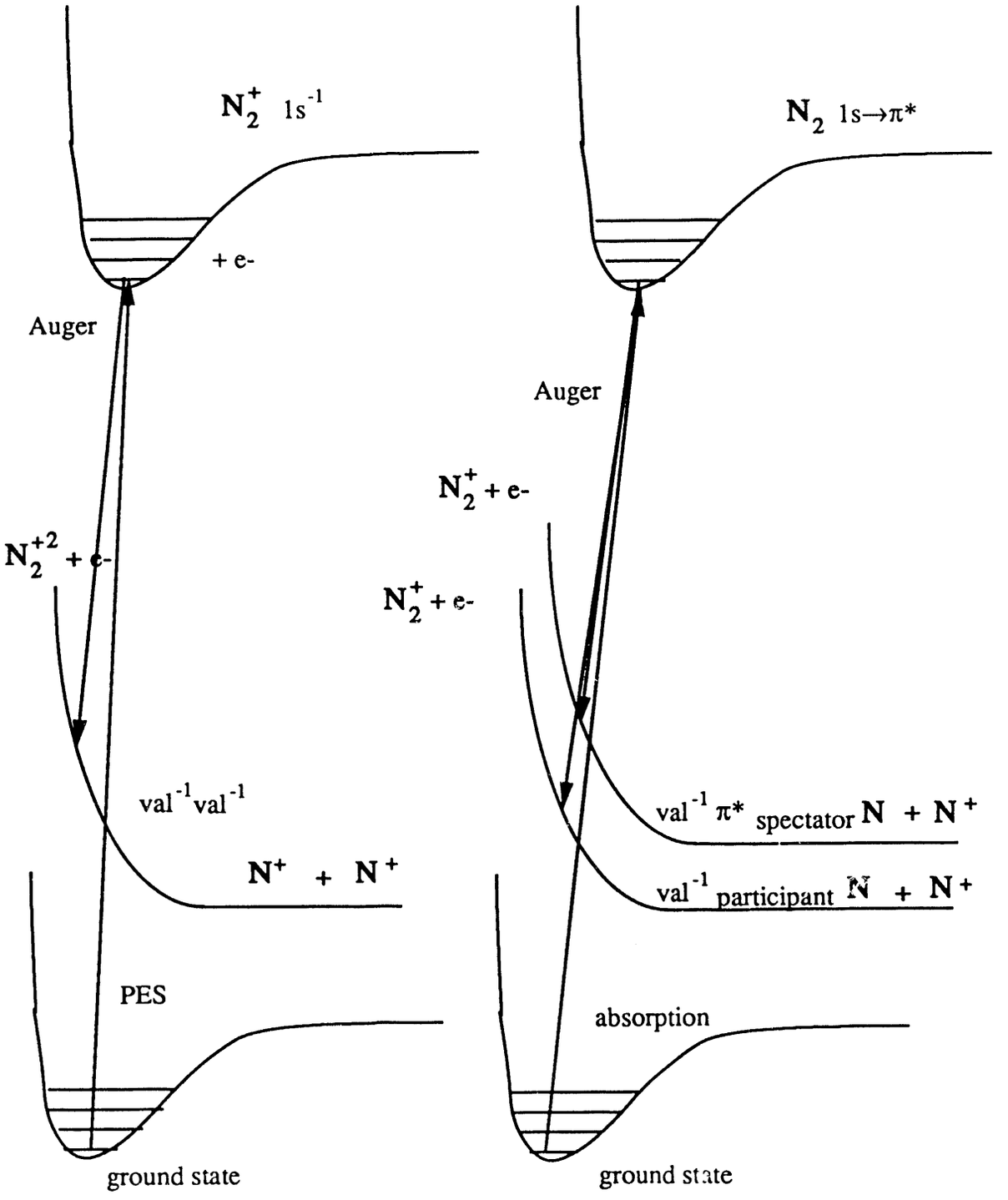

FIGURE 3.1 Schematic Diagram of processes following core-level absorption

shifted to higher kinetic energy by the energy difference between the doubly ionized final state and the final state with only one electron ionized and the other electron left in an excited orbital. Both of these processes leave the molecule in the singly charged state and correspond to the states of the ion determined by UPS. Aside from these dominant processes, double Auger decay can happen from either the core-excited or core-ionized state. In this instance two electrons are emitted in the relaxation of the core-hole state, and therefore the charge of the dissociative state is increased by one. Since the two electrons are emitted simultaneously, they share the energy and do not correspond to a peak in the Auger spectrum but to the background.

Previous studies of core-excited or ionized N_2 have focussed on the differences in the relaxation and dissociation for the different initial electronic excitations. Moddeman et. al.[1] carefully compared the Auger spectrum produced by electron impact with that produced by nonresonant monochromatized X-rays. Electron impact produces core-ionized states and core-excited neutral states whereas the X-rays produce only the core-ionized state. In this way, Auger peaks from the $1s \rightarrow \pi^*$ transition, which are present only in the electron impact spectrum, were distinguished from those which originated from the $1s^{-1}$ initial state, which are present in both. Much effort has been used to compare the Auger transitions of N_2 with calculated states of N_2^{2+}. There has been some disagreement[2-4] in the past over the energy ordering of the lowest calculated orbitals of N_2^{2+}. The lowest energy state is either $^1\Sigma_g^+(3\sigma^{-2})$ or $^3\Pi_u$ $(3\sigma_g^{-1}1\pi_u^{-1})$. Whichever state is lowest, it is approximately 4 eV higher in energy than the lowest N_2^{2+} dissociation channel of N^+ (^3P) + N^+ (^3P), 38 eV. Table 3.1 gives a composite energy level diagram of N_2, its ionic and dissociative states. The assignments of the N_2^{2+} states are based upon a comparison of the experimental energies of Moddeman et. al. with the calculations of Liegener. As table 3.1 indicates, there are many ways the core-excited molecule can relax. It is obvious from the energy levels that a neutral

N_2^+		N_2^{+2}		Dissociative States	
Assignment[a]	Energy[a]	Assignment[b]	Energy[c]	Assignment[d]	Energy[d]
		$2\sigma_g^{-2}\,{}^1\Sigma_g^+$	94.9		
		$2\sigma_g^{-1}2\sigma_u^{-1}\,{}^1\Sigma_u^+$	77.2		
		$2\sigma_g^{-1}(3\sigma_g^{-1}/1\pi_u^{-1})$	72.5		
		$2\sigma_g^{-1}(3\sigma_g^{-1}/1\pi_u^{-1})$	70.8		
				$N^+(^3P) + N^{+2}(^2P)$	68.44
		$2\sigma_g^{-1}(3\sigma_g^{-1}/1\pi_u^{-1})$	67.5		
		$2\sigma_g^{-1}(3\sigma_g^{-1}/1\pi_u^{-1})$	62.1		
		$2\sigma_u^{-1}3\sigma_g^{-1}\,{}^1\Sigma_u^+$	59.5		
		$2\sigma_u^{-2}\,{}^1\Sigma_g^+$	57.4		
				$N(^4S) + N^{+2}(^2P)$	53.9
		$2\sigma_u^{-1}\,3\sigma_g^{-1}\,{}^1\Sigma_u^+$	53.0		
		$2\sigma_u^{-1}\,3\sigma_g^{-1}/1\pi_u^{-1}$	51.2		
		$2\sigma_u^{-1}1\pi_u^{-1}\,{}^1\Pi_g$	49.7		
$2\sigma_g^{-1}\,\pi^*$	49.1[e]				
		$1\pi_u^{-2}\,{}^1\Delta_g$	47.4		
$2\sigma_g^{-1}\,\pi^*$	47.1[e]				
		$3\sigma_g^{-1}1\pi_u^{-1}\,{}^1\Pi_u$	46.4		
$2\sigma_g^{-1}\,\pi^*$	45.1[e]				
		$2\sigma_u^{-1}3\sigma_g^{-1}\,{}^3\Sigma_u^+$	44.9		
		$3\sigma_g^{-1}1\pi_u^{-1}\,{}^3\Pi_u$	43.4		
		$3\sigma_g^{-2}\,{}^1\Sigma_g^+$	42.9		
$2\sigma_g^{-1}\,{}^2\Sigma_g^+$	39.75				
				$N^+(^3P) + N^+(^3P)$	38.83
π^*val^{-1}	32.0[e]				
π^*val^{-1}	26.0[e]				
π^*val^{-1}	25.0[e]				
				$N(^4S) + N^+(^3P)$	24.29
$^2\Sigma_u^+$	23.59				
$^2\Pi_g$	22.07				
$^2\Pi_g$	21.68				
$^2\Sigma_u^+$	18.38				
$2\Pi_u$	16.72				
$^2\Sigma_g^+$	15.58				

Table 3.1 N_2 Ionic States

a. G. Hertzberg Ref. 5.
b. C. M. Liegener, Ref. 2.
c. Moddeman et. al. Ref. 1.
d. C. E. Moore, Ref. 6.
e. Eberhardt et. al. Ref. 7.

excited state which relaxes by participant Auger decay, leaving one valence electron absent, cannot dissociate. However, the inner valence, $2\sigma^{-1}$ orbital, 39.75 eV, lies above the $N^+(^3P) + N^+(^3P)$ dissociation limit as do the $e^{-2}\pi^*$ spectator states, and many N_2^{+2} states are dissociative.

The first measurement of the dissociation of core-ionized N_2 compared the ionic fragments produced by 930 eV X-rays with those from 280 eV X-rays.[8] At 280 eV, the major product was N_2^+ (73 ± 2 %), and N^+ (26 ± 1 %) appeared with only 0.7 eV kinetic energy. At 930 eV, N^+ was the major product (75 ± 8 %) and the average kinetic energy was 6.7 eV. A significant amount of N^{+2} was also present (16 ± 2 %) with a kinetic energy of 17 eV. Some singly ionized N_2^+ was also present (7.5 %). About 5% of the core-ionized molecules relax by fluorescence versus Auger decay, and this plus direct valence excitation can account for the singly ionized molecules. Carlson and Krause explained this by viewing the dissociation as a "Coulomb explosion" and did not discuss the phenomena in terms of potential surfaces. However, Eberhardt et. al.[9] associated an Auger electron of a specific energy with a potential surface for N_2^{+2}. By measuring the ionic fragments produced by quasi monochromatic undulator radiation of 1200 eV with different Auger electrons, they were able to map out some of the low lying potential energy surfaces of N_2^{+2}.

They found that branching ratios and kinetic energies of the departing fragments were highly dependent upon the kinetic energy of the coincident electron. Their results are summarized in table 3.2. The general trend is lower kinetic energy of the Auger electron yields higher kinetic energy of the ionic fragments, which implies that many of the N_2^{+2} states populated by Auger decay dissociate to the ground states of the ionic fragments. Saito and Suzuki,[10] by making this assumption and the assumption that the states dissociate into the nearest energy allowed channel, have explained the kinetic energy distribution of N^+ and N^{+2} determined at 419 eV. The Auger spectrum, on the

Electron	N_2^{+2}	N^+	N^{+2}
367 eV	0.0	(4.5 eV)	
363 eV	0.0	4.45 ± 0.6 eV	
360 eV	0.0	5.5 ± 0.8 eV	
350 eV		Unresolved structure	Unresolved structure
330 eV			6.7 ± 1.0 eV
315 eV		13	13

Table 3.2 Kinetic Energies of fragments from Eberhardt et. al. ref. 9.

binding energy scale, corresponds to the energy of dissociative states. It is scaled to the kinetic energy of the ionic fragment by assuming the total kinetic energy equals the binding energy of the Auger electron minus the energy of the dissociative states. For N^+ this is:

$$(BE_{N_2^{+2}}) - E_{N^+ + N^+} = 2(KE_{N^+}).$$

In the case of N_2 this is multiplied by two because of conservation of momentum. Figure 3.2 shows their results. They also determined the kinetic energy distribution of these ions at the energies of some members the Rydberg series, and at the π^* resonance. Since the Auger spectrum of N_2 is known at the π^* resonance, Saito and Suzuki also compared this with the kinetic energy distribution of N^+, and this is shown in figure 3.3, assuming the dissociation is into the ground state of $N^+ + N$. In this case the agreement was not as good, especially at high kinetic energies. Therefore although this system has been studied previously some questions remain. The origin of Saito and Suzuki's disagreement at high kinetic energy of the ion is still not known. If the ions are a mixture of ground and excited electronic states, which is purely an analysis problem, this would add intensity to the lower kinetic energy ions. Whereas this could explain the differences in the 419 eV kinetic energy distribution, the 401 distribution has experimentally more higher kinetic energy ions. It is possible that the higher kinetic energy ions in Saito and Suzuki's spectra are the result of double Auger on the resonance and are in fact from dissociation of N_2^{+2}. Double Auger decay is known to

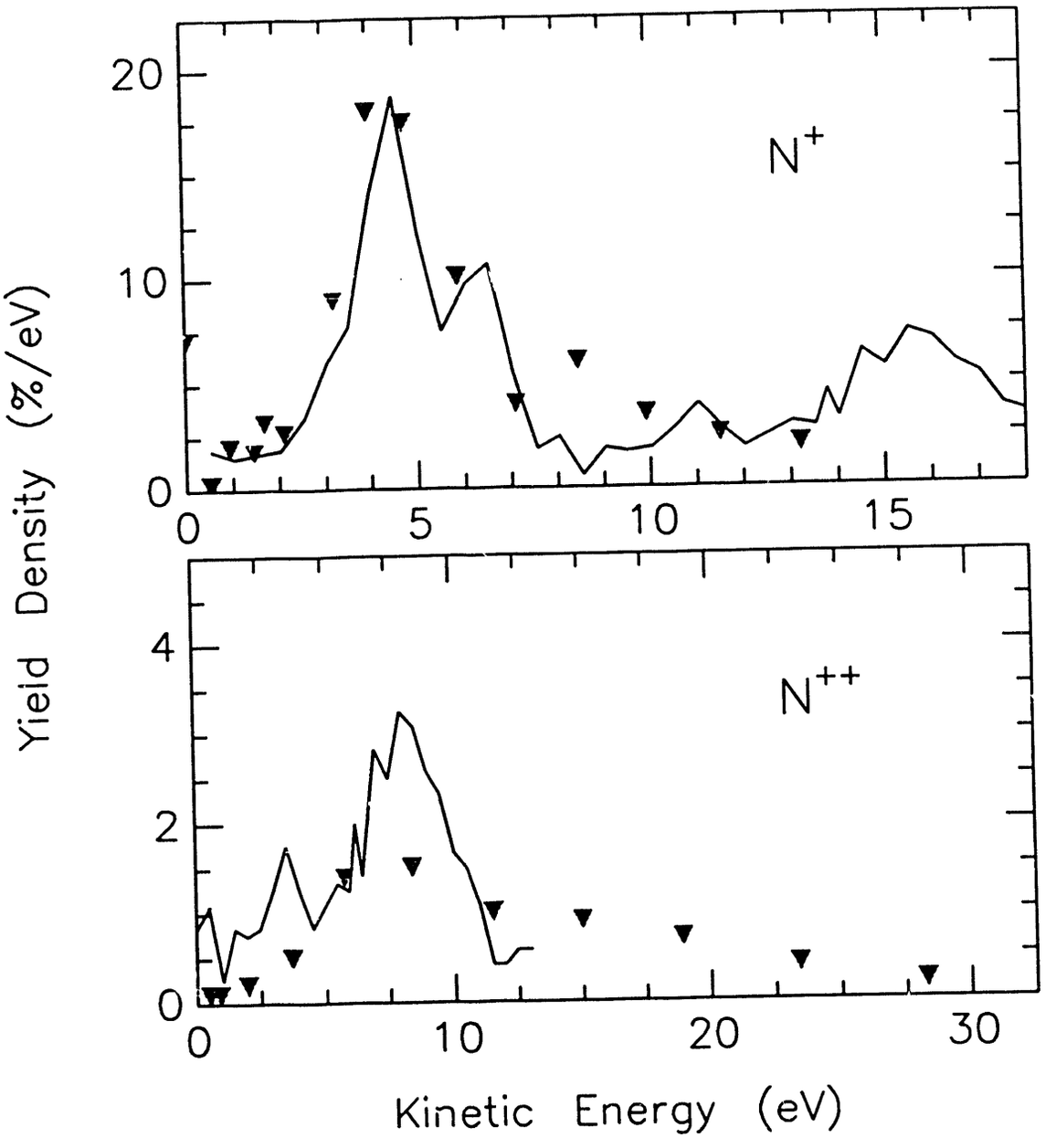

FIGURF 3.2 Experimental kinetic energy distribution of N^+ and N^{+2}, from Suzuki and Saito, Ref. 9, points, compared to the Auger spectrum of Eberhardt et. al. (ref. 7), line, at 419 eV incident light energy.

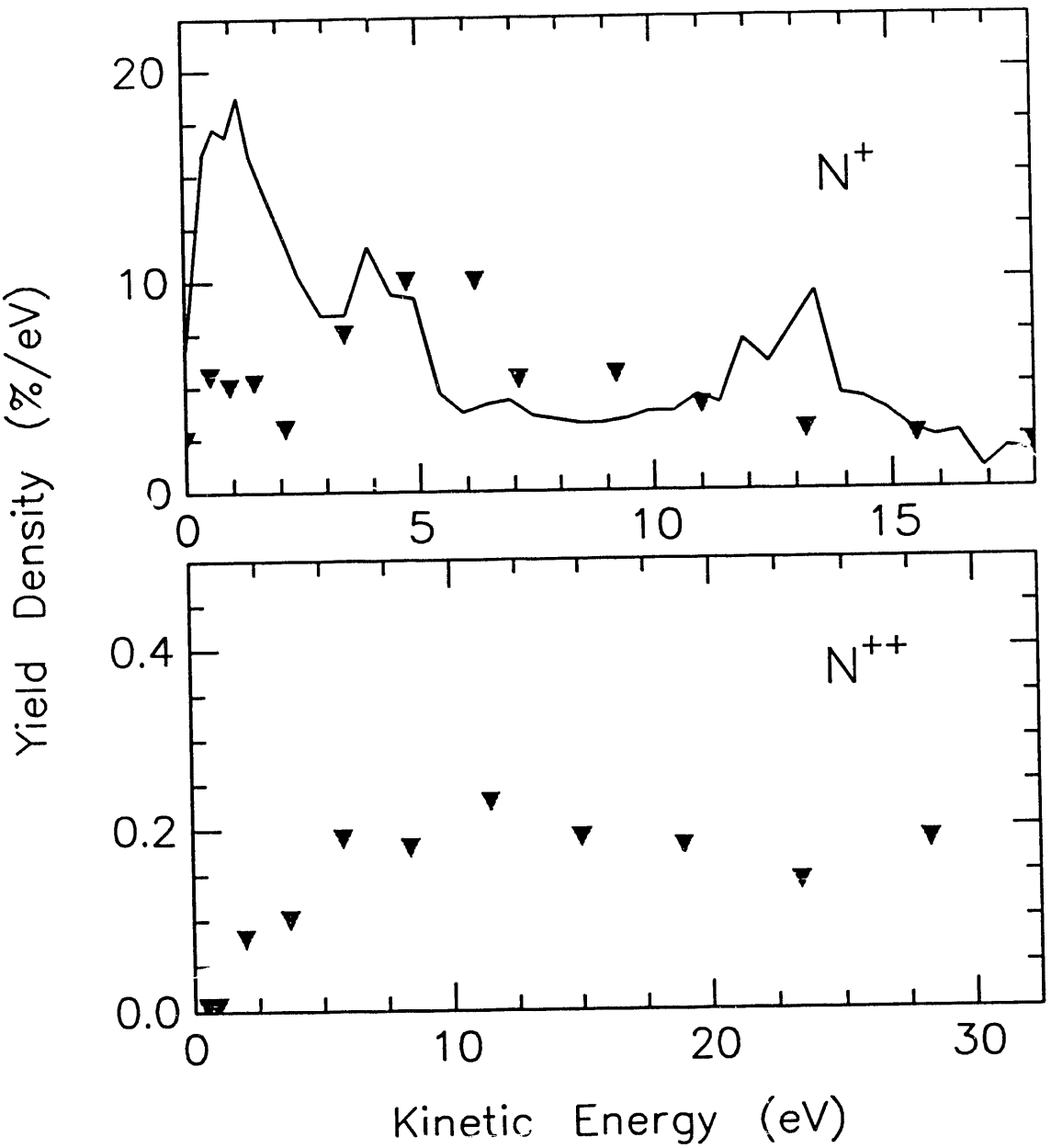

FIGURE 3.3 Experimental kinetic energy distribution of N^+ and N^{+2}, from Suzuki and Saito, Ref. 9, points, compared to the Auger spectrum of Eberhardt et. al. (ref. 7), line, at 401.1 eV incident light energy.

happen on this resonance, and even more prominently on the Rydberg resonances.[11] Saito and Suzuki[12] found the branching ratio of N^{+2} to be 11% on the π^* resonance, so at least this amount of the resonantly excited molecules relax by double Auger, or a cascade type Auger. Ions, which result from double Auger decay, cannot be directly related to the Auger spectrum, since the electrons from double Auger decay form a continuous distribution.

On resonance very low energy electrons must come from double Auger decay, so by measuring the ions in coincidence with low energy electrons, it is possible to see what in the ions' kinetic energy distributions on a resonance is from dissociation on the doubly ionized potential surfaces. In this chapter, I examine the kinetic energy distribution of N_2 ions produced at the core-excited resonances in coincidence with low energy electrons to see which doubly ionized states are important for resonant dissociation. Also, because low energy electrons can be collected with high efficiency, we were able to examine the effects of vibrational excitation on the kinetic energy distributions.

Energy Dependence

There are four prominent ionic species present in the TOF spectra. Figure 3.4 shows a spectrum of N_2 at 380 eV incident light energy with the different species indicated. Also visible is a peak at 5 μsec form O_2 contamination. N^{+3} was not observed. Since N^{+2} and N^+ have significant kinetic energies as is shown by their double peaked structure, their collection is subject to the analyzer's transmission function. N_2^+ and N_2^{+2} are collected with nearly 100% efficiency.

Sweeps of the different ionic species were collected over the entire $1s^{-1}$ region using two different analyzer settings, 30 V extraction, low field, and 120 V extraction,

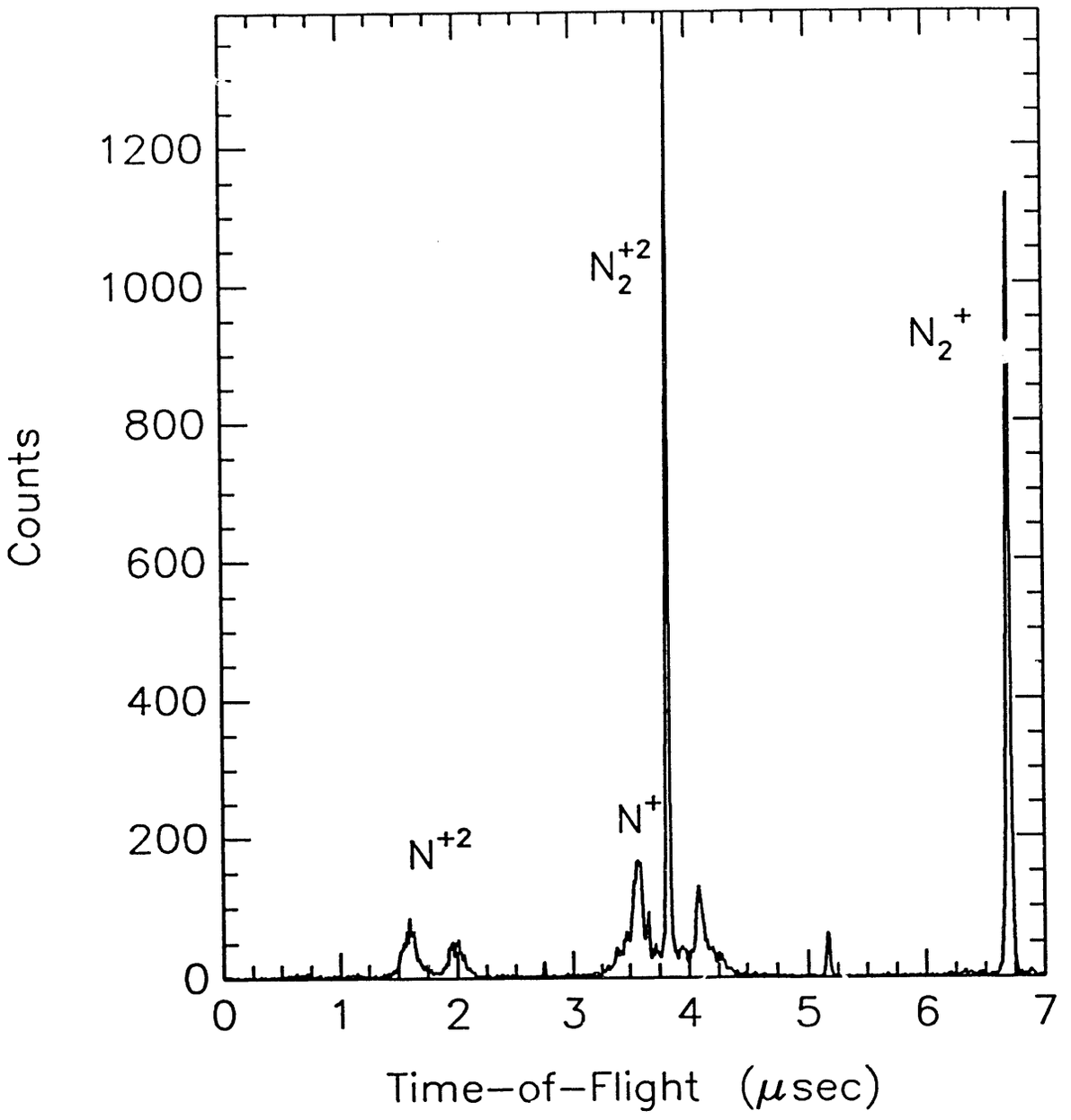

FIGURE 3.4 Time-of-flight spectrum at N_2 at 380 eV incident light energy and 70 V extraction potential.

high field. Figures 3.5 and 3.6 show the results normalized at the π^* resonance. It is clear from the figures that N_2^+ is enhanced only on the $1s\rightarrow\pi^*$ resonance, whereas N^+ and N^{+2} are present in the entire spectrum. This result is consistent with previous studies.[12] N_2^+ is only present if the final state is one of first 5 singly charged states listed in table 3.1. Only the $1s\rightarrow\pi^*$ resonance can relax to these states. A comparison of the low field sweeps of $N^+ + N_2^{+2}$ and N^{+2} with the high field sweeps shows that both N^+ and N^{+2} are enhanced at the Rydberg series and above the threshold in the high field sweeps relative to the low field sweeps. Since the high field configuration is more sensitive to higher kinetic energy ions, there are proportionally more higher kinetic energy N^+ and N^{+2} at the Rydberg series and above the ionization threshold. This will be apparent in the kinetic energy distribution.

To see if vibrational excitation has any effect on the branching ratios, sweeps of the different fragments were taken over the $1s\rightarrow\pi^*$ resonance. The high field spectra are shown in Figure 3.7, and least squares fits to both the low field and high field data are presented in table 3.3 with the absorption results of Chen et. al.[13] Although the Franck-Condon factors for N_2^{+2} do not agree with Chen et. al.'s values within the statistical error, the high field and low field FCFs agree with each other within the statistical error, which confirms that for both fields the entire solid angle is collected. Differences between the N_2^{+2} and absorption FCFs could arise from differences in the least squares fitting procedures and the experimental resolution. The high field and low field N^+ results are also in reasonable agreement with each other. However, there is a statistically significant difference between the FCFs of the 401.1 eV peak measured in the N^+ channel and that measured in the N_2^+ channel. Figure 3.8 shows the N^+ spectrum divided by the N_2^+ spectrum at the top of the figure. The bottom of the figure shows the N^{+2}, and the N_2^+ spectrum is in the middle for an energy reference. Both the N^+/N_2^+

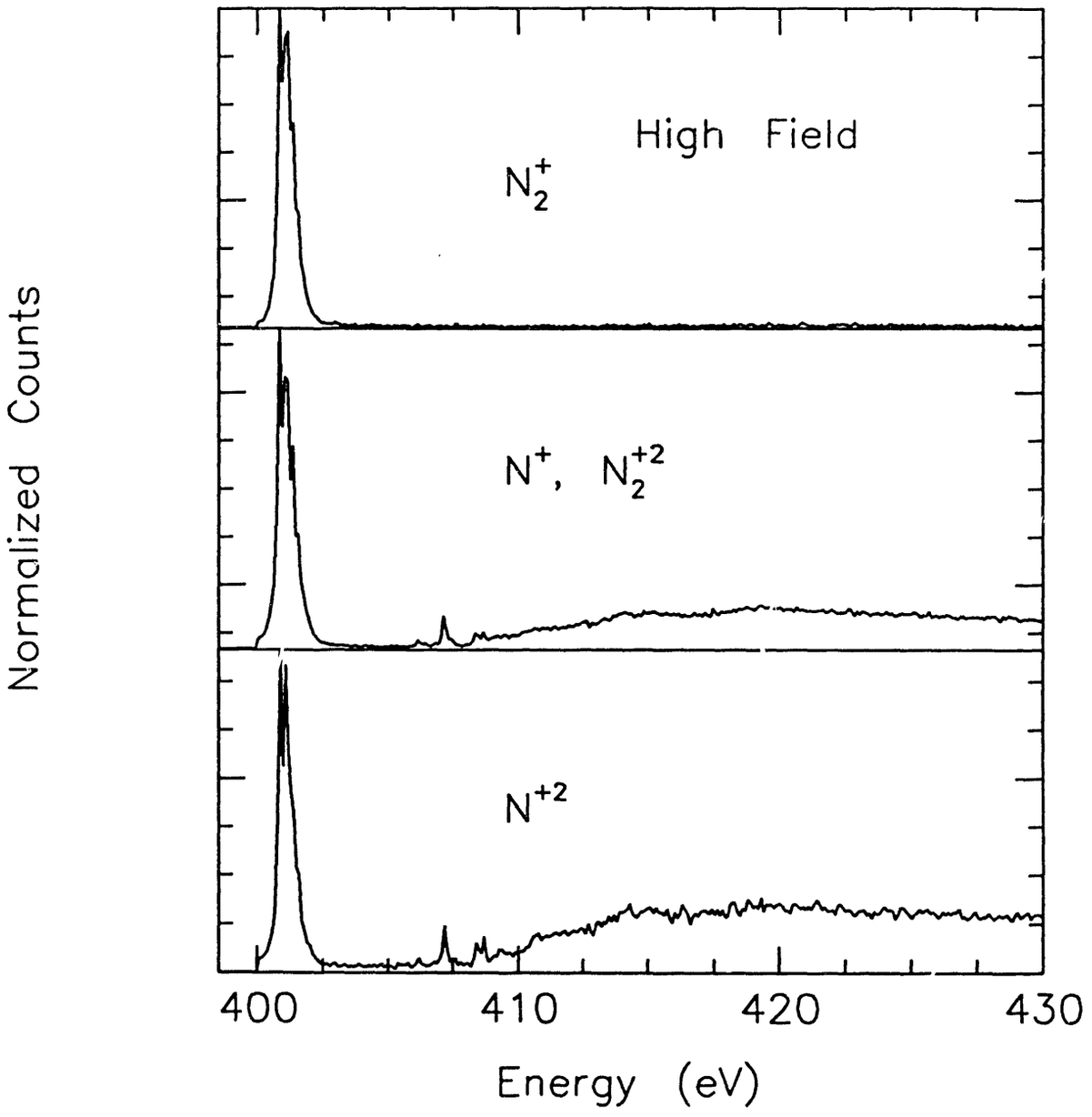

FIGURE 3.5 Ion intensity as a function of incident light energy with 120 V extraction field.

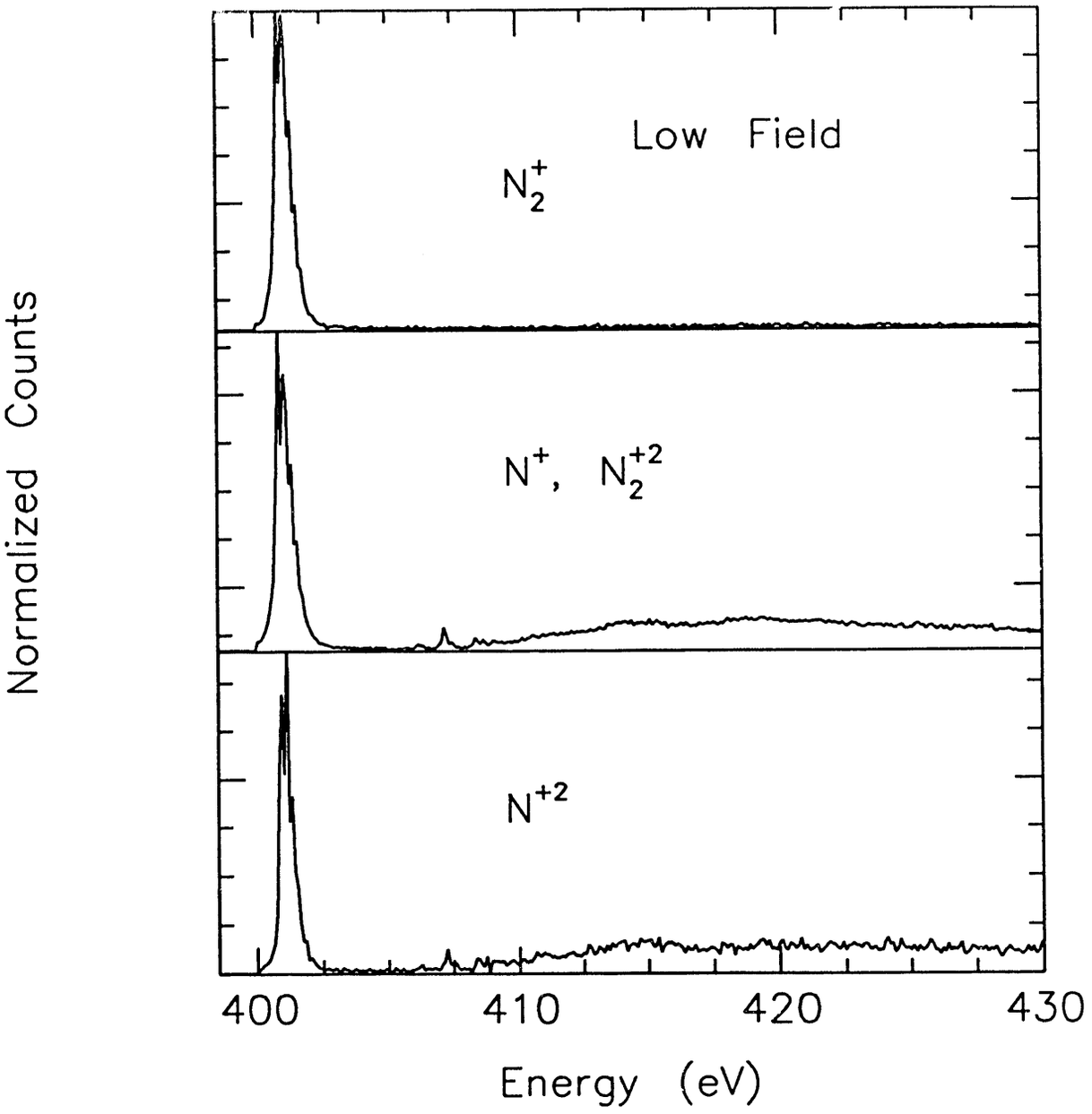

FIGURE 3.6 Ion intensity as a function of incident light energy with 30 V extraction field.

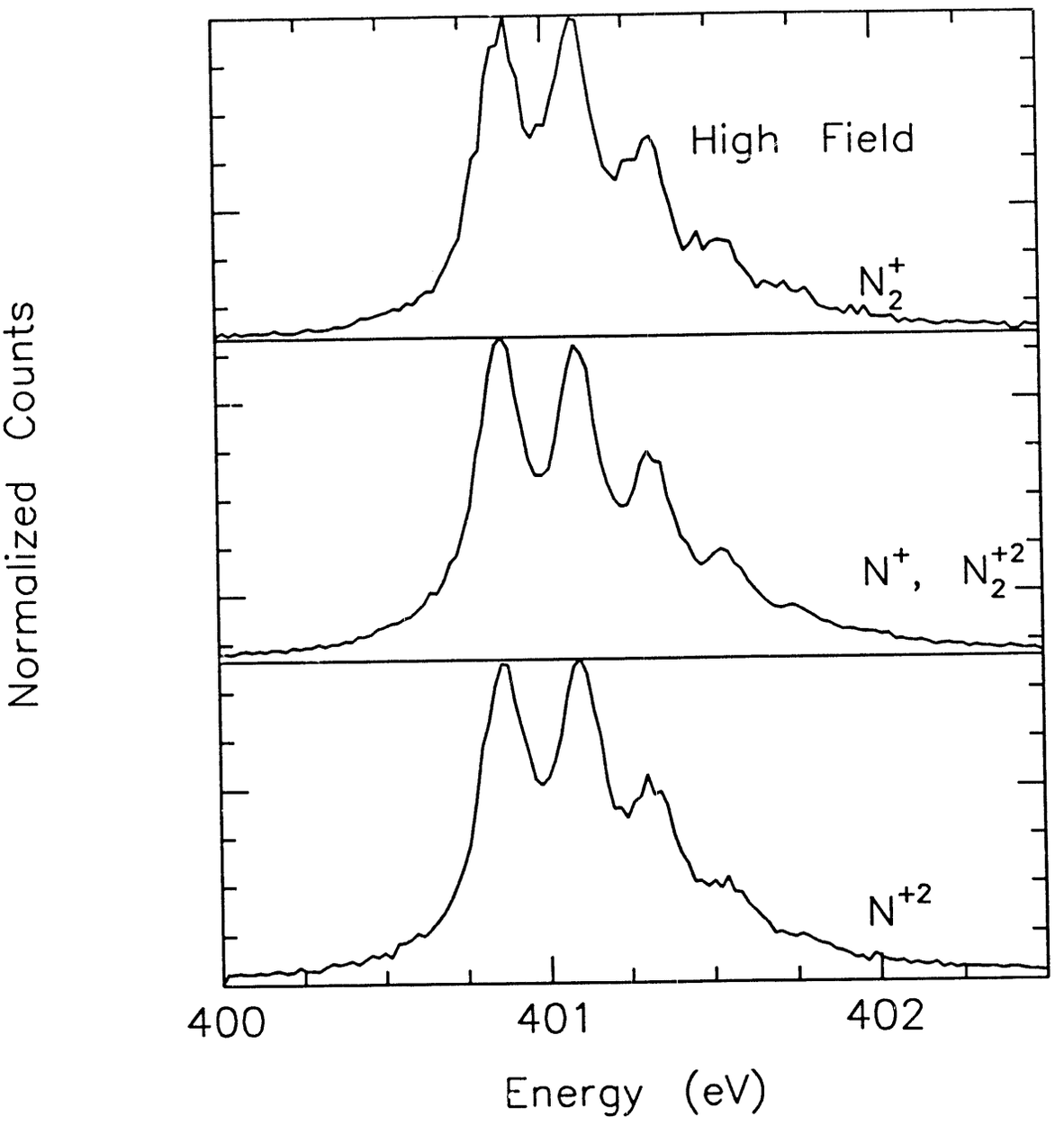

FIGURE 3.7 Ion intensity as a function of incident light energy with 120 V extraction field across the π^* resonance.

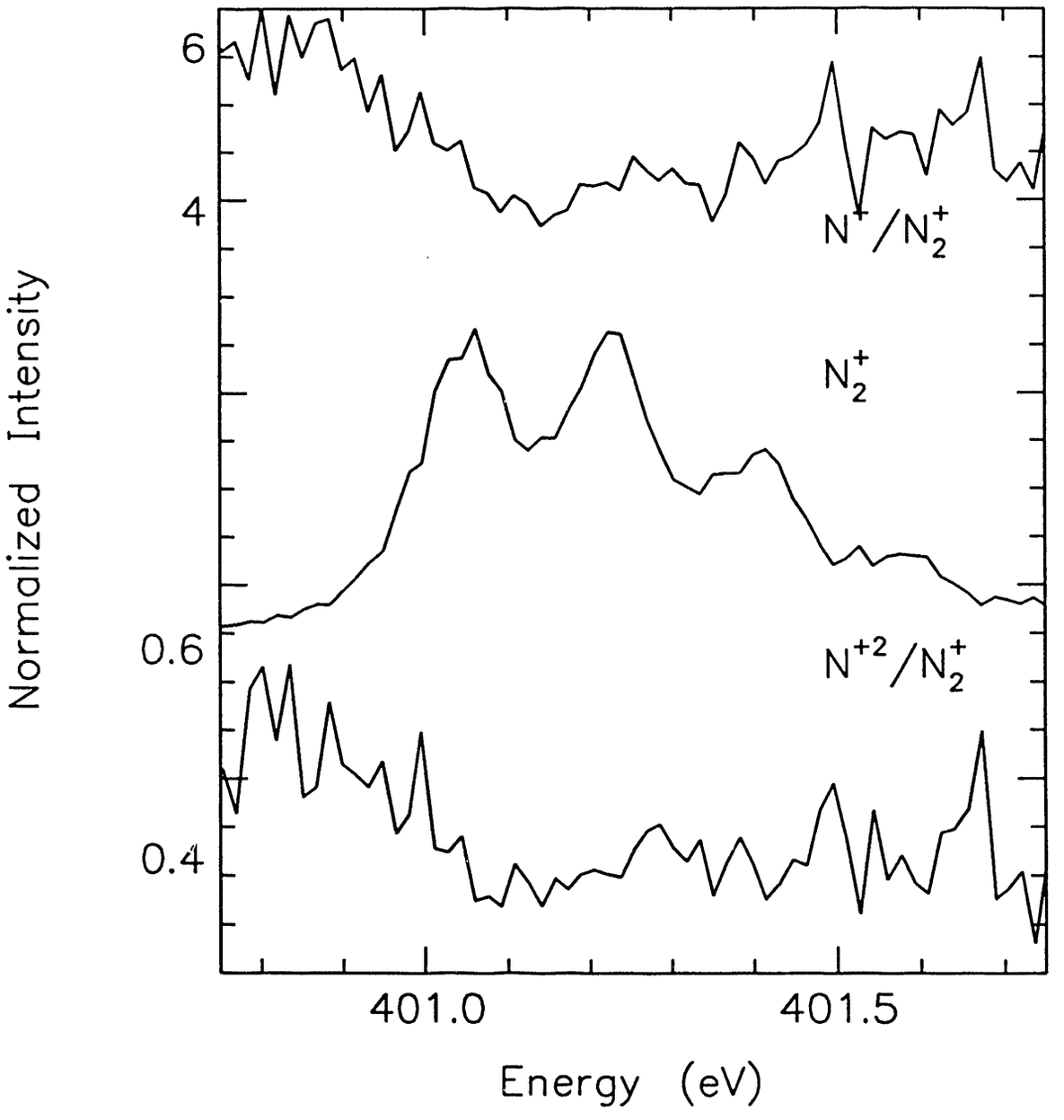

FIGURE 3.8 N^+ and N^{+2} intensity divided by N_2^+ intensity across the π^* resonance with 120 V extraction field.

N^+		N_2^+		N^{+2}		Absorption[a]	Energy (eV)
120 V	30 V	120 V	30 V	120 V	30 V		
1.000 ± 0.007	1.000± 0.007	1.000 ± 0.014	1.000 ± 0.011	1.000 ± 0.014	1.000 ± 0.013	1.000	400.868
0.808 ± 0.006	0.800 ± 0.006	0.900 ± 0.013	0.917 ± 0.010	0.843 ± 0.009	0.987 ± 0.013	0.968	401.099
0.512 ± 0.004	0.521 ± 0.004	0.537 ± 0.010	0.553 ± 0.008	0.511 ± 0.006	0.448 ± 0.007	0.564	401.327
0.238 ± 0.003	0.257 ± 0.003	0.222 ± 0.005	0.258 ± 0.005	0.227 ± 0.004	0.0186 ± 0.004	0.250	401.551
0.055 ± 0.002	0.096 ± 0.002	0.105 ± 0.003	0.108 ± 0.003	0.076 ± 0.002	0.044 ± 0.002	0.088	401.771
0.081 ± 0.002	0.049 ± 0.001	0.034 ± 0.002	0.042 ± 0.002	0.023 ± 0.001	0.027 ± 0.002	0.030	401.987
						0.011	402.199
						0.004	402.408

Table 3.3 Franck-Condon factors for the sweeps of ionic fragments
a. C. T. Chen et. al. Ref. 13.

and the N^{+2}/N_2^+ ratios show a significant (30%) decrease across the ground vibrational state followed by a slight increase for the remainder of the $1s \rightarrow \pi^*$ resonance. Therefore at energies below the resonance there is less access to the stable N_2^+ single valence hole states. Whereas on the resonance the participant Auger decay channels are open. The shape of this effect is evident in the FCFs. This result also implies that, since the FCFs are not the same in every exit channel, it is necessary to be cautious about using anything other than strictly absorption spectroscopy to determine them.

Figure 3.9 shows sweeps of N^+, N_2^+, and N^{+2} across the Rydberg region, and table 3.4 shows the results again compared to the absorption results of Chen et. al. In

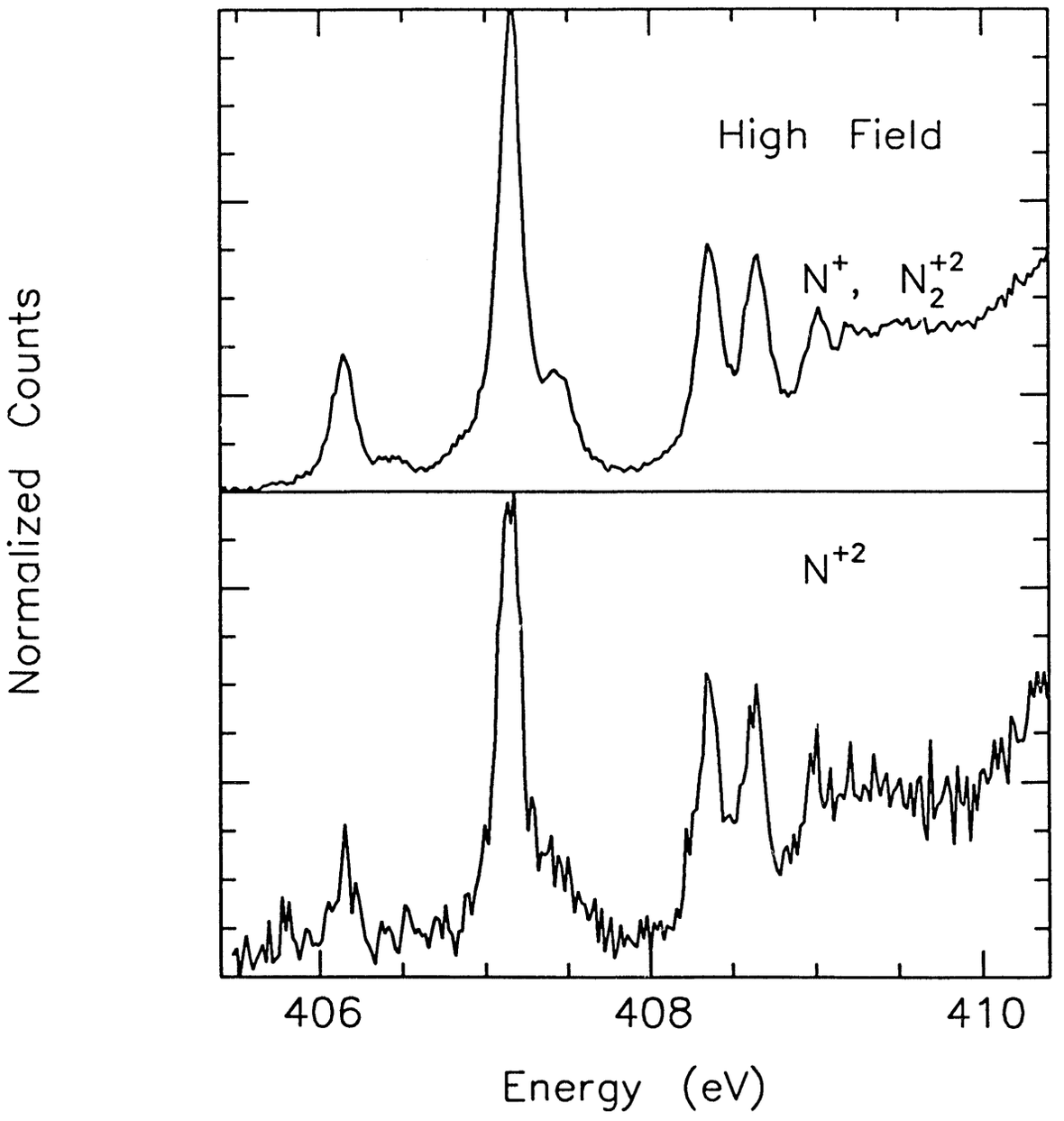

FIGURE 3.9 Ion intensity as a function of incident light energy with 120 V extraction field across the Rydberg series.

this region, the asymmetry parameter has been measured at a few points with lower resolution by Saito and Suzuki[14] and found to vary from 1.4 to -0.066. They found that

Transition/ Energy[a]	N^+		N^{+2}		Absorption [a]	β	β[b]
	120 V	30 V	120 V	30 V			
3sσ 406.15 eV	1.000 ± 0.013	1.00 ± 0.03	1.00 ± 0.03	1.0 ± 0.1	1.000	1.1 ± 0.2	1.4 ± 0.3
3sσ + v 406.44 eV	0.169 ± 0.004	0.085 ± 0.006	0.265 ± 0.013	0.17 ± 0.03	0.115	0.45 ± 0.35	
3pπ 407.12 eV	4.1 ± 0.4	5.82 ± 0.13	5.90 ± 0.15	5.2 ± 0.4	2.307	-0.02 ± 0.04	-0.7 ± 0.2
3pσ 407.33 eV					0.120		
3pπ + v 407.44 eV	0.903 ± 0.02	1.15 ± 0.03	1.20 ± 0.04	0.77 ± 0.08	0.369	-0.45 ± 0.5	-0.4 ± 0.2
4sσ 408.35 eV	1.98 ± 0.02	2.67 ± 0.06	3.29 ± 0.09	2.6 ± 0.2	1.164	0.10 ± 0.11	
4pπ 408.63 eV	1.97 ± 0.02	2.17 ± 0.05	2.58 ± 0.07	2.3 ± 0.2	1.012	-0.01 ± 0.23	
5sσ 408.99 eV	1.193 ± 0.014	0.65 ± 0.02	0.98 ± 0.03	0.86 ± 0.09	0.638	0.7 ± 0.3	

Table 3.4 Relative Intensities and assymetry parameters for the Rydberg series.
a. C. T. Chen et. al., Ref. 13.
b. Suzuki and Saito, Ref. 12.

N^+ and N^{+2} have the same angular distribution. By assuming that the differences between the relative intensities of the fragments we measured at 90° and the absorption spectrum of Chen et. al. are solely from the asymmetry parameter, β, this was calculated for the high and low field spectra of N^+ and N^{+2}, and the average of those values is shown in table 3.4. This assumes the branching ratios for the different fragments are

constant over the Rydberg series, and so are their kinetic energy distributions, which are not good assumptions. Considering that this calculation was made by comparing my differential measurement with Chen et. al.'s total absorption measurement, the agreement with Saito and Suzuki is fairly good. The $1s\rightarrow 3s\sigma$ resonance is the only well separated resonance, and it agrees within the estimated error. It is not very likely that the $1s\rightarrow 3s\sigma$ β changes as much as it appears to change in table 3.4 with one extra quantum of vibrational excitation. It is more probable that there is a change in the kinetic energy distribution. The differences between the high field and low field branching ratios support this, since the high field results show a much stronger resonance on v+1 than the low field results.

The agreement with Saito and Suzuki for the asymmetry parameter deteriorates on the $1s\rightarrow 3p\pi$ resonance. Since their resolution differs from ours, and it appears as though the asymmetry parameter undergoes some rapid oscillations, it is possible that this difference is because we each are averaging over different Rydberg states. However, it is also likely that the assumptions I used to calculate β are not valid. As the extraction field is raised, the efficiency of collection for higher kinetic energy ions is increased. If, however, the collection angle becomes very large, the angular information is lost and all βs appear to be zero. For βs less than zero, measured at 90°, this means as the field is increased the intensity decreases relative to those transitions with β greater than zero. Unfortunately the results are only this simple if the kinetic energy distribution is the same for every member of the Rydberg series. For N^{+2} all of the high field values are greater than the low field values relative to the $1s\rightarrow 3s\sigma$ transition. Therefore the kinetic energy distribution for the $1s\rightarrow 3s\sigma$ transition probably contains more low kinetic energy N^{+2} than the other Rydberg states. This is not the determining factor for N^{+}. Only two states are increased relative to the $1s\rightarrow 3s\sigma$ resonance with increased extraction field, the $1s\rightarrow 3s\sigma$ +1v and the $1s\rightarrow 5s\sigma$ resonances. Both of these transitions should

have relatively high βs, but since neither is greater than β for the 1s→3sσ transition, they must have kinetic energy distributions which are peaked toward higher energies than the 1s→3sσ transition. Because the βs for the other states are less than that for the 1s→3sσ transition, it is impossible to make any conclusions about their kinetic energy distributions from these data.

Kinetic Energy Distributions

The kinetic energies of the dissociation fragments reveal the energies and shapes of electronic states' potential surfaces. In this experiment the extraction field was not pulsed, and all the ions are collected within 10 μsec. Therefore the ions collected can be separated into three categories. States which dissociate while the molecule is traveling down the flight tube produce a complex time-of-flight pattern, which was not observed for N_2. Metastable states with lifetimes longer than a few microseconds are detected in the undissociated state, and those with lifetimes shorter than a few nanoseconds appear as their dissociation fragments. These dissociated fragments appear at kinetic energies corresponding to the energy difference between the fragments and the position on the dissociative surface of the equilibrium bond length of the initial state. Energy conservation reveals which Auger peaks correspond to these dissociative states and, by elimination, which are metastable.

Accurate measurement of the kinetic energies is not trivial. Lower extraction fields provide better resolution, but do not efficiently collect higher kinetic energy ions. For this reason three different extraction fields were used. Figure 3.10 shows kinetic energy distributions for N^+ at the 1s→π* transition and at the 1s→3pπ Rydberg transition for all three fields. All of the kinetic energy distributions presented were corrected for the calculated transmission of the analyzer. This figure illustrates some

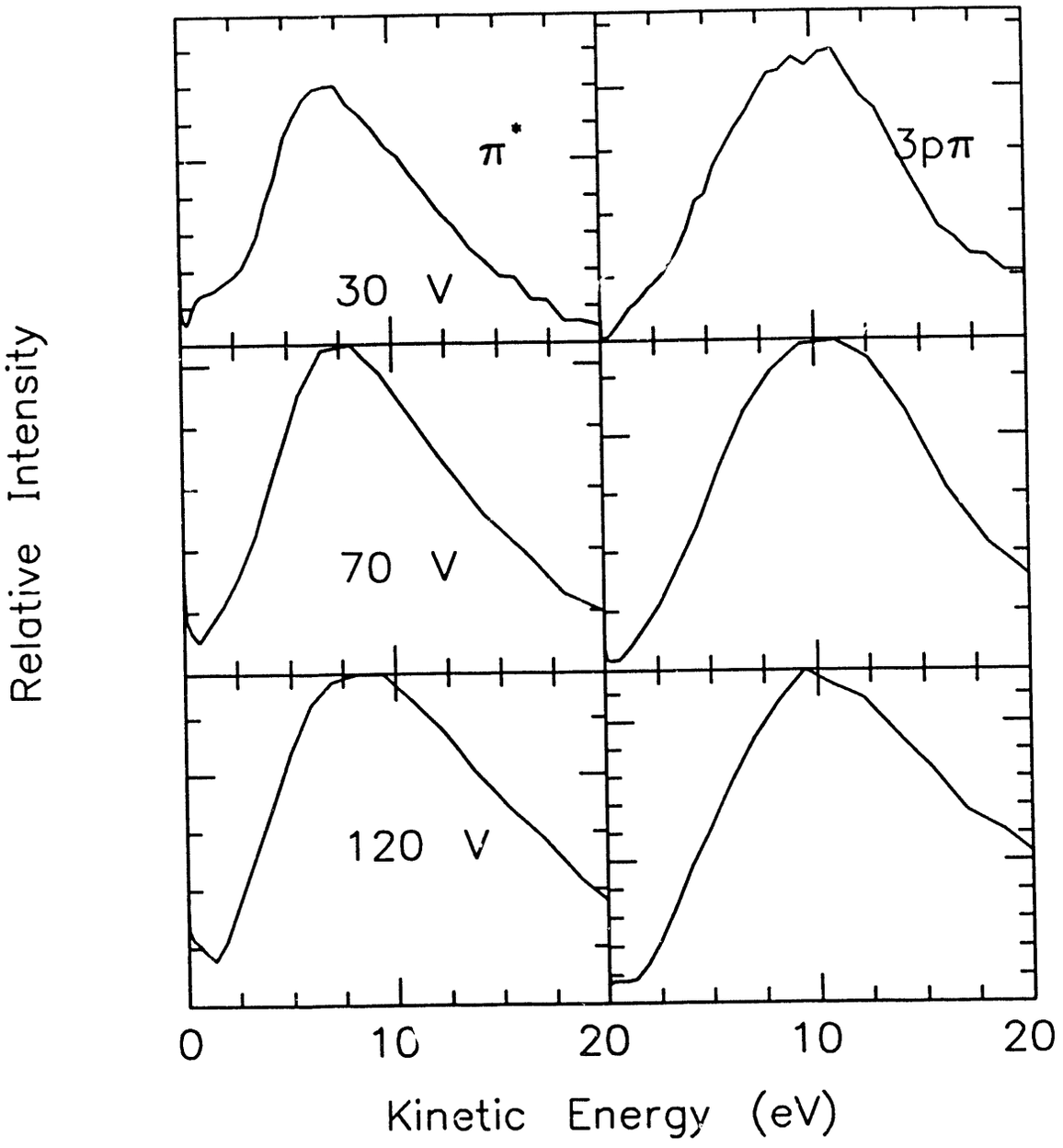

FIGURE 3.10 Kinetic energy distributions for N^+ at the π^* resonance and the $3p\pi$ resonance for three different extraction fields.

important difficulties associated with this measurement. For the $1s\rightarrow\pi^*$ transition, the features are not simply broadened with higher extraction field, but the maximum is also shifted to slightly higher kinetic energies. For this transition $\beta = -1.0$, which means the maximum occurs at 90°. Because the lower kinetic energy ions are averaged over a larger solid angle, at higher extraction fields the distribution is biased toward higher kinetic energy ions. For the $1s\rightarrow 3p\pi$ transition in figure 3.6, this is not the case, since $\beta = 0.0$. Therefore the results for all the extraction fields look quite similar on this transition. Aside from effects due to the angular distribution, in these data the electron used for the start signal can affect the kinetic energy distributions, since the different extraction fields apply to the electrons also. The ratio of the efficiency of electron collection at 120 V extraction potential to that at 30 V extraction potential decreases with increasing kinetic energy. Therefore the higher extraction potential is more biased toward low kinetic energy electrons. Over the energy range of the Auger electrons, 260-370 eV, this is a relatively small effect, less than 10%. At lower kinetic energies (0-100 eV), however, this is a much bigger effect. These very low kinetic energy electrons must be from double Auger decay, and therefore dissociative states reached through two electron relaxation are more prominent in the high extraction field kinetic energy distributions.

Two methods for some dissociative state selection are either measuring an Auger electron of a specific energy in coincidence with the ion, or using the tendency of different core-excited or ionized states to Auger decay to a specific state. By comparing the results from different extraction fields, kinetic energies from double Auger decay can be separated from those from simple Auger decay. For N_2, the Auger spectrum has been measured for the core-ionized state and the $1s\rightarrow\pi^*$ transition. With current synchrotron radiation technology, the Rydberg series is too weak to be the object of a differential experiment. However, some things are known about relaxation through this

series. N_2^+ is not enhanced relative to background, so participant decay of the excited electron to single valence hole states does not happen. This is the result of the Rydberg orbitals' very low overlap with the core hole compared to the other molecular orbitals. Therefore two types of Auger decay are possible, spectator Auger decay and double Auger. It has been previously shown with threshold photoelectron spectroscopy[11] that the tendency for double Auger decay increases through the Rydberg series.

Figure 3.11 shows the kinetic energy distributions of N^+ and N^{+2} at three nonresonant energies. All three of the 30 V extraction potential N^+ spectra show a prominent, relatively narrow, peak at 6.4 eV, followed by a broader distribution centered around 12 eV kinetic energy. Possibly the 380 eV spectra contain three narrow distributions centered at 6, 11 and 15 eV kinetic energy. In the higher extraction fields, the higher kinetic energy ions are enhanced relative to the narrow peak at 6.4 eV. Since β at 380 is slightly less than zero, -0.15, it is possible that this is the usual angular distribution effect. However, β for both other energies in figure 3.11 is greater than zero, therefore it is likely that this higher kinetic energy structure is from a many electron transition. At 380 eV, core-excited or ionized transitions are not allowed, therefore the final states can be in any charge states. However, the similarity between the 380 eV spectra and the others in figure 3.11 indicates that the majority of the transitions involve more than one electron. The presence of N^{+2} supports this. The N^{+2} kinetic energy distribution shown in figure 3.11b is peaked at approximately 14 eV and possibly a second maximum is present at approximately 30 eV. Given the uncertainty in the kinetic energy distribution, it is possible that the 12 eV N^+ and the 14 eV N^{+2} are from the same dissociation event as momentum conservation pair and correspond to the dissociated fragments $N^+(^3P) + N^{+2}(^2P)$, previously observed by Eberhardt et. al.[9] in coincidence with an Auger electron of 310 eV kinetic energy. Suzuki and Saito have measured the total kinetic energy released for N^+ and N^{+2}.[15] They found a broad

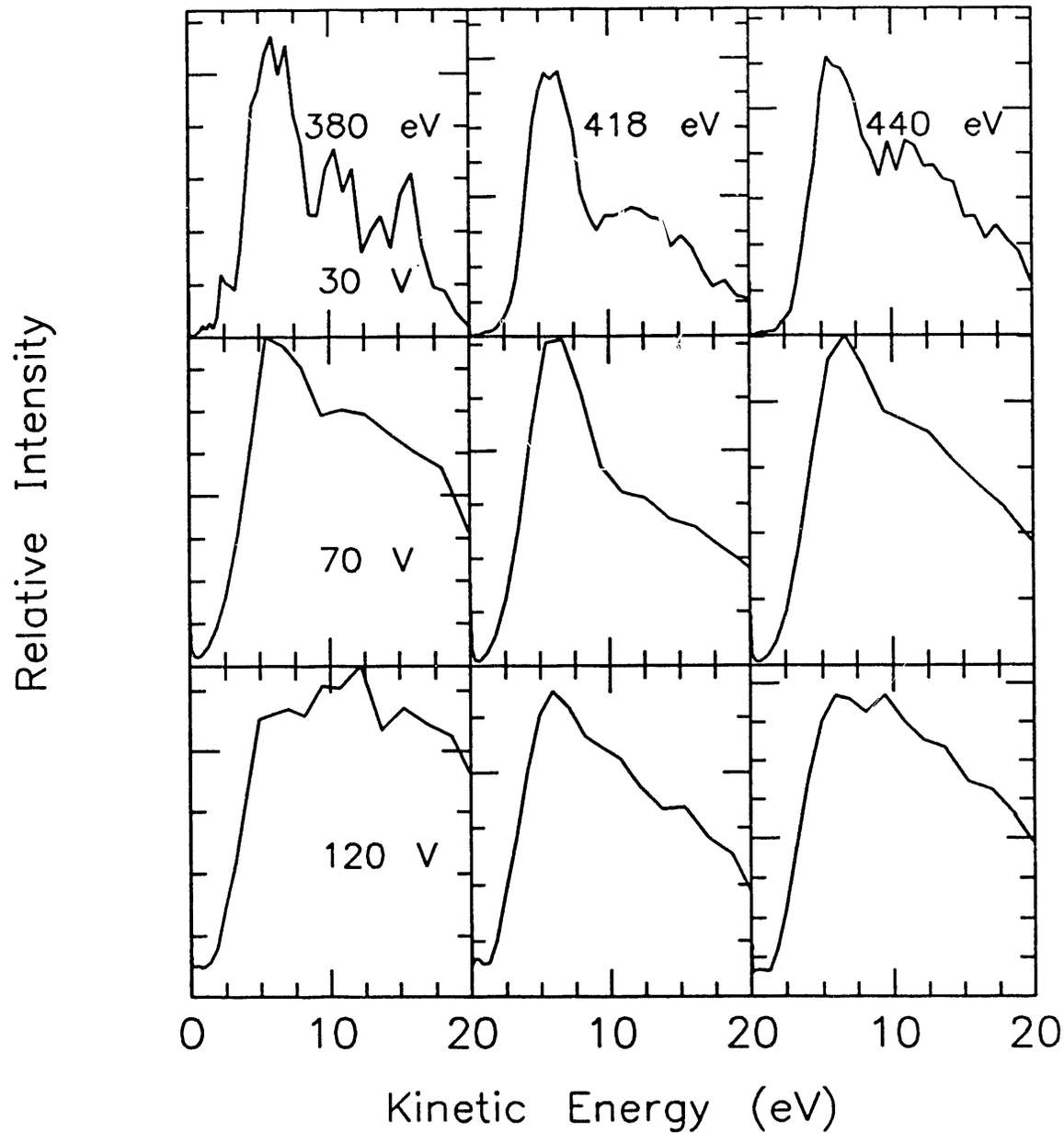

FIGURE 3.11a Kinetic energy distributions for N^+ at three nonresonant energies for three different extraction fields.

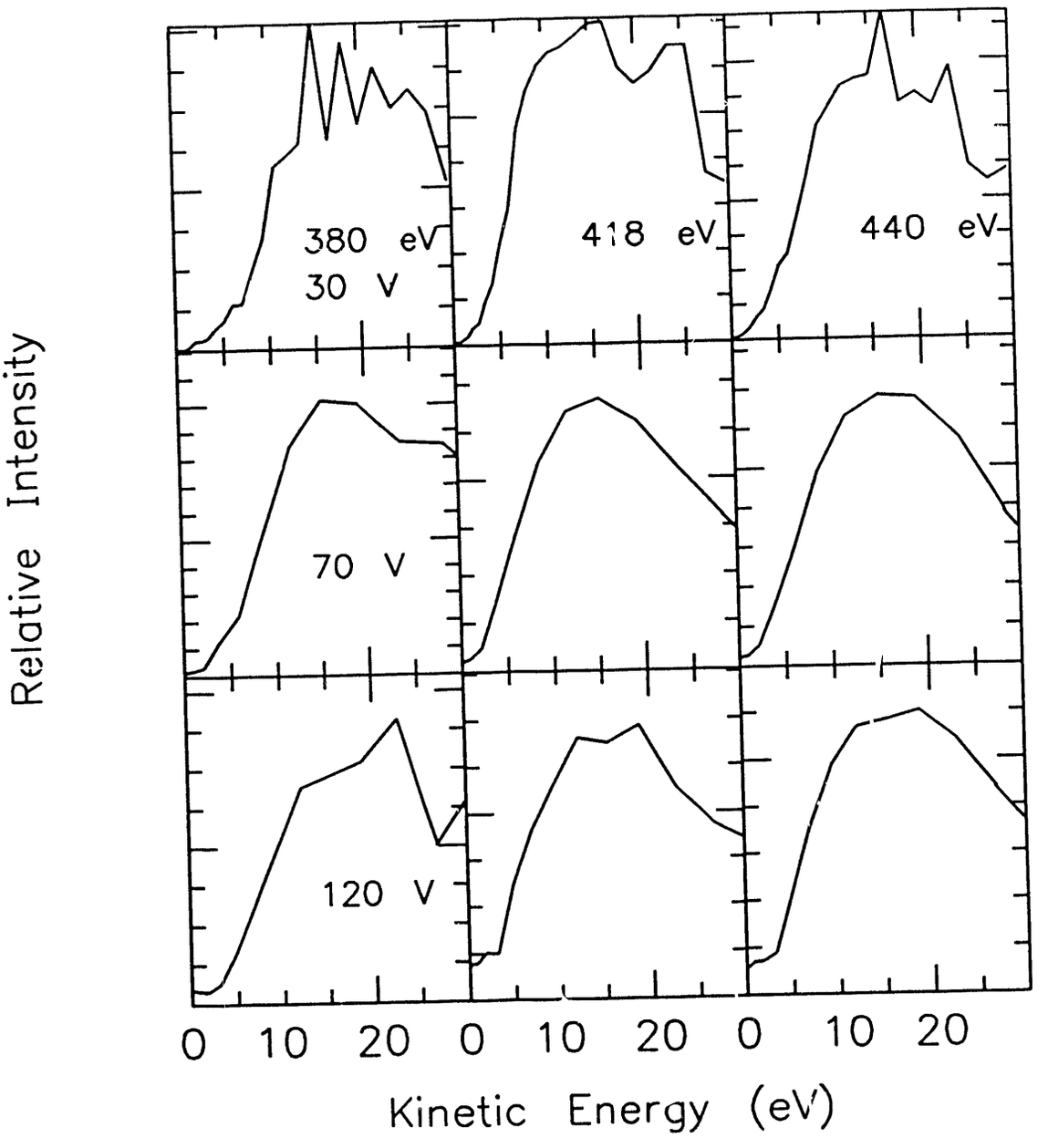

FIGURE 3.11b Kinetic energy distributions for N^{+2} at three nonresonant energies for three different extraction fields.

distribution with significant intensity from 21 to 35 eV, which could be this same pair. That this pair is also very intense in the 440 eV spectra supports this assignment, since at that energy it can be accessed through a single Auger transition from the core and valence double ionized states and not just through a double Auger transition as at 418 eV.

The peaks centered at approximately 6.4 eV must be from a state with the configuration $1\pi_u^{-1}$ val^{-1}. Eberhardt et. al.,[9] in coincidence with 360 eV electrons found N^+ with 5.5 ± 0.8 eV kinetic energy and in coincidence with 363 eV electrons, ions with 4.5 ± 0.6 eV, and Suzuki and Saito found the N^+ kinetic energy distribution to have a broader maximum from 4-5 eV. Since this structure does not change with different extraction fields, it is probably from an N_2^{+2} state. If it dissociates to the ground state of the fragments, at 38.8 eV, by looking at table 3.1 it can be assigned primarily to the $^1\Pi_g$ state with some intensity also from the $^1\Delta_g$ state. Also, some intensity could be attributed to slightly higher kinetic energy states visible in coincidence with 350 eV Auger electrons in the work of Eberhardt et. al.[9] Lastly there appears to be some intensity in the N^{+2} spectra at approximately 25 eV kinetic energy. Again using table 3.1 and assuming ground state fragments, this corresponds to a N_2^{+2} state of at least 104 eV or an N_2^{+3} state of 118 eV. Since the $2\sigma_g^{-2}$, $^1\Sigma_g^+$, at 95 eV is the highest N_2^{+2} state which has the core electrons present, this very high energy N^{+2} cannot be from any N_2^{+2} dissociative surface. Interestingly, Eberhardt et. al. found N^{+2} and N^+ in coincidence with 315 eV Auger electrons. They assumed that the $^1\Sigma_g^+$, $2\sigma_g^{-2}$, state at 95 eV dissociates to these fragments, but it is possible that there e ists a dissociative state of the triple ion close in energy.

Figure 3.12 shows the kinetic energy distribution of N^+ for the different resonant electronic states and just beyond the 1s ionization threshold. The highly excited neutral states can decay to singly ionized surfaces. Previous studies[7] have shown that

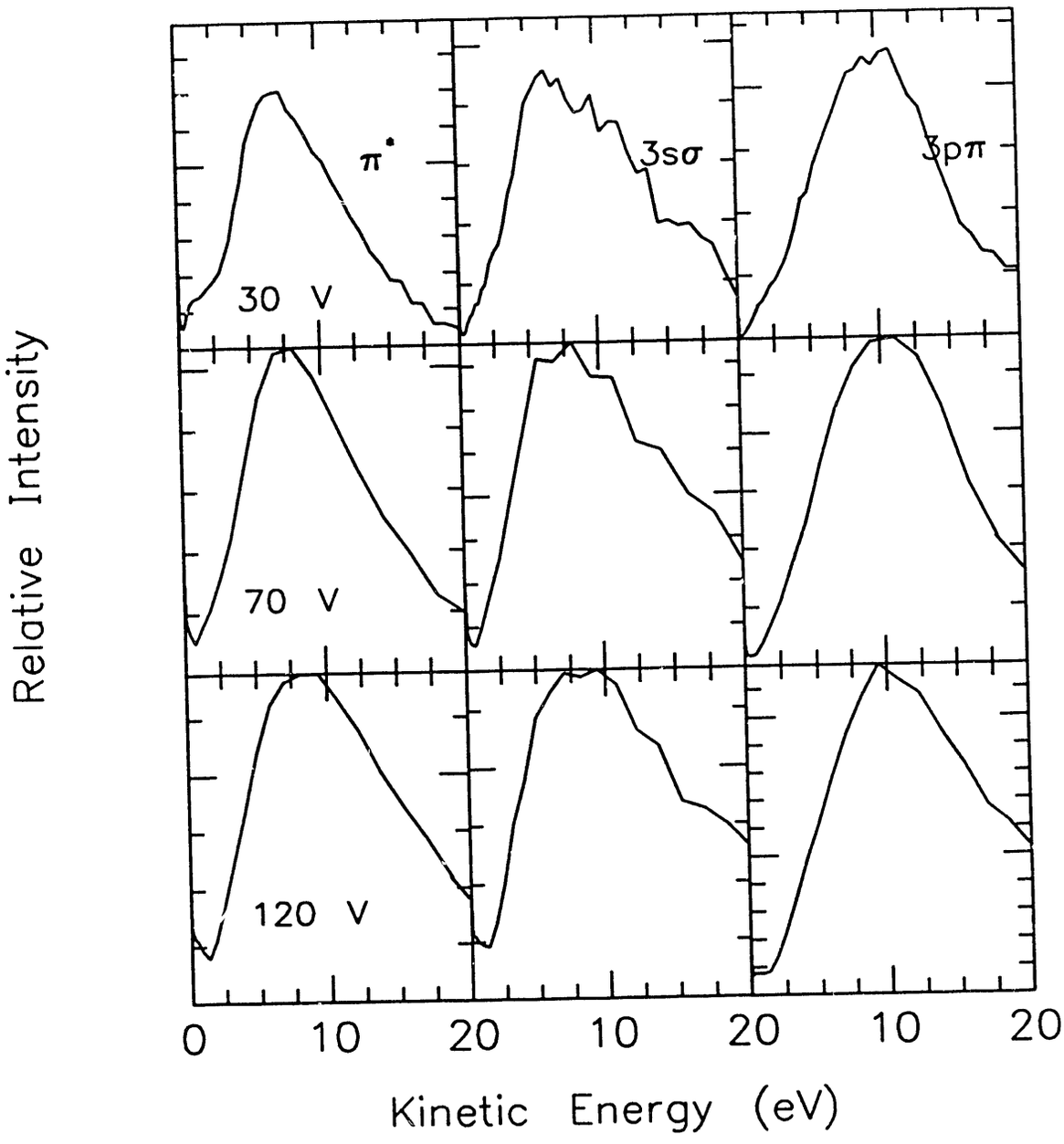

FIGURE 3.12a Kinetic energy distributions for N^+ at different electronic transitions for three different extraction fields.

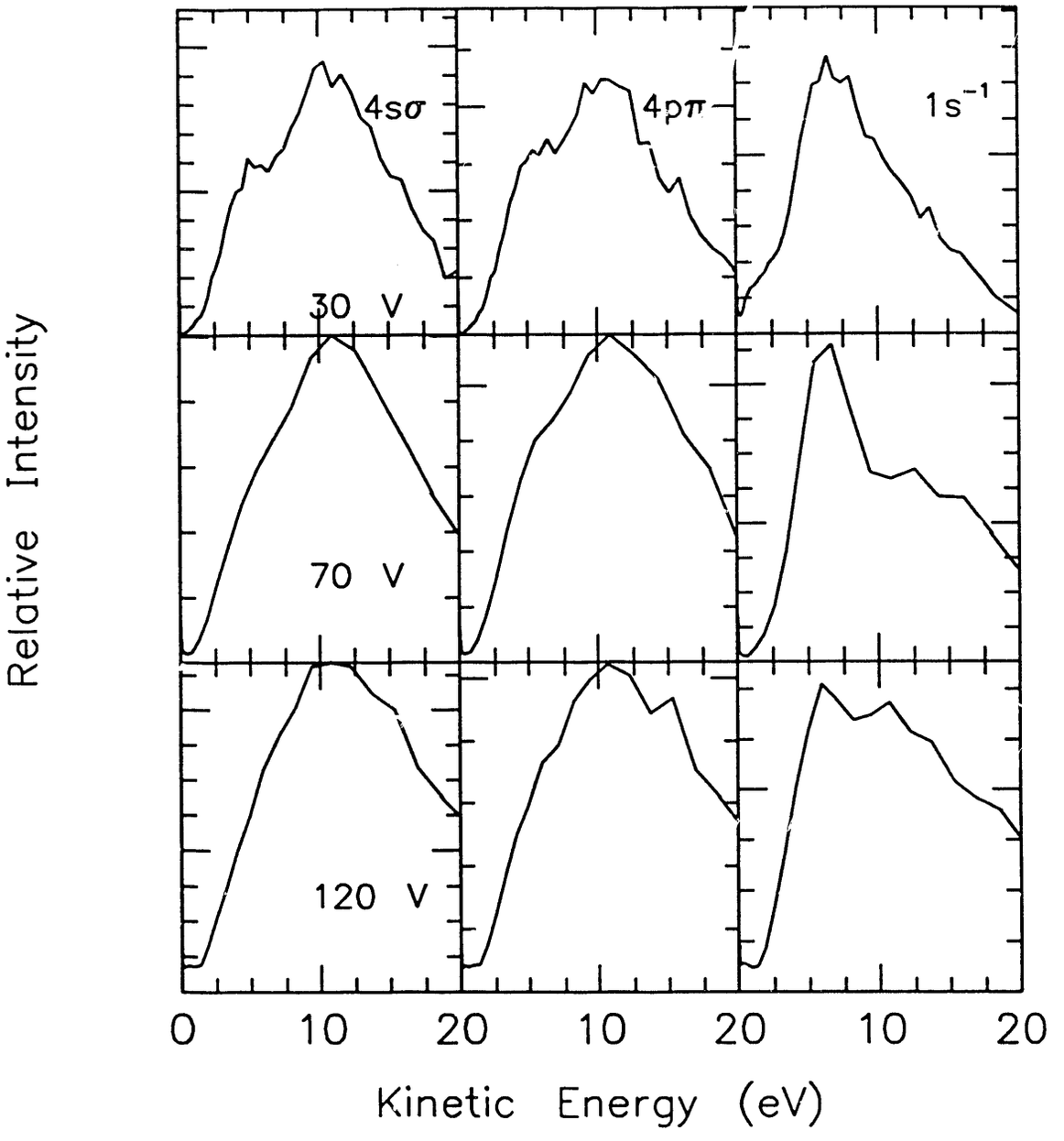

FIGURE 3.12b Kinetic energy distributions for N^+ at different electronic transitions for three different extraction fields.

approximately 15% of the $1s \rightarrow \pi^*$ excited states relax to N_2^+. This is the result of participant Auger transitions to the single valence hole states. The only other participant decay state energy allowed is the inner valence hole state, $2\sigma_g^{-1}$, $^2\Sigma_g^+$, at 39.75 eV which dissociates $N^+(^3P) + N(^4S)$.[5] This would produce N^+ ions with 7.7 eV kinetic energy, which is very close to the maximum of the N^+ intensity. The N^+ kinetic energy distribution looks deceptively like a Maxwell distribution. If it is fitted with a Maxwell distribution function, the activation energy is ~ 4 eV and the random energy or temperature is approximately 3.75 eV. This seems to support the assignment of most of the N^+ ions to the $2\sigma_g^{-1}$, $^2\Sigma_g^+$ state, with however a large portion of the excess energy randomized in the molecule, and not directed along the dissociation axis. The lower energy N^+ ions could be from the low energy spectator states to the ground state of N + N^+ or the first few excited dissociated states.

At the $3s\sigma$ Rydberg transition, the N^+ kinetic energy distribution looks very much like it does at the π^* transition. The major difference is that there are not as many very low energy ions. Since the spectator transition states are higher in binding energy at the $3s\sigma$ transition, if they dissociate to N + N^+ in either the ground state or the first few excited states, they should have approximately 5 eV higher kinetic energy. It appears as though the major dissociative channel is still the $2\sigma_g^{-1}$, $^2\Sigma_g^+$ state. At the $3p\pi$ transition, the lower β could be responsible for the increased intensity at higher kinetic energy, but the spectator decay states should also be at much higher energy and would cause the same effect in the kinetic energy distribution. Since the Auger spectra for the Rydberg states are not known, a definite assignment for the dissociative states is not possible. At the n=4 resonances, intensity starts to grow in at approximately 6 eV, which is like the distribution for the $1s^{-1}$ transition. This is from increased double Auger at the higher n values.

The N^{+2} kinetic energies distributions are shown in figure 3.13. These distributions look very similar except that the π^* distribution has less intensity at higher kinetic energies and the n=3 transitions have very little intensity at 10 eV. For the π^* transition, this means the excited molecules do not decay to +3 states. For the Rydberg states the N^+ ions with 10 eV kinetic energy are from either N^++ N or N^+ + N^+, unlike in the core-ionized case.

Figure 3.14 shows the N^+ and N^{+2} kinetic energy distributions for the different vibrational levels of the π^* resonance. There are no discernable differences between the vibrational levels and no strong trends across the resonance. The total energy difference between v=0 and v=4 is more than 1 eV, and this should be visible. Since more energy has been put into the molecules, it must be emitted in the only channel not measured, the Auger electron. Unfortunately at the time of this experiment, it was not possible to measure Auger spectra with vibrational resolution. To explain this phenomenon, resonant excitation followed by Auger decay quantum mechanically should be written as:

$$\langle \Psi_f | r | \Psi_r \rangle \langle \Psi_r | \Psi_i \rangle$$

where Ψ_i is the initial ground state, Ψ_f is the final dissociative state reached after Auger decay, and Ψ_r is the resonant state. Since the Auger decay is so rapid (~10 fsec), the molecule does not evolve on the core-excited surface.

Branching Ratios

The relative yields of the different ionic species determined from the time-of-flight spectra are present in table 3.5 for all three different extraction fields along with the results of Suzuki and Saito.[12] Their results agree with those of Eberhardt et. al.[7] As can be seen in table 3.5 using a simple sum of counts, the branching ratios are highly

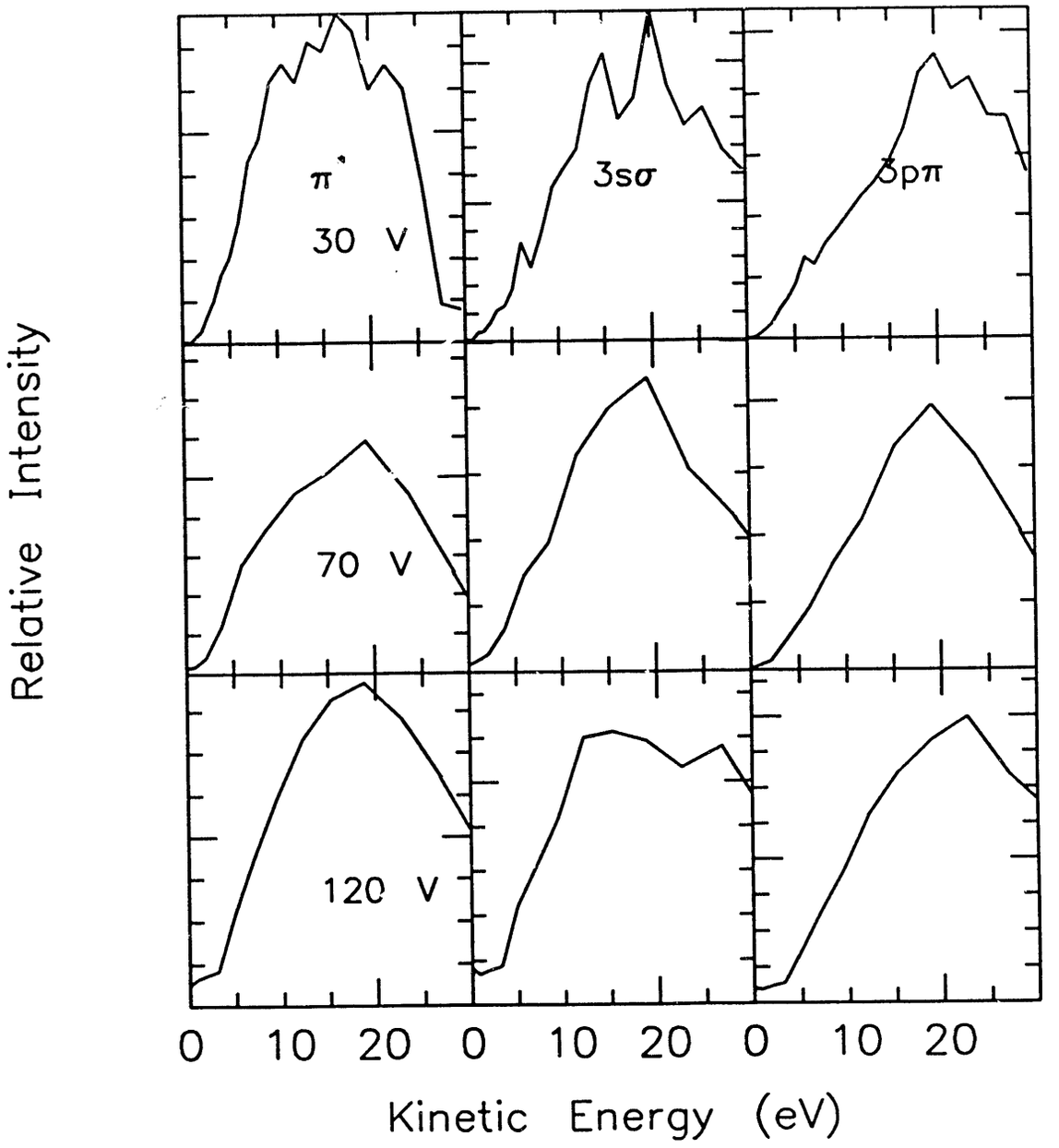

FIGURE 3.13a Kinetic energy distributions for N^{+2} at different electronic transitions for three different extraction fields.

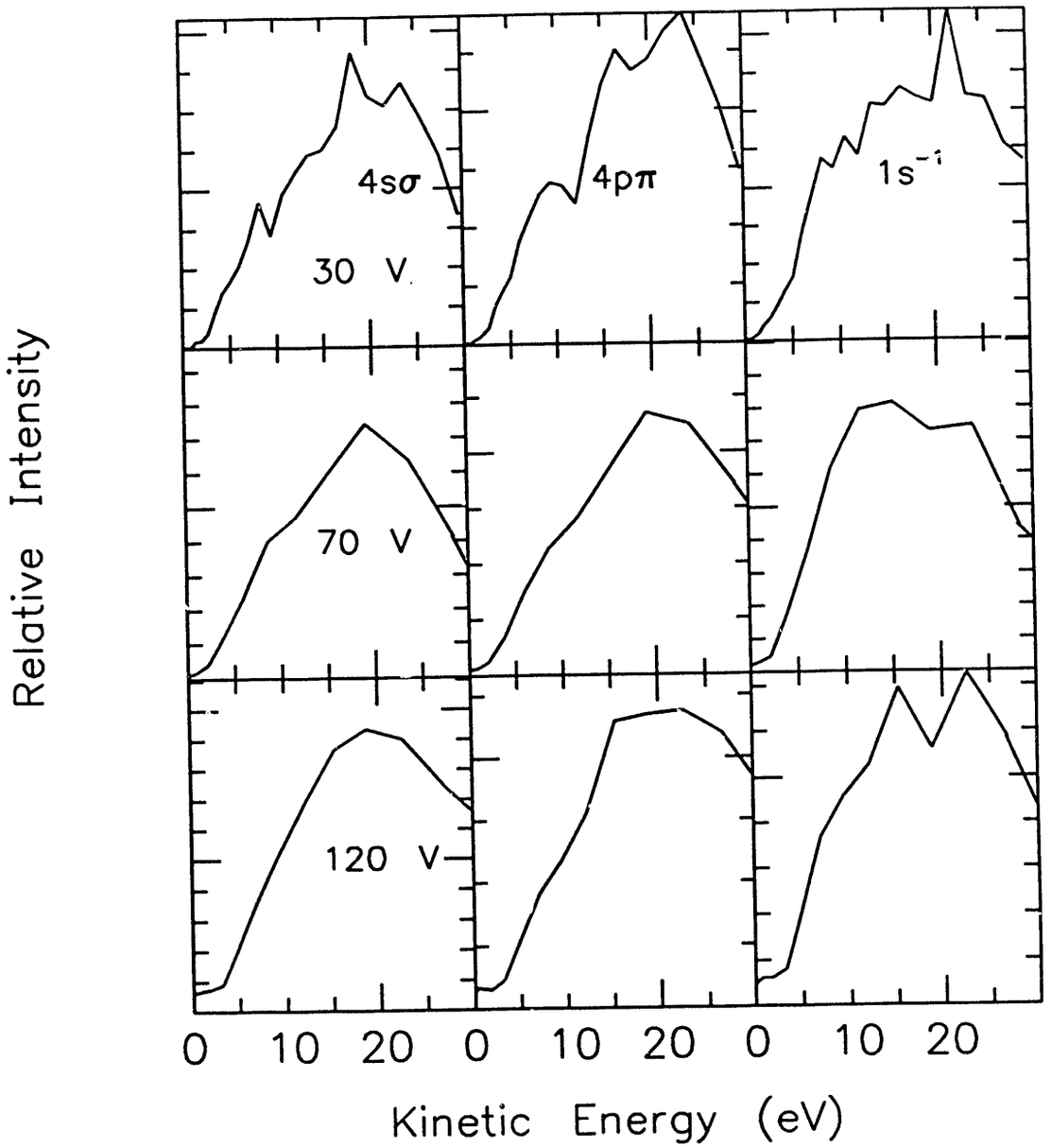

FIGURE 3.13b Kinetic energy distributions for N^{+2} at different electronic transitions for three different extraction fields.

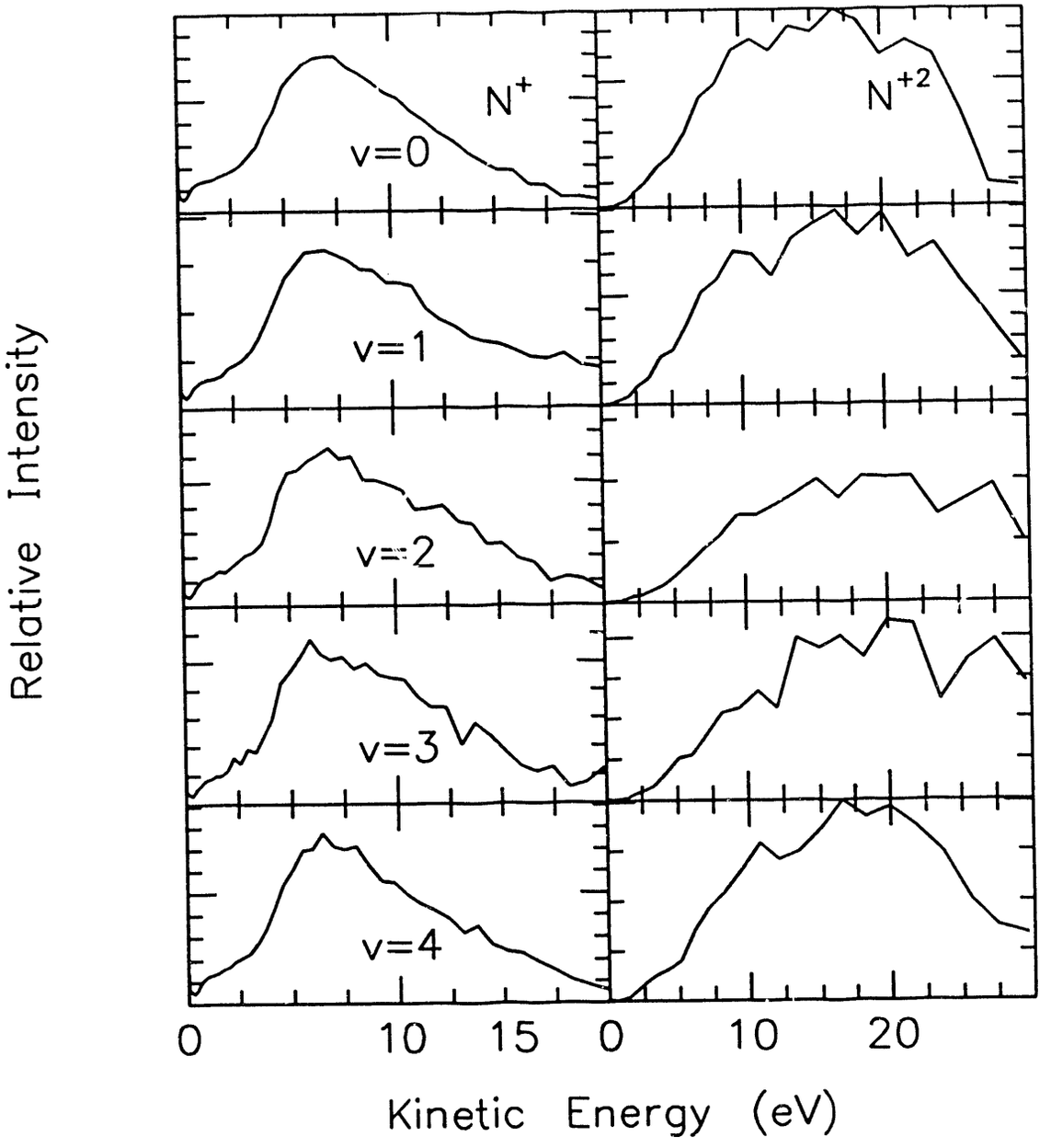

FIGURE 3.14 Kinetic energy distributions for N^+ and N^{+2} for different vibrational levels of the $1s \rightarrow \pi^*$ resonance with 30 V extraction field.

dependent on the extraction field. The analyzer would not work at higher extraction fields. To determine the branching ratios accurately, all the ions must be collected. A previous measurement of the dissociation fragments in coincidence with threshold

Transition		Branching Ratios			
		N_2^+	N_2^{+2}	N^+	N^{+2}
$1s\rightarrow\pi^*$ 401.1 eV	Suzuki and Saito[a]	8.1	4.0	75.9	11.9
	Eberhardt et. al.[b]	9.5	79		11.5
	30 V	28.4	8.9	60.2	2.6
	70 V	19.4	13.9	62.5	4.2
	120 V	4.5	4.4	83.4	7.7
$1s\rightarrow3s\sigma$ 406.15 eV	Suzuki and Saito	1.6	2.7	75.7	20.1
	30 V	15.5	25.2	53.1	6.2
	70 V	15.9	7.0	68.9	8.2
	120 V	1.35	4.9	83.5	10.3
$1s\rightarrow3p\pi$ 408.2 eV	Suzuki and Saito	0.9	1.9	78.6	18.5
	30 V	11.0	15.5	65.3	8.4
	70 V	2.1	5.3	84.2	8.2
	120 V	0.2	1.4	88.3	10.1
$1s^{-1}$ 418 eV	Suzuki and Saito	0.5	5.2	72.0	20.0
	Eberhardt et. al.	0.5	78.5		21.0
	30 V	8.3	24.4	58.7	8.6
	70 V	3.1	17.3	68.3	11.3
	120 V	0.3	2.76	85.9	12.2

Table 3.5 Branching ratios at selected energies
a. Suzuki and Saito, Ref. 12.
b. Eberhardt et. al., Ref. 7.

electrons using a reflection analyzer found the branching ratios to be 67 for N^+, 0 for N^{+2}, 25 for N_2^+, and 8 for N_2^{+2} at the π^* resonance and 81 for N^+, 0 for N^{+2}, 4 for N_2^+, and 14 for N_2^{+2} at the 1s ionization threshold.[16] These results are very like ours

for 30 V extraction, and probably result from an incomplete collection of high kinetic energy ions. The maximum in their spectrum is at 1.8 eV. With the apparatus used in these studies, accurate branching ratios are not possible, but trends can be determined.

Conclusions

Using the kinetic energy distributions of N^+ and N^{+2}, it was possible to discern some characteristics of the dissociative surfaces accessed after core-excitation or ionization. In particular, at the $3s\sigma$ possible participant Auger decay to the inner valence hole state $3\sigma_g^{-1}\ ^2\Sigma_g^+$ was seen, as were very high kinetic energy N^{+2} ions, which most likely are from a highly excited N_2^{+3} dissociative state. In general, the previous results of Eberhardt et. al. and Suzuki and Saito were confirmed. The vibrationally resolved kinetic energy distributions showed no evidence of vibrational energy going to dissociation energy at the $1s\rightarrow\pi^*$ transition.

Chapter 4 Photodissociation of C_2H_4

The core-level absorption of ethylene has recently been the subject of several experimental and theoretical studies. Ma et.al.[1] studied the vibrational structure of the $1s\rightarrow\pi^*$ transition, and found that the frequencies do not correspond to totally symmetric vibrations. Strong excitations to nontotally symmetric modes are observed usually when the molecule's symmetry is lowered. In the first theoretical study of lowered symmetry on core-excitation, Domcke and Cederbaum[2] observed the vibronic effects in the O1s spectrum of CO_2, but their results are quite general, and really are the result of the Jahn-Teller effect. For symmetric molecules containing two equivalent atoms, the molecular core-orbitals are formed from orbitals on these atoms by symmetric ($1a_g$, for C_2H_4) and antisymmetric ($1b_{3u}$) linear combinations. Selection rules determine which of these should be the originating orbital. For example, since the ground state of C_2H_4 is ^1A_g, the allowed $C1s\rightarrow\pi^*$ transition is $^1B_{1u}$ ($1b_{3u}\rightarrow 1b_{2g}$), where $1b_{2g}$ is the π^* orbital. In D_{2h} symmetry the $^1B_{2g}$ ($1a_g\rightarrow 1b_{2g}$) transition is not allowed. However, because of the near degeneracy of these transitions (they differ by 0.02 eV)[3], they can be coupled and mixed by nontotally symmetric vibrational modes. This effect has been calculated for the first $1s\rightarrow\pi^*$ transition of ethylene.[3] In this case ν_{11} and ν_{12} (B_{3u} symmetry) are the modes which couple the two transitions. The resulting spectrum is very complex, containing twelve intense transitions involving symmetric modes ν_1 and ν_2, the ν_{11}

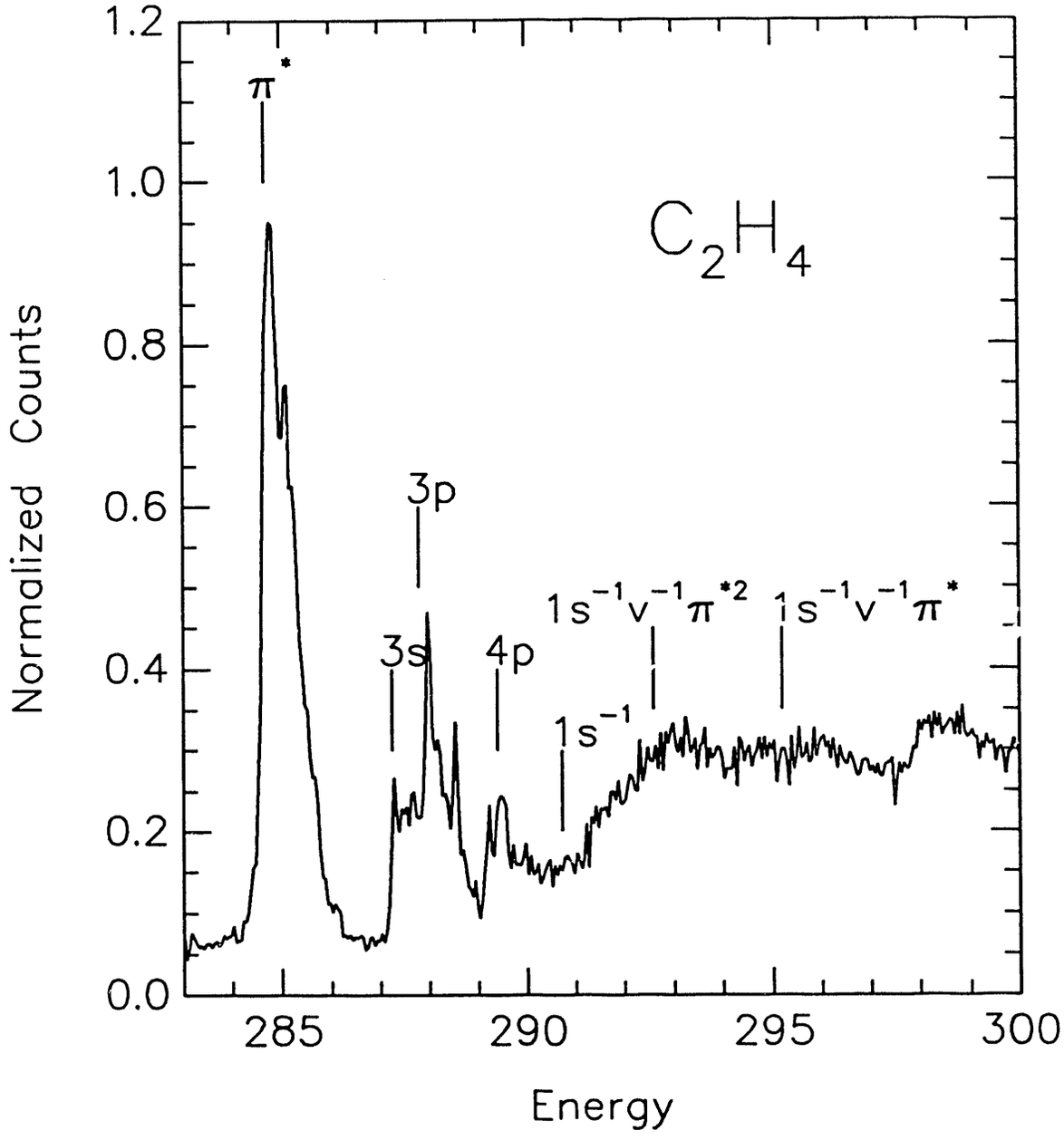

FIGURE 4.1 Total ion yield as a function of light energy for C_2H_4 near the C-1s ionization threshold.

mode and the torsional mode ν_4, and many more weaker transitions. Figure 4.1 shows the total ion yield of C_2H_4 across the $1s^{-1}$ ionization threshold. The $1s \rightarrow \pi^*$ transition looks like two asymmetric peaks, which are separated by approximately the ν_1 (C-H stretch) frequency. Gadea et. al.[3] calculated the vibronic spectrum of this transition assuming the $^1B_{1u}$ and $^1B_{2g}$ transitions are the same energy and obtained good agreement with the experimental results.

The other transitions below the 1s ionization threshold have been assigned to the Rydberg states indicated on the figure. For core-level transitions, the distinction between Rydberg orbitals and the $b_{2g}(\pi^*)$ is much greater than for valence electron transitions. The term value for the $1s \rightarrow \pi^*$ transition is 6.3 eV and for the $1s \rightarrow 3s$ transition is 2.8 eV. For the $\pi \rightarrow \pi^*$ transition the term value is only 2.9, and the $\pi \rightarrow 3s$ term value is 3.4 eV.[4] Therefore for the valence $\pi \rightarrow \pi^*$ transition the excited electronic orbital experiences considerable mixing with the Rydberg $3d\pi$ state. The reason the term values can change so dramatically between core and valence excitation has been termed antishielding. Core-electrons provide more effective shielding of the excited electrons from the nucleus, and excitation from core levels generally increases the term values by increasing the effective charge. However, it can be seen from the example mentioned above that the spatial distribution of the orbitals involved is also very important, since the term value for the π^* orbital increases by 3.4 eV, and the 3s decreases 0.5 eV between core and valence excitation. Even with valence excitation, however, the π^* orbital behaves very much like a molecular orbital particularly in condensed phases.[4]

The relaxation and dissociation of core-excited or ionized ethylene has not been studied as thoroughly as N_2. However, the electron impact Auger spectrum has been measured,[5] and the spectrum has been compared to calculations which used a typical solid state procedure,[6] a self-fold of the one-electron density of states. Their results for

the different binding energies are listed in Table 4.1. The energy values were taken form the peak maxima of figure 8 ref. 6. Those corresponding to an initial highly excited neutral were corrected for the $1s \rightarrow \pi^*$ and $1s^{-1}$ energy difference. Only for the lowest

Energy (eV)[a]	Assignment	Energy (eV)[b]	Assignment[c]	Energy (eV)[b]	Assignment[c]
10.51	**X** $^2B_{3u}$	18	ke-vve	33	k-vv
12.85	**A** $^2B_{2g}$	22		38	
14.7	**B** $^2A_{1g}$	27		41	
15.87	**C** $^2B_{2u}$	31		46	
19.1	**D** $^2B_{1u}$	36		48	
		40		53	
		44		57	

Table 4.1 Singly(**X-D**, ke-evv) and Doubly (k-vv) Charged Dissociating States
a. Brundel et. al. Ref. 7.
b. Rye et. al. Ref. 5.
c. Hutson and Ramaker Ref. 6.

lying single valence hole states are the symmetries and exact energies known from PES[7] measurements. As for the dissociation, this has been studied for the five lowest energy singly ionized states. The X-state cannot dissociate and therefore produces only $C_2H_4^+$.[8] The energy for $C_2H_4^+ \rightarrow C_2H_2^+ + H_2$ is 13.2 eV, which is in the middle of the Franck-Condon envelope for the A-state. At this energy $C_2H_4^+$ is no longer present. 13.6 eV is the threshold for $C_2H_4^+ \rightarrow C_2H_3^+ + H$, which slowly increases and is the dominant decay channel for the C-state and the D-state. At 17.7 eV, $C_2H_4^+ \rightarrow C_2H_2^+ + 2H$, and consequently the intensity of $C_2H_2^+$ increases again and is the dominant ionic product for the state at 19.1 eV binding energy. However, at 17.4 eV the $C_2H_4^+ \rightarrow CH_2^+ + CH_2$ channel is accessible, and CH_2^+ is also present at the 19.1 eV state. These should be the decay channels for the core-excited states, which relax by participant Auger decay. However, the spectator states also listed in Table 4.1 have

many more decay channels available. There are more than forty possible fragmentation channels for the the singly charged ion with the fragments in their ground electronic states. Ibuki et. al.[9] measured the photoionization of ethylene from 10.5 to 80.0 eV using an electron coincidence technique. They found the onset of H^+ at 20.5 eV, H_2^+ at 25.5 eV, C_2H^+ at 22.0 eV, C_2^+ at 28.0 eV, CH^+ at 22.5 eV, and C^+ at 26.5 eV. The branching ratios at 80 eV showed $C_2H_2^+$ to be most intense at 24.84%, followed by $C_2H_4^+$ (19.07%), $C_2H_3^+$ (17.71 eV), H^+ (12.79%), CH_2^+ (10.90%), C_2H^+ (5.48%), CH^+ (3.75%), C^+ (2.29%), and C_2^+ (1.55%).

For the fragmentation of the doubly charged ion there are at least forty-three channels with ground electronic states and singly charged fragments and twenty-three for the triply charged fragments under the same conditions. Many of these channels are accessible, as can be seen in figure 4.2, the time-of-flight spectrum of C_2H_4 at 284.7 eV light energy with the different mass to change ratios indicated on the figure. Clearly the group of peaks with 8 to 9 μsec flight time correspond to ions with two carbons and zero through four hydrogens attached. These are all narrow, well separated peaks. This is expected, since the hydrogens will carry away almost all of the kinetic energy. It is not completely apparent in this figure, but the width of these peaks decreases with increasing mass to charge ratios. However, the peaks in the mass to charge ratio region of twelve to fourteen reveal much more kinetic energy broadening. There is also a peak at mass to charge fourteen, which is very narrow, and this is assigned to a quasi-stable (at least 10 μsec lifetime) state of $C_2H_4^{+2}$. Also present are the very large H^+ peak and a small H_2^+ peak.

Energy Dependence

As with N_2, the intensities of different ions were measured as functions of incident light energy. Because there are eleven different ions in the time-of-flight

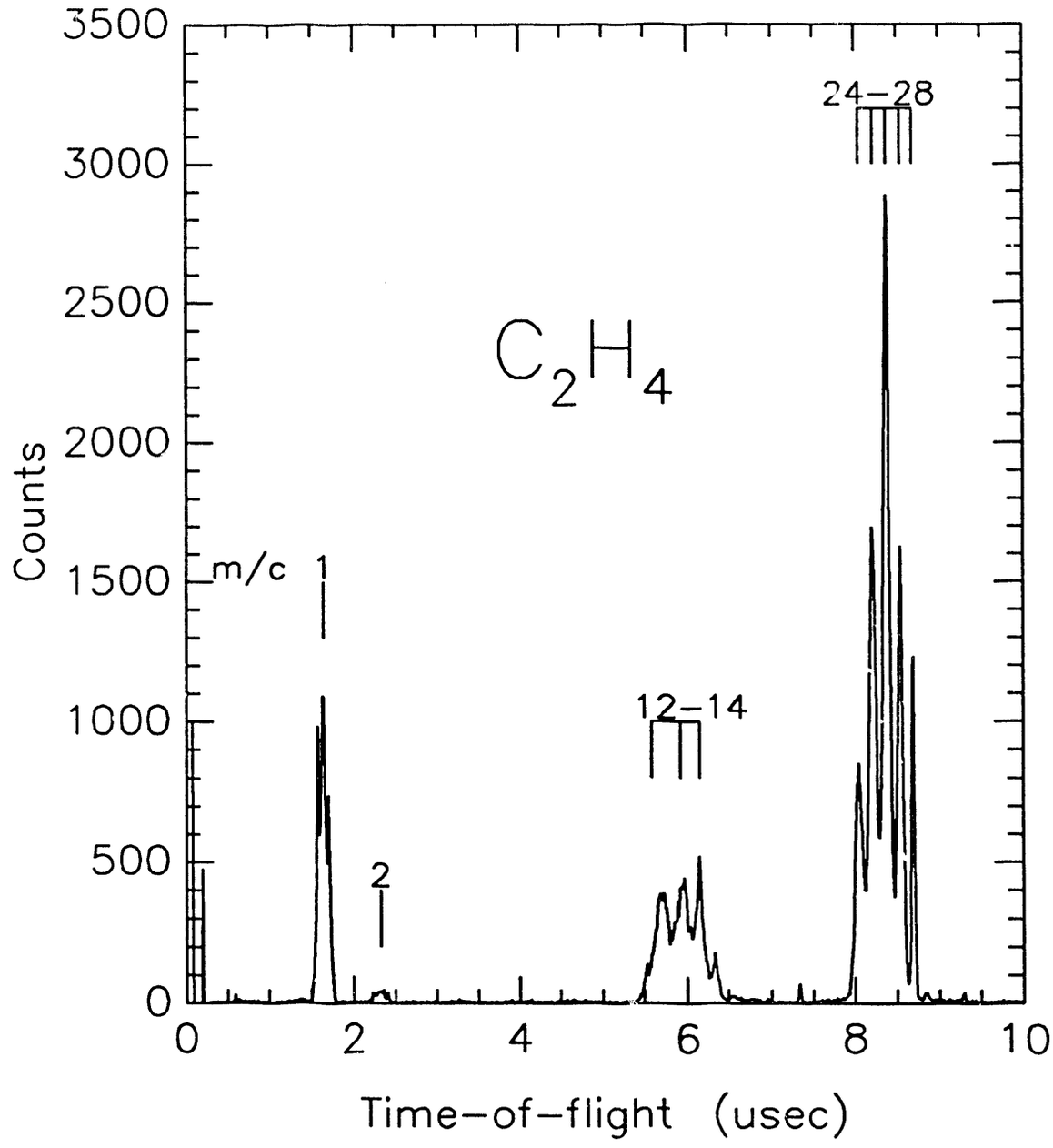

FIGURE 4.2 Time-of-flight of positive ions at 284.7 eV light energy.

spectrum and not all of them are well separated from the others some of them were measured in groups. Figure 4.3 shows the results using 30 V extraction field, since this was the best statistical set over the entire energy range. The $C_2H_n^+$ yield looked the same for both this extraction field and a higher, 120 V, field, as is expected for fragments without significant kinetic energy. For all the other fragments, their intensities above the threshold are enhanced in the higher extraction field relative to those in the lower extraction field. The asymmetry parameter for C_2H_4 C $1s^{-1}$ photoelectron has been measured by Piancastelli et. al.,[10] and it was found to increase from 0.5 at 297 eV light energy to 2.0 at 330 eV. Higher asymmetry parameters increase the relative yield at 90° when the angular acceptance is large, which in this case is the high field scan. Therefore this change in the relative intensity is probably because of changes in the asymmetry parameter. Below the ionization threshold, there appeared to be no difference between the high and low extraction field spectra.

As can be seen in figure 4.3, $C_2H_4^+$ is present not only at the $1s\rightarrow\pi^*$ transition, but also for the first few peaks in the Rydberg series. This means that $1s\rightarrow3s$ and $1s\rightarrow3p$ Rydberg transitions must relax partially by participant Auger decay. This implies that they are not completely Rydberg-like but also have some valence orbital character. They are not, however, nearly as intense relative to the $1s\rightarrow\pi^*$ as the total ion yield or the absorption spectrum, because they probably still have a much larger spatial extent than a typical valence orbital. Comparing this system with N_2 makes the mixed nature of these orbitals much more evident. The difference in the term values between the π^* orbital and the 3s orbitals for N_2 is 5.6 eV, and none of the Rydberg states relaxed to N_2^+, whereas for C_2H_4 the term value difference is only 2.6 eV, and $C_2H_4^+$ is enhanced slightly on the first two series members.

All other expected mass to charge ratios appear throughout the $1s^{-1}$ energy range. The CH_n^+ energy dependence looks almost exactly like that of H^+, while the

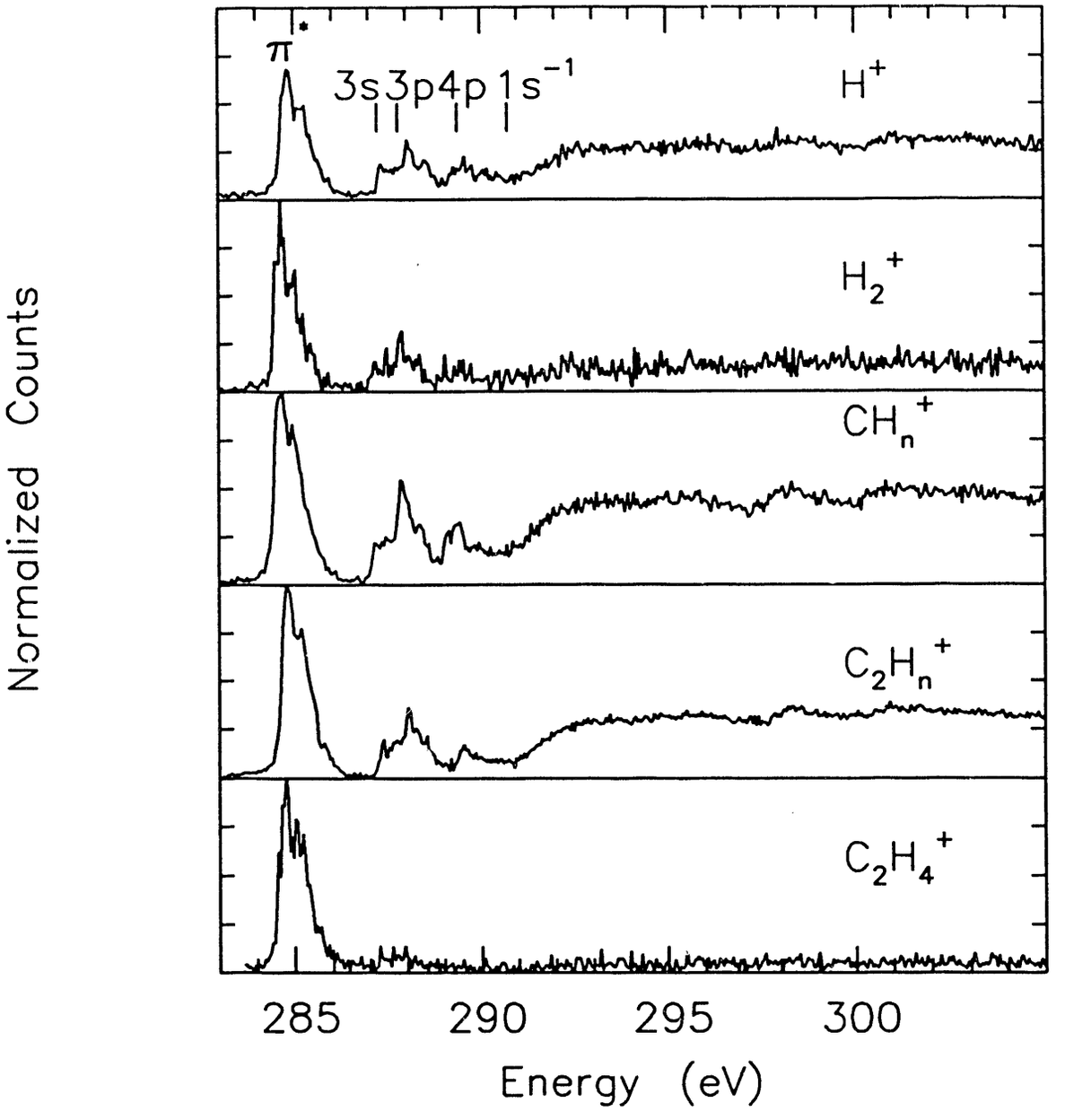

FIGURE 4.3 Normalized intensity of ions as a function of light energy with 30 V extraction field.

$C_2H_n^+$ intensity is much lower above threshold relative to the $1s\rightarrow\pi^*$ transition than either H^+ or CH_n^+. This is most likely because above threshold most of the final states are double ions. A single absorption event cannot create two ions of $C_2H_n^+$, but it can easily create two ions of CH_n^+ and H^+. The difference between the CH_n^+ and $C_2H_n^+$ energy dependences appears, however, to be a uniform intensity decrease after the $1s\rightarrow\pi^*$ transition, and the decrease in intensity at the high energy part of the spectrum appears to have the same slope. Unfortunately, because the H_2^+ fragment has very little intensity over the entire energy range, the signal to noise ratio is not very good for this fragment, but it appears to have roughly the same energy dependence as the other ionic fragments.

Figure 4.4 shows the energy dependence for the three most abundant ionic fragments with better resolution below the 1s ionization threshold. It can be seen more clearly in this figure that these three fragments have very similar spectra across the $1s\rightarrow\pi^*$ transition, and like N_2 there is probably not much change in the photofragmentation for transitions to different vibrational levels of the same electronic state.

The major fragmentation products at the $1s\rightarrow\pi^*$ transition are the $C_2H_n^+$ ions, but both the H+ and CH_n^+ intensities are increased relative to $1s\rightarrow\pi^*$ transition on the Rydberg series, and by comparing the $1s\rightarrow4p$ intensity with the lower members of the series they also appear to increase through the Rydberg series. Some of this could arise from differences in the angular distribution, but it is most likely also from the increase in relaxation by double Auger transitions for higher n members of the Rydberg series, previously observed for N_2. Above the double ionization threshold all the fragments which are more likely to be the products of dissociation from doubly charged states are also enhanced.

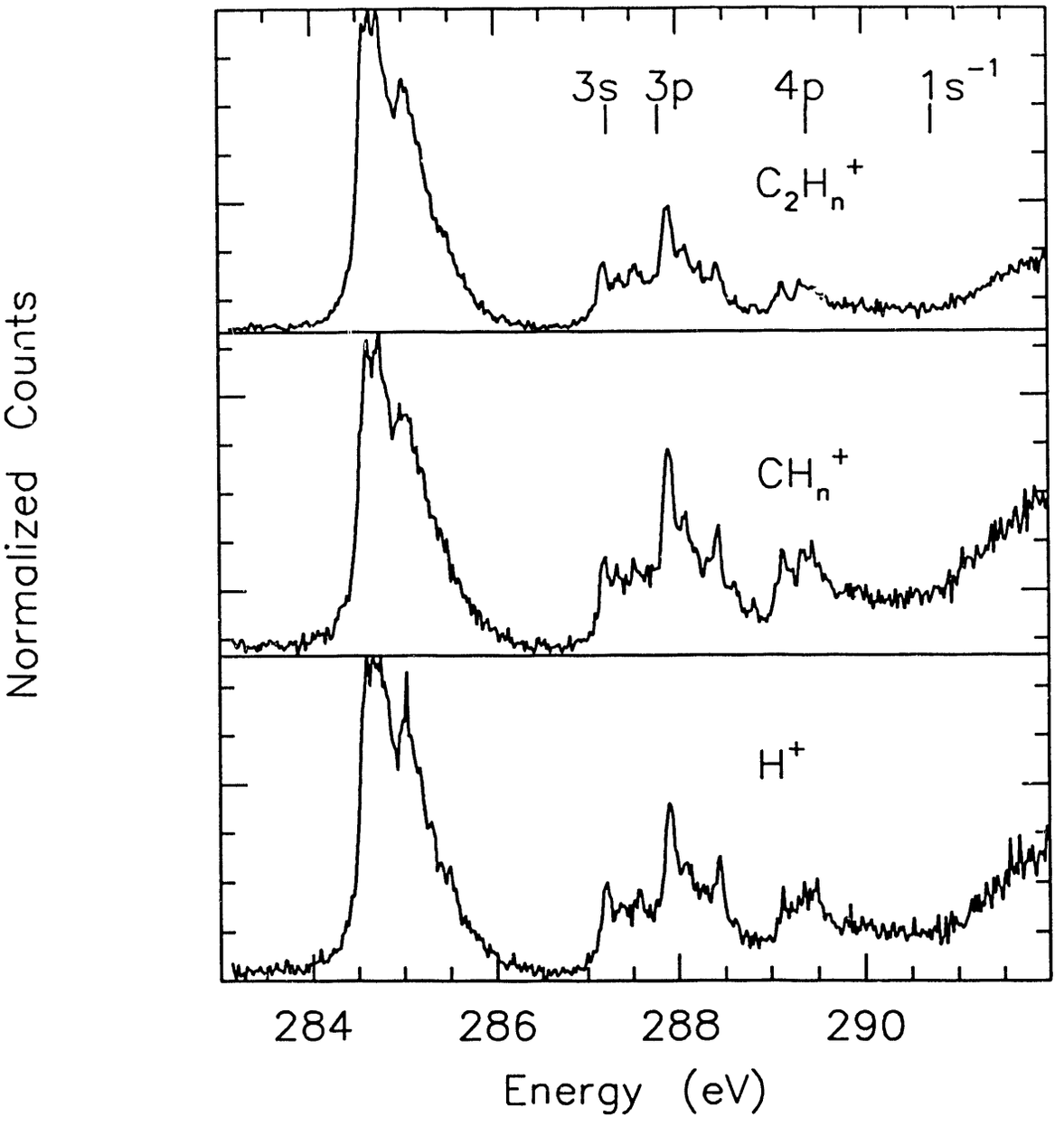

FIGURE 4.4 Normalized intensity of ions as a function of light energy with 120 V extraction field.

Branching Ratios

More details about the dissociation process can be determined from the branching ratios and the kinetic energy released during dissociation. These were measured at 90° relative to the polarization vector and with two different extraction fields applied to the analyzer. Because not all of the ions with high kinetic energy were collected, especially H^+, the results are biased toward fragments with less kinetic energy, generally the ions with a high mass to charge ratio. The asymmetry parameter also affects the results. For ions with only thermal kinetic energy, there is no angular information in the different spectra, but those with greater kinetic energy have a different acceptance angle for different fields. At 90° relative to the polarization vector, fragments with the asymmetry parameter equal to minus one are at a maximum, and those with $\beta = 2$ are at a minimum. Therefore the branching ratios determined with a weak extraction field will be enhanced for fragments with greater than thermal kinetic energy on transitions with higher asymmetry parameters, compared to the branching ratios obtained with a higher extraction field. Lower extraction fields are, however, useful for separating fragments into components with different kinetic energies.

Figure 4.5 shows the branching ratios for the $C_2H_n^+$ fragments with 120 V extraction field. The statistical uncertainty is on the order of the symbol size. Systematic errors from the analyzer transmission are probably much larger. However, since the mass to charge ratios of all of these fragments are very similar, and the other fragments of dissociation are mass one or two, the systematic errors should be the same for the ions in the figure. The first point was taken off resonance at 260 eV. The branching ratios here differ considerably from those of Ibuki et. al. at 80.0 eV. They are, however, consistent with the trends of their data, since the $C_2H_2^+$, $C_2H_3^+$, and $C_2H_4^+$ branching

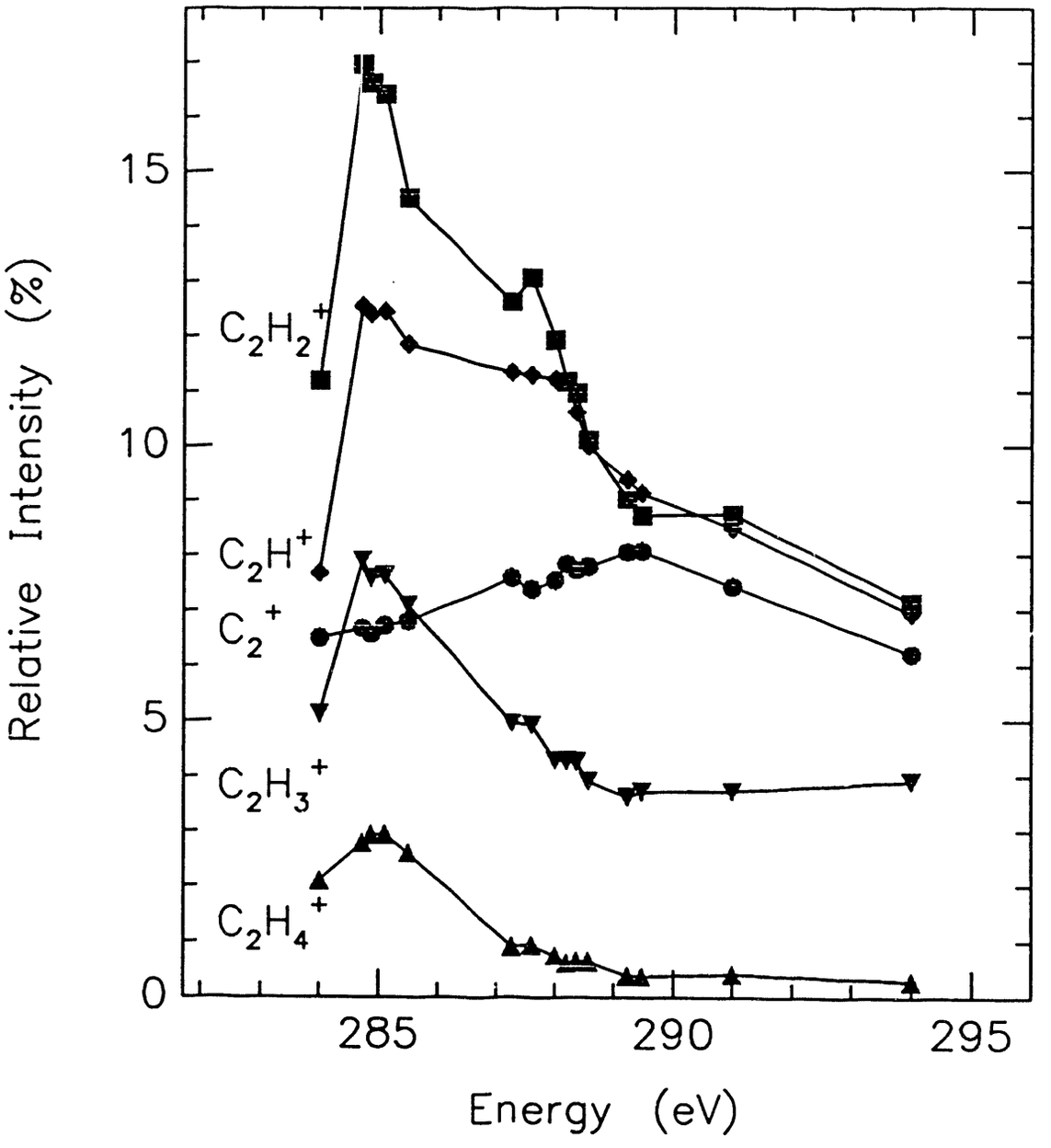

FIGURE 4.5 Branching ratios for $C_2H_n^+$ ions determined from 120 V extraction field time-of-flight spectra. Lowest Energy points were taken at 260 eV and the highest energy points were taken at 330 eV, but have been shifted to 284 eV and 294 eV respectively.

ratios were decreasing , and C_2H^+, C_2^+, H^+ , and CH_n^+ were all increasing, with increasing energy.

As the energy dependence data showed $C_2H_4^+$ has significant intensity only on the π^* resonance and the first few peaks of the Rydberg series. $C_2H_2^+$ is the most abundant fragment, with resonant enhancement on the π^* resonance and the low energy Rydberg states. This enhancement on the π^* resonance is approximately 50% of the branching ratio below the C $1s^{-1}$ structure. After the first few Rydberg peaks, the branching ratio of this ion rapidly becomes smaller than it was below the C $1s^{-1}$ structure. This same behavior is seen for $C_2H_4^+$ and $C_2H_3^+$, with the exception that by the Rydberg series they are already less intense than before the C $1s^{-1}$ pre-edge structure. C_2H^+ behaves slightly differently. It is more enhanced on the first few Rydberg peaks relative to its intensity at the $1s\rightarrow\pi^*$ transition, and its branching ratio above the 1s ionization threshold is not less than it is below the $1s\rightarrow\pi^*$ transition. Whereas C_2^+ is not resonantly enhanced , but appears to increase very slightly over the Rydberg series.

It is known from the results of Stockbauer and Inghram[8] that $C_2H_4^+$, $C_2H_3^+$, and, $C_2H_2^+$ are the products of single valence hole states. $C_2H_3^+$ and $C_2H_2^+$ can also be the products of double valence hole states, and this is the reason for their appreciable intensity above the 1s ionization threshold. C_2H^+, since it is enhanced on the $1s\rightarrow\pi^*$ transition but is not a known dissociation product of a single valence hole state, is probably a primary dissociation product of an important spectator Auger state. This state may correspond to the E-state, a known satellite, at which C_2H^+ is found with valence dissociation.[9] The greater enhancement of this state for the first few members of the Rydberg series compared to that of $C_2H_2^+$ and $C_2H_3^+$ lends some support to this assignment, since these orbitals are still more Rydberg-like in character than valence-like and therefore should have a higher percentage of Auger decay through the spectator

channels. C_2^+ does not appear to increase at the $1s\rightarrow\pi^*$ transition. Since it does not decrease relative to its below resonance value, it too must be at least in part a product of spectator Auger decay.

Figure 4.6 shows the branching ratios of the CH_n^+ fragments at high extraction field. The energy dependence data showed these fragments to be enhanced at the $1s\rightarrow\pi^*$ transition. However, it is clear from the branching ratios that at this transition the $C_2H_n^+$ ions are more greatly enhanced. This at first seems counter-intuitive, since the geometry of the $1s\rightarrow\pi^*$ state has an increased C-C bond length, a localized core-hole, and a decreased C-H bond length at the localized core-hole. However, just as N_2 excited to the $1s^{-1}\pi^*$ state does not evolve on that state before Auger decay, the $1s^{-1}\pi^*$ state of C_2H_4 behaves like a virtual state, and the Franck-Condon overlap between the ground state and the dissociative singly ionized state is what is important for dissociation. The excited states of the single ion reached by spectator decay of the $1s^{-1}\pi^*$ state also must prefer to dissociate by breaking hydrogen bonds, since participant Auger decay has been calculated to be about 13% of the total Auger intensity for the $1s\rightarrow\pi^*$ transition, and the $C_2H_n^+$ ions are approximately 40% of the total ion intensity.

CH_2^+ appears to have a maximum relative intensity at the $1s\rightarrow4p$ transition, while CH^+ is most intense just at the ionization threshold and C^+ is maximized at the highest energy. The only other ion which continues increasing in relative intensity with increased energy is the other atomic ion, H^+. Since the highest measured energy points were at 330 eV, which is above the energy for core plus valence ionization, this could mean that the resulting triply ionized states favor these dissociative states. As could be seen in figure 4.2, however, these ions possess significant kinetic energy, and therefore they were also measured with a low extraction field in an attempt to separate fragments with different kinetic energies. Figure 4.7 shows the mass to charge region for CH_n^+ ions at 120 V extraction field and at 30 V extraction field for the same incident light

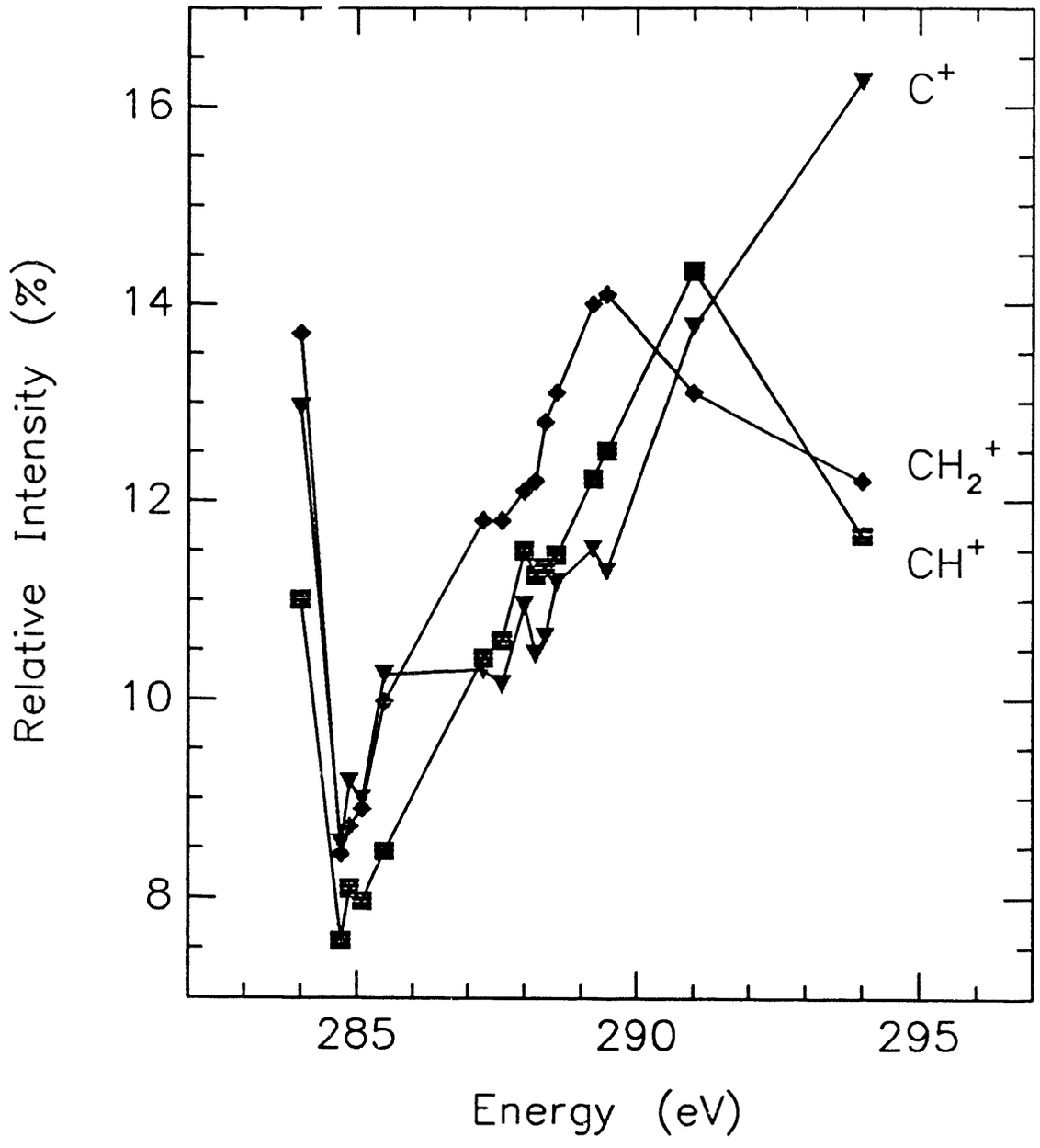

FIGURE 4.6 Branching ratios for CH_n^+ ions determined from 120 V extraction field time-of-flight spectra. Lowest Energy points were taken at 260 eV and the highest energy points were taken at 330 eV, but have been shifted to 284 eV and 294 eV respectively.

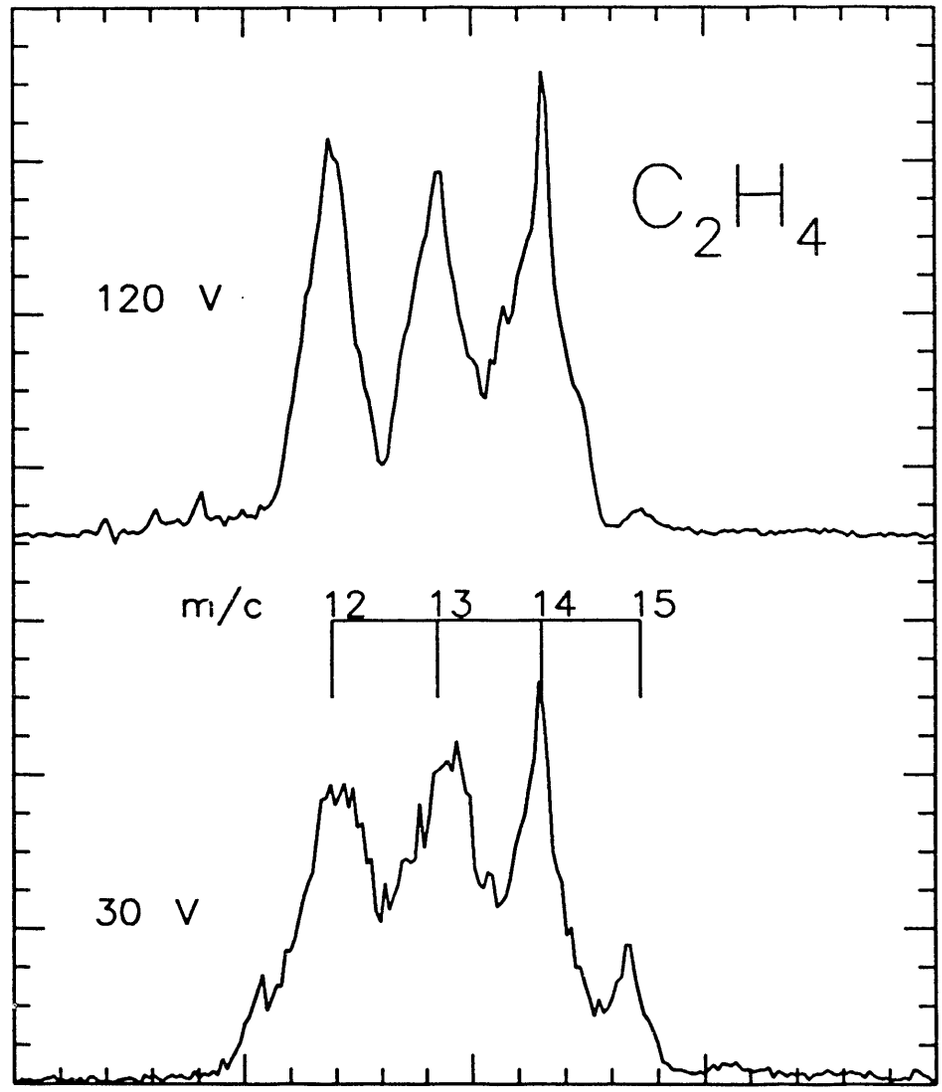

FIGURE 4.7: Comparison of time-of-flight spectra taken with 30 V extraciton field and 120 V extraction field for ions with mass to charge ratios of 12-14.

energy. From the figure, it is clear that higher extraction field separates the different masses more effectively, but low field emphasizes the kinetic energy distribution, since the 30 V spectrum appears to have a peak at mass to charge 15 but the 120 V spectrum shows that most of this is high kinetic energy mass to charge 14. Therefore the low field results were used to determine the primary kinetic energy of the fragments. Table 4.2 shows the primary values of kinetic energy for the different fragments determined form the low field data. Using the kinetic energies of the fragments it is possible to make tentative assignments of the dissociation

Fragment	Kinetic Energy $1s\rightarrow\pi^*$	Kinetic Energy $1s^{-1}$
C_2H^+	4.5 eV	4.5 eV
C_2^+	4.0 eV	4.0 eV
H_2^+	5.5 eV	5.5 eV
H^+	6.0 eV	7.0 eV

Table 4.2 Measured Kinetic Energies of Major Fragments

fragments of some of the Auger states. Some assumptions are necessary to make these assignments. First the total charge has to be assumed. For the $1s\rightarrow\pi^*$ transition it is assumed that this is one, and above the ionization threshold it is assumed to be two. Since this neglects the role of double Auger decay, which was shown to be important for N_2, this is only an approximation. Also it is necessary to assume a distribution of excess energy. Since there are so many dissociative states, the possible assignments are limited to ground electronic states of the fragments. The vibrational energy remaining in the molecular fragments is assumed to be negligible. The first few dissociative states with a total charge of one are listed in table 4.3 with their thermodynamic energies.[11]

Conservation of momentum determines the sharing of energy among the various fragments. For the participant decay states at the $1s\rightarrow\pi^*$ transition, which are the

valence states, the dissociation products are known, states 1-3, 5, and 7 in table 4.3. States 4 and 6 are not mentioned in reference 6 or 9, but they are energetically accessible

	$C_2H_n^+$	Energy[a]		CH_n^+	Energy[a]
1	$C_2H_4^+$	10.5 eV	5	$CH_2^+ + CH_2$	17.4 eV
2	$C_2H_2^+ + H_2$	13.2 eV	12	$CH_2^+ + C + H_2$	21.1 eV
3	$C_2H_3^+ + H$	13.4 eV	13	$CH_2 + C^+ + H_2$	22.0 eV
7	$C_2H_2^+ + 2H$	17.7 eV	14	$CH_2^+ + CH + H$	22.0 eV
8	$C_2H^+ + H_2 + H$	18.9 eV	16	$CH_2 + CH^+ + H$	22.7 eV
10	$C_2^+ + 2H_2$	20.0 eV	17	$CH^+ + CH + H_2$	22.9 eV
19	$C_2H^+ + 3H$	23.4 eV	23	$CH_2^+ + C + 2H$	25.6 eV
20	$C_2^+ + H_2 + 2H$	24.6 eV	24	$C^+ + C + 2H_2$	25.7 eV
33	$C_2^+ + 4H$	29.1 eV	27	$CH_2 + C^+ + 2H$	26.5 eV
			28	$CH^+ + C + H_2 + H$	26.5 eV
			30	$CH^+ + CH + 2H$	27.4 eV
			36	$C^+ + C + H_2 + 2H$	30.2 eV
			38	$CH^+ + C + 3H$	31.0 eV
			41	$C^+ + C + 4H$	34.7 eV
	H^+	Energy[a]		H_2^+	Energy[a]
6	$H^+ + C_2H_3$	17.6 eV	4	$H_2^+ + C_2H_2$	17.2 eV
9	$H^+ + C_2H_2 + H$	19.9 eV	15	$H_2^+ + C_2H + H$	22.6 eV
11	$H^+ + C_2H + H_2$	20.8 eV	18	$H_2^+ + C_2 + H_2$	23.4 eV
21	$H^+ + CH_2 + CH$	25.2 eV	25	$H_2^+ + CH_2 + C$	26.1 eV
22	$H^+ + C_2H + 2H$	25.3 eV	29	$H_2^+ + 2CH$	27.2 eV
26	$H^+ + C_2 + H_2 + H$	26.2 eV	31	$H_2^+ + C_2 + 2H$	28.0 eV
32	$H^+ + CH_2 + C + H$	28.8 eV	34	$H_2^+ + 2C + H_2$	29.8 eV
35	$H^+ + 2CH + H$	29.9 eV	40	$H_2^+ + 2C + 2H$	34.3 eV
37	$H^+ + C_2 + 3H$	30.7 eV			
39	$H^+ + 2C + H_2 + H$	32.5 eV			
42	$H^+ + 2C + 3H$	37.0 eV			

Table 4.3 Thermodynamic Energies for Fragments
a. Ref. 11.

for the D-state at 19.1 eV. They did not see any H^+ until they passed the appearance potential of state 11, 20.8 eV, and H_2^+ at state 25, 26.2 eV. Ions from states 4 and 6

could be present in this experiment, but they do not produce a discernible peak at the correct kinetic energy. The first spectator state at 18.2 has these same states available to it, but the kinetic energy of the fragments should be even less.

The next and most intense spectator state occurs at 21.9 eV binding energy, so five more dissociative channels are open, including $C_2H^+ + H_2 + H$ and $C_2^+ + 2H_2$. Since C_2H^+ appears to be enhanced on spectator states, it is probably a major decay product of this state. Another intense spectator peak appears at 26.7 eV. The energetic CH_2^+ fragment has approximately 4.5 eV kinetic energy, adding the total kinetic energy of the fragments of state 5 in table 4.3 to its binding energy gives 26.4 eV total energy. Therefore the energetic CH_2^+ fragments may come from this spectator state. There is also some evidence for this in the work of Ibuki et. al. There are now, however, seventeen more dissociative channels open. Energetic H^+ could come from the next spectator state at 31 eV binding energy. $C_2H_2 + H + H^+$ has a binding energy of 19.9 eV. If it dissociates

symmetrically the H^+ fragment should have about 5 eV kinetic energy, while the energetic H^+ has 5.5 ± 1.0 eV. The 5.0 ± 1.0 eV kinetic energy H_2^+ could result from the 36 eV spectator state dissociating to $C_2 + H_2 + H_2^+$ which has 23.4 eV binding energy.

The first few doubly ionized dissociative states are listed in table 4.4, and these are the fragments from dissociation of the k-vv states in table 4.1. Energetic H^+ could result

from the first k-vv state dissociating to $C_2H_3^+ + H^+$, since that would give H^+ with approximately 6.0 eV kinetic energy, and H^+ appears with 7.0 ± 1.0 eV kinetic energy. It is also possible the k-vv state at 46.0 eV dissociates into $C_2H_2^+ + H^+ + H$, which would give binding energy plus kinetic energy of 31.6 + 14.0 eV = 45.6 eV. The

energetic H_2^+ may result from the lowest lying dissociative state $C_2H_2^+ + H_2^+$, since binding energy plus kinetic energy would be about 35.1 eV, and the nearest k-vv state is

	$C_2H_n^+$	Energy[a]		CH_n^+	Energy[a]
1	$C_2H_4^{+2}$		3	$2CH_2^+$	27.8 eV
2	$C_2H_3^+ + H^+$	27.0 eV	6	$CH_2^+ + C^+ + H_2$	32.4 eV
4	$C_2H_2^+ + H_2^+$	28.6 eV	8	$CH_2^+ + CH^+ + H$	33.3 eV
5	$C_2H_2^+ + H^+ + H$	31.6 eV	10	$2CH^+ + H_2$	34.1 eV
7	$C_2H^+ + H^+ + H_2$	32.5 eV	13	$CH_2^+ + H^+ + CH$	35.6 eV
11	$C_2H^+ + H_2^+ + H$	34.3 eV	15	$CH^+ + H^+ + CH_2$	36.3 eV
12	$C_2^+ + H_2^+ + H_2$	35.4 eV	16	$CH_2^+ + H_2^+ + C$	36.5 eV
19	$C_2H^+ + H^+ + 2H$	37.0 eV	17	$CH_2^+ + C^+ + 2H$	36.8 eV
20	$C_2^+ + H^+ + H_2 + H$	38.1 eV	18	$2C^+ + 2H_2$	36.9 eV
27	$C_2^+ + H_2^+ + 2H$	40.0 eV	21	$CH^+ + H_2^+ + CH$	38.4 eV
			22	$2CH^+ + 2H$	38.5 eV
			29	$CH^+ + H^+ + CH + H$	41.0 eV
			30	$2C^+ + H_2 + 2H$	41.4 eV
	H^+	Energy[a]		H_2^+	Energy[a]
2	$H^+ + C_2H_3^+$	27.0 eV	4	$H_2^+ + C_2H_2^+$	28.6 eV
5	$H^+ + C_2H_2^+ + H$	31.6 eV	11	$H_2^+ + C_2H^+ + H$	34.3 eV
7	$H^+ + C_2H^+ + H_2$	32.5 eV	12	$H_2^+ + C_2^+ + H_2$	35.4 eV
9	$2H^+ + C_2H_2$	33.5 eV	14	$H_2^+ + H^+ + C_2H$	36.2 eV
13	$H^+ + CH_2^+ + CH$	35.6 eV	15	$H_2^+ + CH_2^+ + C$	27.2 eV
14	$H^+ + H_2^+ + C_2H$	36.2 eV	21	$H_2^+ + CH^+ + CH$	38.4 eV
15	$H^+ + CH^+ + CH_2$	36.3 eV	23	$2H_2^+ + C_2$	38.9 eV
19	$H^+ + C_2H^+ + 2H$	37.0 eV	27	$H_2^+ + C_2^+ + 2H$	40.0 eV
20	$H^+ + C_2^+ + H + H_2$	38.1 eV	31	$H^+ + H_2^+ + H + C_2$	41.6 eV
24	$2H^+ + C_2H^+ + H$	38.9 eV			
25	$H^+ + CH_2^+ + C + H$	37.0 eV			
26	$2H^+ + H_2 + C_2$	39.7 eV			
28	$H^+ + C^+ + CH_2 + H$	40.0 eV			
29	$H^+ + CH^+ + CH + H$	41.0 eV			

Table 4.4 Thermodynamic Energies for Fragments of Doubly Charged States
a. Ref. 11.

at 38.0 eV. The fragments would have relatively high internal energy but not enough to dissociate. With 4.5 eV kinetic energy, CH_2^+ would result from dissociation of the 38 eV Auger state into $2CH^+$ with 27.8 eV binding energy.

Conclusions

The dissociation pattern reveals that with core-excitation the 3s and 3p Rydberg orbitals show some valence character in their Auger decay through participant channels. If vibrational excitation changes the dissociation, it is too small an effect to be seen in this experiment There is also evidence of metastable $C_2H_4^{+2}$. The dissociation of the highly excited singly and doubly charged states produces a very complex dissociation spectrum. All the possible ions are present, and the smaller fragments are also present with significant kinetic energy, up to 7.0 eV for H^+ and 5.0 eV for CH_n^+. This indicates that dissociation does not always occur through nearby channels. In this case detailed knowledge of the symmetries and energies of the excited states of $C_2H_4^{+2}$ would help determine the actual relaxation channels for the specific Auger states.

Chapter 5 Photodissociation of CH_3Cl

Methyl chloride differs in many important ways from N_2 and C_2H_4. The lowest energy unoccupied molecular orbital is a σ^* and not a π^* orbital. In this case the σ^* orbital is a C-Cl antibonding orbital. Because all of the bonds have approximately the same strength, there is less chance that the molecule will preferentially break one bond over another, as C-H bond breaking is more common for C_2H_4 than C-C bond breaking. N_2 also has many single valence hole ionic states, which are stable,[1] and some known double ionic states, which are stable. Whereas ethylene is known to dissociate on all but the two lowest energy single ionic states, it has a highly structured PES spectrum,[2] and only three available dissociative states exist the for the entire valence hole region. The PES spectrum of CH_3Cl, on the other hand, shows only two almost degenerate features with vibrational structure, which correspond to ionization of the highest-lying molecular orbitals, the Cl lone pair orbitals. The energy for this transition is 11.68 eV,[3] and the energy for the first dissociation channel $CH_3Cl^+ \rightarrow CH_3^+ + Cl$ is 13.41 eV. The other singly charged states in the PES spectrum lie above this dissociative state, are extremely weak and show broadening typical of fast dissociation. An Auger spectrum taken at 201 eV[4] shows that there are excited states

of CH_3Cl^+ from 20-23.5 eV binding energy corresponding to two valence electron holes and an electron in the σ^* orbital.

Figure 5.1 shows the total ion yield from CH_3Cl across the C 1s ionization threshold. The states are labeled according to Hitchcock and Brion.[5] Unlike N_2 and C_2H_4 the first resonance does not rise from an almost zero background. The Cl 2s and 2p ionization thresholds are at 277 eV and 207 eV, respectively, and photoelectric events from these subshells contribute significantly to the absorption in this energy region, and provide the background for the C 1s spectrum. Unfortunately, it was impossible to eliminate all of the effects of carbon contamination on the grating, which causes the dip at 290.5 eV. The σ^* resonance in this spectrum is clearly more closely related to the Rydberg resonances than either the N_2 or C_2H_4 $1s\rightarrow\pi^*$ resonance. This is not an uncommon occurrence, and frequently because they are so close in energy to the Rydberg series, σ^* orbitals mix with Rydberg series.[6] Therefore the resonance is not intense relative to the Rydberg series. In the CH_3Cl Auger spectrum taken at 201 eV,[4] the $2p\rightarrow\sigma^*$ transition, Carlson et. al. found that spectator Auger decay dominated the spectrum, which is also considered evidence of Rydberg character. Then it is possible that the unique dissociation structure seen at the other core→valence transitions may not be seen for CH_3Cl.

Figure 5.2 shows the time-of-flight spectrum for the ions taken at 292.9 eV just at the C 1s ionization threshold. The CH_3Cl used in this experiment contained the naturally occurring abundances of Cl^{35} and Cl^{37}. Therefore all ions containing Cl appear as two peaks. The only peaks in these spectra which do not reveal significant kinetic energy are the CH_nCl^+ and CH_nCl^{+2} peaks. The most intense peak under those labeled CH_nCl^+ is that corresponding to $CCl,^{35+}$ and the second most intense peak is $H_2CCl.^{35+}$ All possible states are present. In the region of the spectrum labeled $ClH_n,^+$ it is not as easy to assign specific peaks. It is clear, however, that Cl^+ and HCl^+

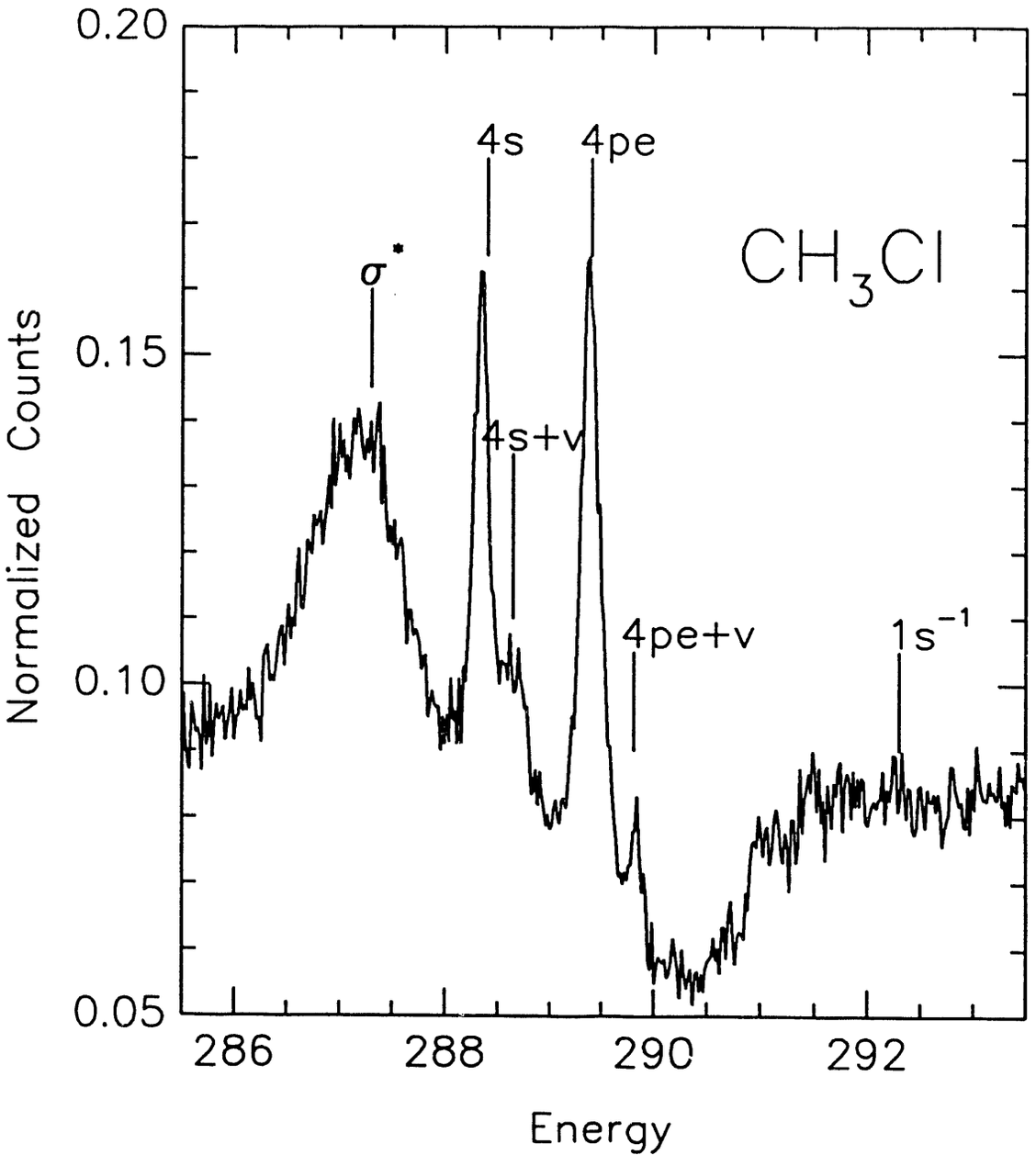

FIGURE 5.1 Normalized total ion yield as a function of light energy for CH_3Cl near the C-1s ionization threshold.

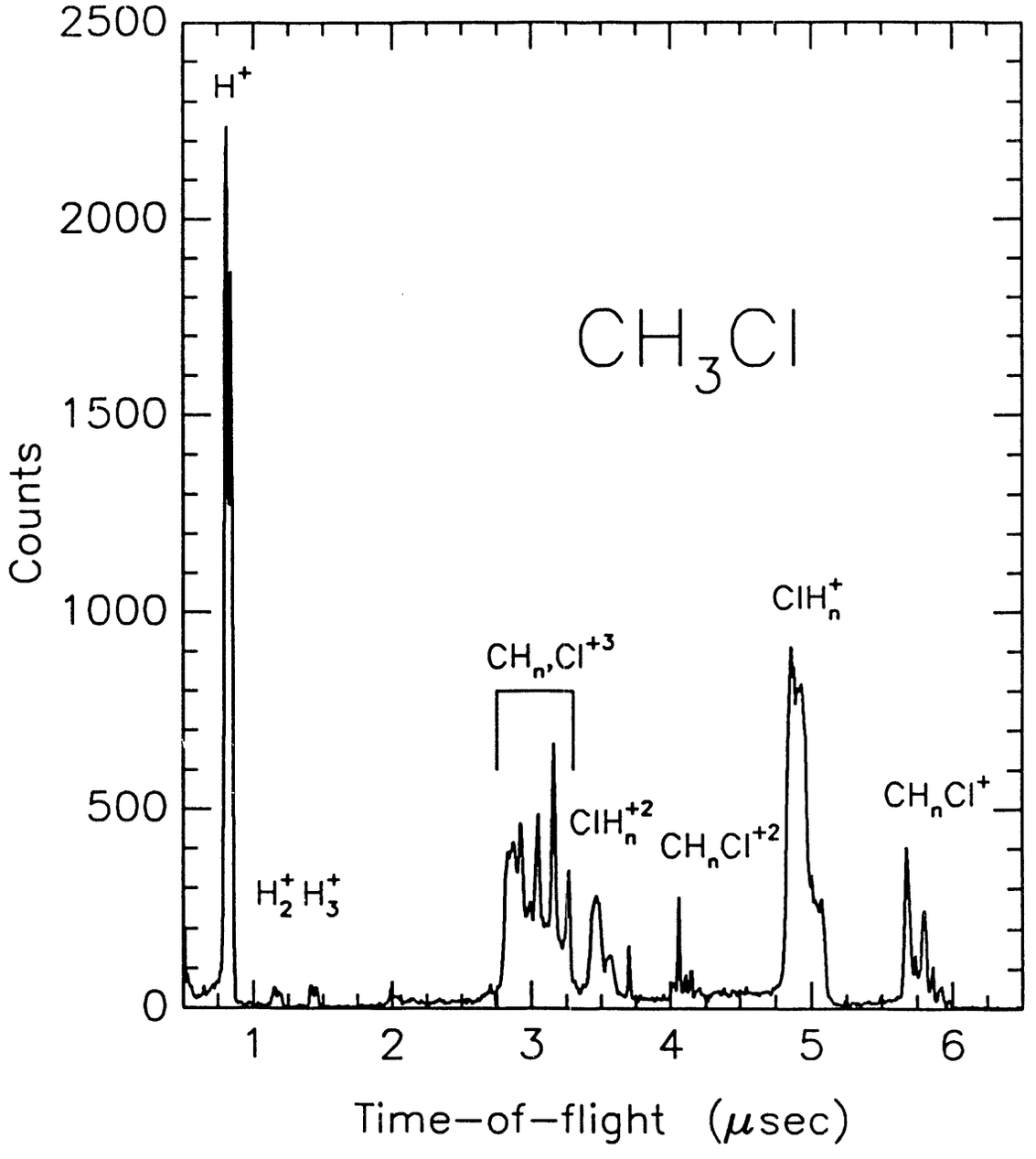

FIGURE 5.2 Time-of-flight of positive ions of CH_3Cl at 292.9 eV light energy.

are the most important species, since the intensity is limited to that time-of-flight range. Interestingly there are quasistable states of $CH_nCl.^{+2}$ The narrow peak at 3.7 μsecs time-of-flight is from Argon contamination. The group of peaks at 3.5 μsecs look similar to those at 5.0 μsecs and corresponds to $ClH_n.^{+2}$ The actual time-of-flight indicates that the majority of the intensity here is from $Cl,^{+2}$ as would be expected. The next set of peaks reveals a complex structure. This is to be expected, since CH_n^+ ions should possess various kinetic energies. H_2^+ and H_3^+ appear with small intensity and significant kinetic energy over the entire energy range, and H^+ is the second most intense peak (approximately 20%) after ClH_n^+ (approximately 30%) for the entire energy range.

Individual photodissociation spectra of CH_3Cl were collected over the entire $1s^{-1}$ excitation and ionization region. Four of these are shown in figure 5.3. It is immediately apparent from looking at these four spectra that the kinds of differences in dissociation seen between the different core level transitions in N_2 and C_2H_4 are not seen for this case. There are, however, subtle differences. The relative intensities of the CH_nCl^+ peaks change, giving more intensity above the 1s ionization threshold and on the Rydberg peak to CCl^+ and more intensity to CH_2Cl^+ on the σ^* resonance. The CH_nCl^{+2} region, however, does not show any such changes. The relative intensities here could be determined primarily by the stability of the doubly charged ions. The other difference is in the structure of the CH_n^+, Cl^{+3} region. In both the nonresonant and the $1s^{-1}$ spectra there are four sharply defined peaks, which correspond to zero kinetic energy CH_n^+. In the resonant spectra, however, the kinetic energy spread is much greater. There is also a trend toward smaller mass to charge ratio in this region as the incident energy is increased.

The overwhelming characteristic of these spectra, however, is their sameness. There are two possible reasons for this. The σ^* orbital does not have significant overlap

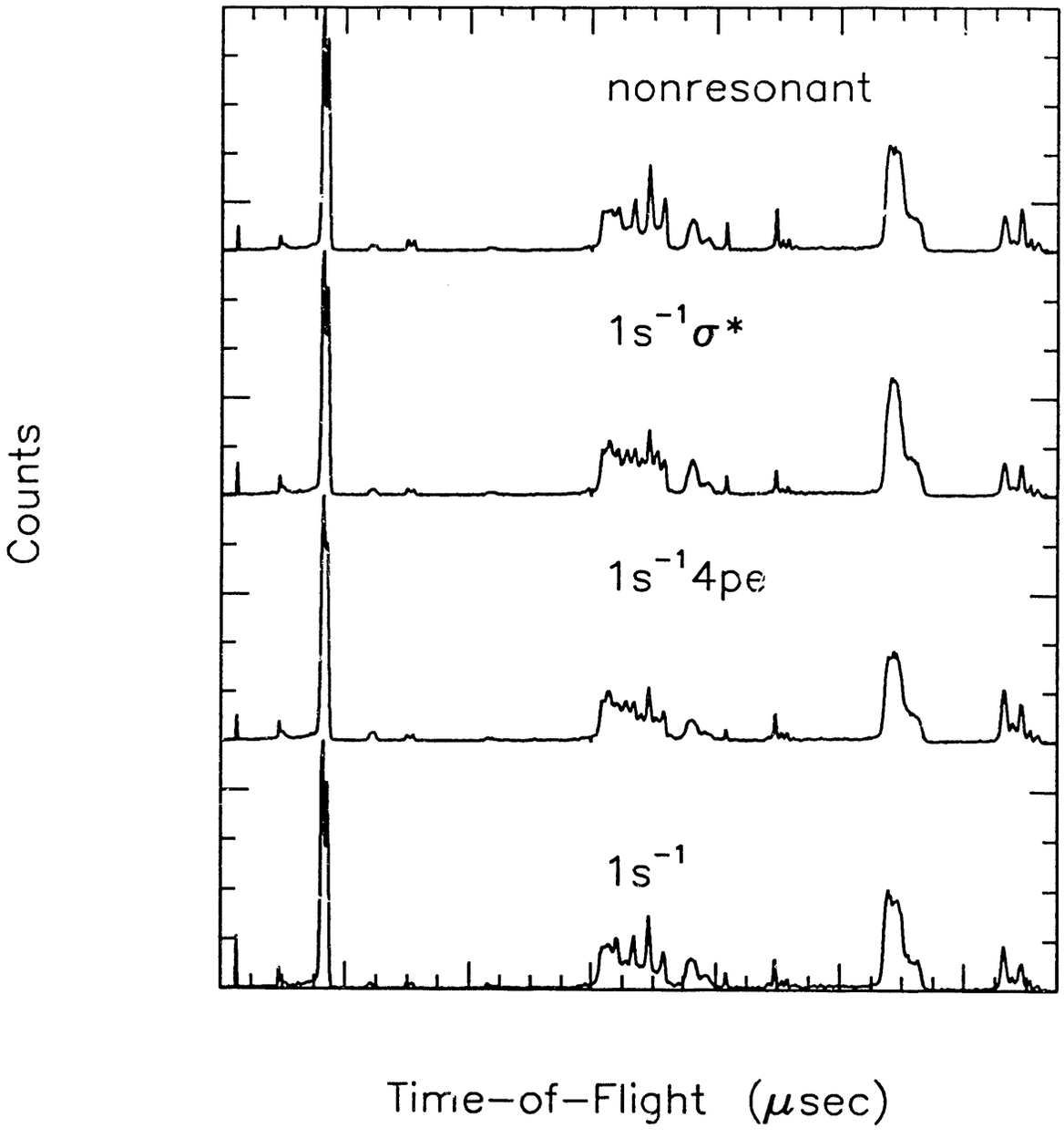

FIGURE 5.3 Normalized intensity of ions as a function of light energy with 30 V extraction field for different transitions near the C 1s ionization threshold

with the single valence hole states, and because of its Rydberg character relaxation to double hole states is more intense here than for the π^* orbitals. Also the entire C $1s^{-1}$ region sits on a background of Cl $2p^{-1}$ and $2s^{-1}$ continua, unlike N_2 and C_2H_4 where the nearest subshell was over 350 eV and 240 eV away, respectively. The increase above the background above threshold is approximately 60%. Therefore in most of the C 1s region over half the intensity is from Cl $2p^{-1}$or $2s^{-1}$ events. If this were the primary factor the 1s→4pe TOF spectrum would be the most representative of the C $1s^{-1}$ events. In fact the H_nCl^{+2} peaks are somewhat less intense, which is a naive expectation of removing more electrons from the carbon atom than the chlorine, but the differences are not very large. In conclusion, this is not a case of state-specific dissociation.

References

Part I Zero-Kinetic-Energy PES

Introduction:

1. A. Einstein, "Uber einen die Erzeugung und verwandlung des Lichtes betreffenden heuristischen Gesichtspunkt," Ann. Phys. **17**, 132 (1905).

2. D. W. Turner, C. Baker, A. D. Baker, and C. R. Brundle, *Molecular Photoelectron Spectroscopy,* John Wiley & Sons Ltd., London, 1970)

3. K. Siegbahn, C. Nordling, G. Johansson, J. Hedman, P. F. Heden, K. Hamrin, U. Gelius, T. Bergmark, L. O. Werme, R. Manne, and Y., Baer, "*ESCA Applied to Free Molecules*," (North-Holland Publishing Company, Amsterdam-London, 1969).

4. S. E. Bradforth, A. Weaver, D. W. Arnold, R. B. Metz, and D. M. Neumark, "Examination of the Br + HI, Cl + HI, and F + HI hydrogen abstractoin reactions by photoelectron spectroscopy of Br HI $^-$, ClHI$^-$, and FHI$^-$," J. Chem Phys., **92**, 7205 (1990).

5. D. D. Sarma, K. Sreedhar, P. Ganguly, and C. N. R. Rao, "Photoemisssion study of $YBa_2Cu_3O_7$ through the superconducting transition: Evidence for oxygen dimerization," **36**, 2371 (1987).

6. Teijo Åberg, "Theory of X-Ray Satellites," Phys. Rev. **156,** 35 (1966).

7. P. A. Heimann, "Near Threshold Studies of Photoelectron Satellites," PhD Thesis, University of California, Berkeley (1986), LBL report No. 22419.

8. W. C. Wiley and I. H. McLaren, "Time-of Flight Mass Spectrometer with Improved Resolution," Rev. Sci. Instru. **26**, 1150 (1955).

9. C. N. Yang, "On the Angular Distribution in Nuclear Reactions and Coinncidence Measurements," Phys. Rev. **74**, (1948).

10. J. Cooper and R. N. Zare,"Angular Distribution of Photoelectrons," J. Chem Phys.,, **48** 942 (1968).

Chapter 1

1. Attilla Szabo, Neil S. Ostlund, *Modern Quantum Chemistry: Introduction to Advanced Electronic Structure Theory,* (McGraw-Hill Publishing Company, New York, 1982).

2. Ibid., pg. 196.

3. Teijo Åberg, "Theory of X-Ray Satellites," Phys. Rev. **156,** 35 (1966).

4. K. G. Dyall and F. P Larkins, "Satellite structure in atomic spectra I. Theoretical framework and application to excited states of the singly ionised rare gases," J. Phys B **15,** 203 (1982), and "Satellite structure in atomic spectra II. The outer-shell photoelectron spectra of the rare gases, "J. Phys B **15,** 219 (1982).

5 C. E. Moore *Atomic Energy Levels,* U. S. National Bureau of Standards, NBS Circular No. 467 (U.S. GPO, Washington, DC, 1949)

6. S. Svensson, B. Ericksson, N. Mårtensson, G. Wendin, and U. Gelius, "Electron Shakeup and Correlation Satellites and Continuum Shake-off Distributions in X-ray Photoelectron Spectra of the Rare Gas Atoms," J. Electron Spectr. **47,** 327 (1988).

7. C. N. Yang, "On the Angular Distribution in Nuclear Reactions and Coincidence Measurements," Phys. Rev. **74,** (1948).

8. K. T. Leung and C. E. Brion, "Experimental Investigations of the Valence Orbital Momentum Distributions and Ionization Energies of the Noble Gases by Binary (e,2e) Spectroscopy," Chem. Phys. **82,** 87 (1983).

9. A. Hibbet and J. E. Hansen, "Accurate wavefunctions for ^2S and ^2P states in Ar II," J. Phys. B **20,** L245 (1987), and the references therein.

10. M. Y. Adam, P. Morin, and G. Wendin, "Photoelectron satellites spectrum in the region of the 3s Cooper minimum of argon," Phys. Rev. A **31,** 1426 (1985).

11. H. Kossman, B. Krässig, V. Schmidt and J. E. Hansen, "High-Resolution Measurements of the 3s Satellite Spectrum of Argon between 77 and 120 eV Photon Energy," Phys. Rev. Lett. **58,** 1620 (1987).

12. C. E. Brion, K. H. Tan and G. M. Bancroft, "Synchrotron Radiaton Studies of the Ar $3s^{-1}$ Binding-Energy Spectrum: A Comparison of Experimental Intensities and Theory," Phys. Rev. Lett. **56,** 584 (1986).

13. H. Smid and J. E. Hansen, "Influence of the Energy of the Incident Photon on Satellite Intensities in Photoelectron Spectra of the Rare Gases," Phys. Rev. Lett. **52,** 2138 (1984).

14. W. Wijesundera and H. P. Kelly, "Photoionization cross section with excitation of neutral argon," Phys. Rev. A **36,** 4539 (1987).

15. U. Becker, B. Langer H. G. Kerkhoff, M. Kupsch, D. Szostak, R. Wehlitz, P. A. Heimann, S. H. Liu, D. W. Lindle, T. A. Ferret, and D. A. Shirley, "Observation of

Many New Argon Valence Satellites near Threshold," Phys. Rev. Lett. **60**, 1490 (1988).

16. P. A. Heimann, "Near Threshold Studies of Photoelectron Satellites," PhD Thesis, University of California, Berkeley (1986), LBL report No. 22419.

17. K. N. Huang, W. R. Johnson and Cheng, "Photoionization of the outer shells of neon, argon, krypton, and xenon using the relativistic random-phase approximation," Atomic and Nucl. Data Tables **26**, 33 (1981).

18. G. H. Wannier, "The Threshold Law for Single Ionization of Atoms or Ions by Electrons," Phys. Rev. **90**, 817 (1953).

19. U. Fano, "Excitations of atoms to states of high orbital momentum,"J. Phys. B **7**, L401 (1974).

20. R. P. Madden, D. L. Ederer, and K. Codling, "Resonances in the Photoionization Continuum of Ar I (20-150 eV)," Phys. Rev. **177**, 136 (1969).

21. K. H. Schartner, B. Mobus, P. Lenz, H. Schmoranzer, and M. Wildberger, "Observation of Resonances in the Ar-3s Photoionization Cross Section," Phys. Rev. Lett. **61**, 2744 (1988).

22. R. Haensel, G. Keitel, and P. Schreiber, "Optical Absorption of Solid Krypton and Xenon in the Far Ultraviolet," Phys. Rev. **188**, 1375 (1969).

23. P. A. Heiman, D. W. Lindle, T. A. Ferrett, S. H. Liu, L. J. Medhurst, M. N. Piancastelli, D. A. Shirley, U. Becker, H. G. Kerkhoff, B. Langer, D. Szostak, and R. Wehlitz, "Shake-off on inner-shell resonances of Ar, Kr, and Xe," J. Phys. B. **20**, 5005 (1987).

24. A. Neihaus, "Analysis of post-collision interactions in Auger processes following near-threshold inner-shell photoionization," J. Phys. B **10**, 1845 (1977).

Chapter 2

1. Attilla Szabo, Neil S. Ostlund, *Modern Quantum Chemistry: Introduction to Advanced Electronic Structure Theory,* pg. 196, (McGraw-Hill Publishing Company, New York, 1982).

2. Ibid., pg. 204 and pg.251.

3. Prins, Physica 1, 1174 (1934).

4. Michel Tronc, George C. King, and Frank Read, "Nitrogen K-shell excitaion in N_2, NO, and N_2O by high-resolution electorn energy-loss spectroscopy," J. Phys. B **13**, 999 (1980). and Michel Tronc, George C. King, and Frank Read, "Carbon K-shell excitation in small molecules by high-resolution electron impact," J. Phys. B **12**, 137 (1979).

5. A. P. Hitchcock and C. E. Brion, "K-shell excitation spectra of CO, N_2 and O_2," J. Elec. Spectros. and Rel. Phen. **18**, 1 (1980).

6. C. T. Chen, Y. Ma, and F. Sette, "K-shell photoabsorption of the N_2 molecule," Phys. Rev. A **40**, 6737 (1989).

7. M. Domke, C. Xue, A. Puschmann, T. Mandel, E. Hudson, D. A. Shirley, and G. Kaindl, "Carbon and oxygen K-edge photoionization of the CO molecule," Chem. Phys Letters **173**, 122 (1990):, Erratum **174**, 663 (1990); Y. Ma, C. T. Chen, G. Meigs, K. Randall and F. Sette, in "X-ray and Innershell Processes", edited by T. A. Carlson, M. O. Krause and S. T. Manson, AIP Conference Proceedings No. 215, pg 634 (1990).

8. U. Gelius, "ESCA studies of gases,"J. Electron Spectrosc. Relat. Phenom. **5**, 985 (1974).

9. D. W. Lindle, C. M. Truesdatle, P. H. Kobrin, T. A. Ferrett, P. A. Heimann, U. Becker, H. G. Kerkhoff, and D. A. Shirley, "Nitrogen K-shell photoemission and Auger emission from N_2 and NO," J. Chem. Phys. **81**, 5375 (1984).

10. M. F. Guest, W. R. Rodwell, T. Darko, I.H. Hillier, and J. Kendrick, "Configuration interaction calculations of the satellite peaks associated with C_{1s} ionization of carbon monoxide," J. Chem Phys., **66**, 5447 (1977).

11. G. Angonoa, O. Walter, and J. Schirmer, "Theoretical K-shell ionization spectra of N_2 and CO by a fourth-order Green's function method,"J. Chem. Phys. **87**, 6789 (1987).

12. L. Ungier and T. D. Thomas,"Resonance-Enhanced Shakeup in Near-Threshold Core Excitation of CO and N_2," Phys. Rev. Lett., **53**, 435 (1984).

13. A. Reimer, J. Schirmer, J. Feldhaus, A. M. Bradshaw, U. Becker, H. G. Kerkhoff, B. Langer, D. Szostak, and R. Wehlitz, "Near-Threshold Measurements of the C 1s Satellites in the Photoelectron Spectrum of CO," Phys. Rev. Lett. **57**, 1707 (1986).

14. C. T. Chen and F. Sette, "High Resolution Soft X-Ray Spectroscopies with the Dragon Beamline," Physica Scripta **T31**, 119 (1990).

15. P. A. Heiman, D. W. Lindle, T. A. Ferrett, S. H. Liu, L. J. Medhurst, M. N. Piancastelli, D. A. Shirley, U. Becker, H. G. Kerkhoff, B. Langer, D. Szostak, and R. Wehlitz, "Shake-off on inner-shell resonances of Ar, Kr, and Xe," J. Phys. B. **20**, 5005 (1987).

16. L. J. Medhurst, T. A. Ferrett, P. A. Heimann, D. W. Lindle, S. H. Liu, and D. A. Shirley, "Observation of correlation effects in zero kinetic energy electron spectra near the N1s and C1s thresholds in N_2, CO, C_6H_6, and C_2H_4," J. Chem. Phys. **89**, 6096 (1988).

17. A. Neilhaus, "Analysis of post-collision interactions in Auger processes following near-threshold inner-shell photoionization," J. Phys. B **10**, 1845 (1977).

18. A. Russek and W. Mehlhorn, "Post-collision interaction and the Auger Lineshape," J. Phys. B **19**, 911 (1986).

19. R. W. Nicholls, "Approximate formulas for Franck-Condon factors," J. Chem. Phys **74**, 6980 (1981).

20. J. Schirmer, G. Angonoa, S. Svensson, D. Nordfors, and U. Gelius, "High-energy photoelectron C 1s and O 1s shake-up spectra of CO," J. Phys. B , , 6031 (1987).

17. G. H. Wannier, "The Threshold Law for Single Ionization of Atoms or Ions by Electrons," Phys. Rev. **90**, 817 (1953).

22. T. A. Ferrett, D. W. Lindle, P. A. Heimann, M. N. Piancastelli P. H. Kobrin, H. G. Kerkhoff, U. Becker, W. D. Brewer, and D. A. Shirley, " Shape-resonant and many-electron effects in the S 2p photoionization of SF_6," J. Chem. Phys. **89**(8), 4726 (1988).

Part II Photodissociation

Introduction:

1. J. H. Fock, P. Gurtler, and E. E. Koch, "Molecular Rydberg Transitions in Carbon Monoxide: Term Value/Ionization Energy Correlation of BF, CO and N_2," Chem Phys. **47**, 87 (1980).

2. T. N. Rescigno and A. E. Orel, "Theoretical study of the 400 eV core-excited valence state of N_2," J. Chem Phys. **70**, 3390 (1979).

3. M. Tronc, G. C. King, and F. R. Read, "Carbon K-shell excitation in small molecules by high-resolution electron impact," J. Phys. B, **12**, 137 (1979).

4. A. P. Hitchcock, C. E. Brion, and M. J. van der Wiel, "Ionic frragmentation of inner shell excited states of CO_2 and N_2O," Chem Phys Lett., **66**, 213 (1979).

5. Y. Ma, F. Sette, G. Meigs, S. Modesti, and C. T. Chen, "Breaking of Ground-State Symmetry in Core-excited Ethylene and Benzene," Phys Rev. Lett., **63**, 2044 (1989).

6. K. Muller-Dethlefs, M. Sander, L. A. Chewter, and E. W. Schlag. "Site-Specific Excitation in Molecules at Very High Energies: Changes in Ionization Patterns of CF_3CH_3," J. Phys. Chem **88**, 6098 (1984).

7. R. Murphy, W. Eberhardt, "Site specific fragmentation in molecules: Auger-electron ion coincidence studies," J. Chem. Phys. **89**, 4054 (1988).

8. W. Eberhardt, T. K. Sham, R. Carr, S. Krummacher, M. Strongin, S. L. Weng, and D. Wesner, "Site-Specific Fragmentation of Small Molecules Following Soft-X-Ray Excitation," Phys. Rev. Lett. **50**, 1038 (1983).

9. W. Eberhardt, E. W. Plummer, I. W. Lyo, R. Carr, and W. K. Ford,"Auger-Electron-Ion coincidence Studies of Soft-X-Ray-Induced Fragmentation of N_2," Phys Rev. Lett. **58**, 207 (1987).

10. R. Murphy, I. W. Lyo, W. Eberhardt, "The effect of the nuclear motion on the electronic decay of core hole excited states in molecules," J. Chem Phy. **88**, 6078 (1988).

11. E. D. Poliakoff, L. A. Kelly, L. M. Duffy, B. Space, P. Roy, and S. H., Southworth, M. G. White, "Vibrationally resolved electronic aurtoionization of core-hole resonances,"J. Chem Phys. **89**, 4048 (1988).

12. W. C. Wiley and I. H. McLaren, "Time-of Flight Mass Spectrometer with Improved Resolution," Rev. Sci. Instru. **26**, 1150 (1955).

13. D. C. McGilvery and R. J. S. Morrison, "MacSimion" Montech Pty Ltd.

14. N. Saito and I. H. Suzuki, "Asymmetry of departing fragment ion in the K-shell excitation of N_2," Phys. Rev. Lett. **61**, 2740 (1988).

15. D. W. Lindle, C. M. Truesdatle, P. H. Kobrin, T. A. Ferrett, P. A. Heimann, U. Becker, H. G. Kerkhoff, and D. A. Shirley, "Nitrogen K-shell photoemission and Auger emission from N_2 and NO," J. Chem. Phys. **81**, 5375 (1984).

16. T. A. Carlson, D. R. Mullins, C. E. Beall, B. W. Yates, J. W. Taylor, D. W. Lindle, and F. A Grimm, "Angular Distribution of Ejected Electrons in Resonant Auger Processes of Ar, Kr and Xe," Phys Rev. A **39**, 1170 (1989).

17. N. Saito and I H. Suzuki, "Kinetic Energy Release from N_2 induced by Selective inner-shell excitation," Int. J. Mass. Spec. **82**, 61 (1988).

Chapter 3

1. W. E. Moddeman, T. A. Carlson, M. O. Krause, and B. P. Pullen, "Determination of the K-LL Auger Spectra of N_2, O_2, CO, NO, H_2O, and CO_2," J. Chem Phys. **55**, 2317 (1971).

2. C. M. Liegener, "Calculations on the Auger spectrum of N_2," J. Phys. B **16**, 4281 (1983).

3. E. W. Thurstrup and A. Andersen, "Configuration interaction studies of bound, low-lying states of N_2^-, N_2, N_2^+, N_2^{+2}," J. Phys. B. **8**, 965 (1975).

4. M. Cobb, T. F. Moran, R. F. Borkman, and R. Childs,"Ab initio potential energy curves for the low-lying electronic states of N_2^{+2}," J. Chem, Phys. **72**, 4463 (1980).

5. K. P. Huber and G. Herzberg, *Molecular Spectra and Molecular Structure IV. Constants of Diatomic Molecules*, (Van Nostrand Reinhold Co., New York, 1979).

6. C. E. Moore *Atomic Energy Levels,* U. S. National Bureau of Standards, NBS Circular No. 467 (U.S. GPO, Washington, DC, 1949)

7. W. Eberhardt, J. Stohr, J. Feldhaus, E. W. Plummer, and F. Sette, "Correlation between Electron Emission and Fragmentation into Ions following Soft-X-Ray Excitation of the N_2 Molecule," Phys. Rev. Lett. **51**, 2370 (1983).

8. T. A. Carlson and M. O. Krause, "Relative Abundances and Recoil Energies of Fragment Ions Formed from the X-Ray Photoionization of N_2, O_2, CO, NO, CO_2, and CF_4," J. Chem. Phys. **56**, 3206 (1972).

9. W. Eberhardt, E. W. Plummer, I. W. L[illegible] R. Carr, and W. K. Ford,"Auger-Electron-Ion coincidence Studies of Soft [illegible]-Ray-Induced Fragmentation of N_2," Phys Rev. Lett. **58**, 207 (1987).

10. N. Saito and I H. Suzuki, "Kinetic Energy Release from N_2 induced by Selective inner-shell excitation," Int. J. Mass. Spec. **82**, 61 (1988).

11. L. J. Medhurst, T. A. Ferrett, P. A. Heimann, D. W. Lindle, S. H. Liu, and D. A. Shirley, "Observation of correlation effects in zero kinetic energy electron spectra near the N1s and C1s thresholds in N_2, CO, C_6H_6, and C_2H_4," J. Chem. Phys. **89**, 6096 (1988).

12. I. H. Suzuki and N. Saito, "Fragmentation of N_2 in the inner-shell to Rydberg-orbital excited states $(K)^{-1}(nl)^1$," J. Chem Phys. **91**, 5324 (1989).

13. C. T. Chen, Y. Ma, and F. Sette, "K-shell photoabsorption of the N_2 molecule," Phys. Rev. A **40,** 6737 (1989).

14. N. Saito and I. H. Suzuki, "Asymmetry of departing fragment ion in the K-shell excitation of N_2," Phys. Rev. Lett. **61**, 2740 (1988).

15. N. Saito and I. H. Suzuki, "Kinetic energies of fragment ions from N_2 absorbing soft x-rays by a photoion-photoion coincidence technique," J. Phys. B **20**, L785 (1987).

16. W. Habenicht, K. Muller-Dethlefs, and E. W. Schlag, "Zero-Kinetic Energy Photoelectron-Photoion Coincidence Measurements of Ar in the 2p and N_2 in the 1s Region," J. Elec. Spectr. **52**, 697 (1990).

Chapter 4

1. Y. Ma, F. Sette, G. Meigs, S. Modesti, and C. T. Chen, "Breaking of Ground-State Symmetry in Core-excited Ethylene and Benzene," Phys Rev. Lett., **63**, 2044 (1989).

2. W. Domcke and L. S. Cederbaum, "Vibronic Coupling and Symmetry Breaking in Core Electron Ionization," Chem Phys., **25**, 189 (1977).

3. F. X. Gadea, H. Koppel, J. Schirmer, L. S. Cederbaum, K. J. Randall, A. M. Bradshaw, Y. Ma, F. Sette, and C. T. Chen, "Vibronic Coupling and Core-Hole Localization in K-Shell Excitations of Ethylene," Physl Rev. Lett. **66**, 883 (1991).

4. M. B. Robin, *Higher Excited States of Polyatomic Molecules, Vol III*, (Academic Press, Inc. New York, 1985).

5. R. R. Rye, T. E. Madey, J. E. Johnson, and P. H. Holloway, "Chemical-state effects in Auger electron spectroscopy," J. Chem Phys. **69**, 1504 (1978).

6. F. L. Hutson and D. E. Ramaker, "Identification of resonant excitation and shakeoff contributions to the C KVV Auger line shapes of several gas phase hydrocarbons," J. Chem Phys. **87**, 6824 (1987).

7. C. R. Brundle, M. B. Robin, N. A. Kuebler, and H. Basch, "Perfluoro Effect in Photoelectron Spectroscopy. I. Nonaromatic Molecules," J. Amer. Chem. Soc., **94**, 1451 (1972).

8. R. Stockbauer and M. G. Inghram, "Threshold photoelectron-photoion coincidence mass spectrometric study of ethylene and ethlylene-d_4," J. Chem. Phys. **62**, 4862 (1975).

9. T. Ibuki, G. Cooper, and C. E. Brion, "Absolute Dipole Oscillator Strengths for Photoabsorption and the Molecular and Dissociative Photoionization of Ethylene," Chem. Phys. **129**, 295 (1989).

10. M. N. Piancastelli, T. A. Ferrett, D. W. Lindle, L. J. Medhurst, P. A. Heiman, S. H. Liu, and D. A. Shirley, "Resonant processes above the carbon 1s ionization threshold in benzene and ethylene," J. Chem. Phys., **90**, 3004 (1989).

11. *Handbook of Chemistry and Physics,* CRC Press, Cleveland Ohio (1972).

END

DATE FILMED

01/27/92